



BUDAPEST UNIVERSITY OF TECHNOLOGY AND ECONOMICS

FACULTY OF MECHANICAL ENGINEERING

GÉZA PATTANTYÚS-ÁBRAHÁM DOCTORAL SCHOOL OF MECHANICAL ENGINEERING
SCIENCES

DEPARTMENT OF MECHATRONICS, OPTICS AND MECHANICAL ENGINEERING

INFORMATICS

MECHATRONICS AND OPTICS PARTIAL PROGRAM

Kinematic and Dynamic Limits of Holonomic Mobile Robots

Ph.D. Thesis

Géza Szayer

Supervisors:

Péter Korondi, DSc., Prof. Univ.

Péter Tamás, Ph.D.

Budapest, 2017.

ACKNOWLEDGEMENTS

I would like to express my gratitude to everyone who helped me in my studies leading to this thesis work. Utmost thanks to my supervisors, Professor Péter Korondi and Péter Tamás, who provided an excellent working environment to accomplish my aspirations and to everyone at the department.

Special thanks to my family supporting me in my studies all the way to arrive at this point.

CONTENTS

Acknowledgements.....	iii
Contents	iv
List of Figures	vii
List of Tables	xiii
1 INTRODUCTION	1
1.1 Goal of the dissertation.....	2
1.2 Structure of the dissertation	3
1.3 Nomenclature.....	3
1.3.1 Abbreviations.....	3
1.3.2 Roman letters	4
1.3.3 Greek letters	5
2 State of the art	6
2.1 History of the holonomic wheel	6
2.2 Application in mobile robotics	7
2.3 Previous results focusing on the mechanical capabilities of holonomic robots	10
2.4 Relevant publications of Hungarian authors	12
2.5 Conforming with current high-level control platforms	14
2.6 ISO Standardization.....	15
3 Proposed phase space to define the kinematic and dynamic limits of holonomic wheeled mobile robots	16
3.1 Practical application of direction dependent velocity and acceleration limits .	18
4 Modeling of omniwheeled robots	19
4.1 Inverse kinematic model.....	19
4.2 Calculating maximum velocities	20
4.3 Velocity phase space in case of a kiwi drive	21
4.3.1 Utilizing the peripheral areas of velocity phase space of kiwi drive robots	22
4.4 Inverse dynamic model.....	27
4.5 Defining the friction reserve multiplier	30
4.6 Maximum acceleration of the robot considering the maximum torque of electric motors	31

4.7	Calculating the maximum acceleration of the robot avoiding a tip-over situation	32
4.8	Visualizing the acceleration space.....	33
4.9	Investigation of 3D phase spaces.....	37
4.9.1	Braking distance and climbing ability	37
4.9.2	Direction independency and the compactness of the phase space	39
4.9.3	Effect of the height of the CoG on unidirectionality	44
5	Evaluation	48
5.1	Calculation examples and kinematic simulation	48
5.1.1	Kinematic simulation – Limits based on velocity space.....	48
5.2	Acceleration space - Application for assisting robot design	49
5.3	Robotic implementation based on decentralized hardware architecture	50
5.3.1	Applicability Criteria for Compliance with Reliability Requirements	50
5.3.2	General overview of stock hardware architectures for robotic research ..	51
5.3.3	Introduction to robot control with LinuxCNC.....	51
5.3.4	Interfacing with LinuxCNC	52
5.3.5	Servo amplifiers.....	57
5.4	Application of velocity and acceleration space theories.....	62
5.4.1	Embedded implementation example of dynamic acceleration and velocity controls	63
5.4.2	Reusable open source ROS C++ catkin package.....	64
5.5	Evaluation of the results	65
5.5.1	Wheel slip tests to validate the dynamic model.....	65
5.5.2	Evaluation of model efficiency	69
5.5.3	Model sensitivity to the position of the CoG	69
5.5.4	Defining the safe area by applying a safety reserve	70
6	Conclusion	71
6.1	Significantly improved wheel slip based acceleration space.....	71
6.2	Reusable open source implementation	71
6.3	Comparing holonomic mobile robots	72
6.3.1	Braking distance and climbing ability	72

6.3.2	Direction independency	72
6.3.3	Standardization efforts in the field of mobile robotics	72
7	Thesis	73
7.1	Thesis 1.....	74
7.1.1	Background explanation	74
7.1.2	Practical application.....	74
7.2	Thesis 2.....	75
7.2.1	Background explanation	75
7.2.2	Practical application.....	76
7.3	Thesis 3.....	77
7.3.1	Background explanation	77
7.3.2	Practical application.....	79
8	Tézisek Magyarul.....	80
1.	tézis	81
8.1.1	Háttér magyarázat	81
8.1.2	Gyakorlati alkalmazás.....	82
8.2	2. tézis	82
8.2.1	Háttér magyarázat	82
8.2.2	Gyakorlati alkalmazás.....	83
8.3	3. tézis	84
8.3.1	Háttér magyarázat	84
8.3.2	Gyakorlati alkalmazás.....	86
	Appendix.....	89
	Author's publications.....	90
	Bibliography	92

LIST OF FIGURES

Fig. 1 . Statistics and prognostication of the exponentially growing service robotics sector	1
Fig. 2 . Different moving direction and robot body orientation in case of an ethologically inspired holonomic mobile robot. The object-oriented behavior makes the robot motion more natural, and helps people to naturally predict the upcoming motion direction of the robot.	2
Fig. 3 . Drawings of the patent of the first holonomic wheel from 1919 (a), and a later (1974) patent which defined the current shape of omniwheels (b)	6
Fig. 4 . The first omniwheeled mobile robot at the Euromicro competition, London, 1980 (a), and the first 3-wheeled arrangement at the International Personal Robots Congress, Mexico, 1984 (b).....	7
Fig. 5 . Killough's patent drawings from 1994. The holonomic wheel, consisting of two traditional wheels in an orthogonal arrangement (a), and the isometric view of the kiwi drive scheme (b).....	8
Fig. 6 . Front (a) and rear (b) wheel driven cases of a kiwi drive mobile robot platform, where V_{wheel} is the constrained driving velocity of the wheels and V_{robot} is the linear velocity vector. Due to robot dynamics, the maximum acceleration of the robot is higher in case (b)......	9
Fig. 7 . Robots of the Cornell RoboCup Team: Bottom view of the RoboCup 2000 winner (a), it used the same orthogonal wheel concept as Killough in 1994. A later design from 2004 (b), it used small rollers on the circumference of the wheel.....	13
Fig. 8 . Real and assumed acceleration phase spaces of a kiwi drive platform. The transparent body is the calculated and measurement-verified acceleration phase space. The solid body is the well-known and commonly used direction-independent model called friction circle. The volumetric difference represents the non-utilized capabilities of the robot dynamics. Axes x and y represent planar linear accelerations, and z represents angular acceleration. (a) is the x-z plane view, (b) is y-z plane view, (c) is x-y plane view, (d) is an isometric view.	17

Fig. 9 . Block diagram of control schema. The real-time controller of acceleration and velocity receives a preferred velocity command from the high-level robot control platform and adjust it according to the mechanical model and actual motion state of the robot	18
Fig. 10 . Robot-coordinate system, fixed to the geometric center in the x-y direction and fixed to the ground in vertical direction.	19
Fig. 11 . Velocity vectors of an omnidirectional wheel (top view)	20
Fig. 12 . Maximum linear velocities depending on direction and angular velocity. The bold hexagon corresponds to the limit of linear velocity when the angular velocity is zero. As the angular velocity grows (thick solid lines), the maximum linear velocity is often reduced. The dot in the center shows that the maximum linear velocity is zero when the robot is rotating with the maximum angular velocity. The dashed lines represents the linear velocity limit in case of negative angular velocity.	21
Fig. 13 . Vector set of feasible velocities in the velocity space. Linear velocities are represented by the x and y axes, and angular velocity is represented by the z axis. The shade of the surface represents the distance from the origin, which is equal to the maximum length of the velocity vector.	22
Fig. 14 . 3D (a) and bottom view (b) of the velocity phase space. The bolded line hexagon shows the maximum linear velocity in case the angular acceleration is zero. The gray areas show the special areas where the linear velocity is higher while the angular velocity is non-zero.	23
Fig. 15 . Comparison of actual velocity vectors of the linear movement (a) with the corresponding rotating movement (b). In the second case, the absolute value of the linear velocity vector of the robot ($v_{CoG, 3}$) is 33.3% higher compared to the first case ($v_{CoG, 2}$)	25
Fig. 16 . Mechanic model of a three omniwheel based kiwi drive mobile robot platform	28
Fig. 17 . Tangential and radial components of the wheel force.....	29

Fig. 18 . <i>x-y</i> section plane of the wheel slip constrained acceleration phase space, for different heights of the CoG (h) related to the radius (r) of the circle coincident with the wheels when the angular acceleration is zero	35
Fig. 19 . Acceleration phase space constrained by wheel slip. The shade of the surface represents the distance from the origin, which is equal to the maximum length of the acceleration vector.	36
Fig. 20 . The <i>x-y</i> section plane of the tip-over situation constrained acceleration phase space	37
Fig. 21 . <i>x-y</i> section plane of the (wheel slip constrained) acceleration phase space. The minimum acceleration has to be chosen for defining the safety braking distance (worst case principle), while the maximum can be used for calculating the climbing ability.	38
Fig. 22 . Compactness measurement of a 2D (a) and a 3D (b) shape by a convex hull. 2D/3D compactness is defined as the area/volume ratio of the original shape and its convex hull, respectively.....	41
Fig. 23 . Principle of the Reock score in 2D (a) and 3D (b). 2D/3D compactness is defined as the ratio of the surface/volume of the original shape and the bounding circle/sphere, respectively.....	41
Fig. 24 . An example where the Reock score yields a very low value, caused by one narrow extremal protrusion which could be left unused by the robot control. The relatively high protrusion is caused by a 5 cm horizontal offset of the CoG measured from the geometrical center on the <i>x-y</i> plane, where the robot diameter is 60 cm....	42
Fig. 25 . Principle of the Polsby-Popper (a) and Schwartzberg (b) compactness scores. The first one compares the surfaces in case of equal perimeters, while the second one compares the perimeters in case of equal surfaces.....	43
Fig. 26 . Wheel slip based acceleration phase spaces of the robot in case of neglecting (a) and considering (b) the effect of the CoG height.	45
Fig. 27 . Higher resolution phase space for volume and surface calculations (a) and the generated Alpha shape	46

Fig. 28 . Unidirectionality as the function of CoG height (Ψ_f), maximum error (ϵ_{max}) and linear correlation (R) of vector length compared to the case of zero CoG height.	46
Fig. 29 . Peripheral velocity of each wheel, where the three different plots represent wheels 1, 2 and 3 (a) and the limited linear velocity of the robot (b)	48
Fig. 30 . Graphical user interface of the acceleration space visualizer Matlab application	49
Fig. 31 . Experimental robot and its drive system in the bottom view	50
Fig. 32 . Default graphical user interface of LinuxCNC for numerical control	52
Fig. 33 . System layout (a) and functional block diagram (b) based on GM6-PCI motion control card.....	54
Fig. 34 . PCI interface rooted on two layers with the diagonal placement of PCI bridge ASIC.....	55
Fig. 35 . RS485 extension bus (a) and general module isolation concept	56
Fig. 36 . Examples of (a) analogue and (b) differential incremental servo interfaces ...	57
Fig. 37 . Brushed DC servo amplifiers installed on mobile robot	57
Fig. 38 . Block diagram of the brushed DC servo controller.....	58
Fig. 39 . DC servo amplifier 3D model (a), electronics (b), enclosure (c)	60
Fig. 40 . Screenshot of the software during configuration and servo tuning	61
Fig. 41 . Functional block diagram of the decentralist robot control architecture.....	62
Fig. 42 . Functional block diagram of limiter functions	63
Fig. 43 . Structure of acceleration (a) and velocity limiter algorithms (b)	64
Fig. 44 . (a) Slip test results of the acceleration space at zero angular acceleration, where the dotted line is measurement data, the continuous line is the calculated dynamic model, the dashed line is direction-independent abstraction and the gray area is the safe area of the acceleration vector. (b) The absolute value of relative errors, where the thin line is direction-independent abstraction and the thick line is the simulated dynamic model.....	67

FIG. 45 . (a) Slip test results of the acceleration space at 0.4 rad/s ² angular acceleration, where the dotted line is measurement data, the continuous line is the calculated dynamic model, the dashed line is direction-independent abstraction and the gray area is the safe area of the acceleration vector. (b) The absolute value of relative errors, where the thin line is direction-independent abstraction and the thick line is the simulated dynamic model.....	68
Fig. 46 . 3D (a) and bottom view (b) of the velocity phase space. The bold contoured hexagon shows maximum linear velocity in case angular acceleration is zero. Black vectors mark maximum linear velocities in case of zero angular velocity, while the dashed vector is the maximum linear velocity vector when angular velocity is unconstrained.	73
Fig. 47 . Actual velocities in case of the circular path which is faster than the straight one, and the applied notations.....	74
Fig. 48 . Wheel slip based acceleration phase spaces of the robot in case of neglecting (a) and considering (b) the effect of the CoG height.	78
Fig. 49 . Unidirectionality as the function of CoG height (Ψ_f), maximum error (ϵ_{\max}) and linear correlation (R) of vector length compared to the case of zero CoG height. r is the radius of the circle coincident with the wheels.	78
Fig. 50 . Matlab application for assisting the robot design process	79
Fig. 51 . Kiwi hajtású robot kinematikai fázisterének 3D és alulnézete, ahol a vastag hatszög jelöli a nulla szögsebességhez tartozó síkot. A nulla szögsebességnél irányonként elérhető maximális lineáris sebességet fekete vektorok ($v_{CoG,1}$ és $v_{CoG,2}$) jelölik, míg a nem nulla szögsebességhez a fehér szaggatott vektor ($v_{CoG,3}$) tartozik.	80
Fig. 52 . Az egyenesnél gyorsabb, körív menti mozgáspálya pillanatnyi sebesség vektorai és az alkalmazott jelölések.....	81
Fig. 53 . A súlypont helyzetének hatását elhanyagoló (a), illetve figyelembe vevő (b) kiwi hajtású mobilrobot gyorsulás fázistere.....	85
Fig. 54 . Általános irányfüggetlenségi tényező (Ψ_f), maximális relatív hiba (ϵ_{\max}) és lineáris korreláció (R) a súlypont helyzetét elhanyagoló modellhez képest a súlypont	

föltől mért magasságának (h) függvényében. r a robot alapkörének sugara, amely körvonal a kerekek tapadási pontjain halad át.	85
Fig. 55 . Kiwi hajtású robot tervezését támogató szoftver.....	87

LIST OF TABLES

TABLE I Error Propagation Between the wheel slip limited acceleration space and the Measured Data For 0 [rad/s ²] Angular Acceleration.....	67
TABLE II Error Propagation Between the wheel slip limited acceleration space Model and the Measured Data For 8.7 [rad/s ²] Angular Acceleration.....	69

1 INTRODUCTION

The market share of service robots is the fastest growing sector according to the past statistics and near future prognostication of the Japan Robotics Association (see Fig. 1). The most of the robots are open-chain manipulators within the manufacturing industry, while in the service robotics sector, mobile robotics is the greatest discipline.

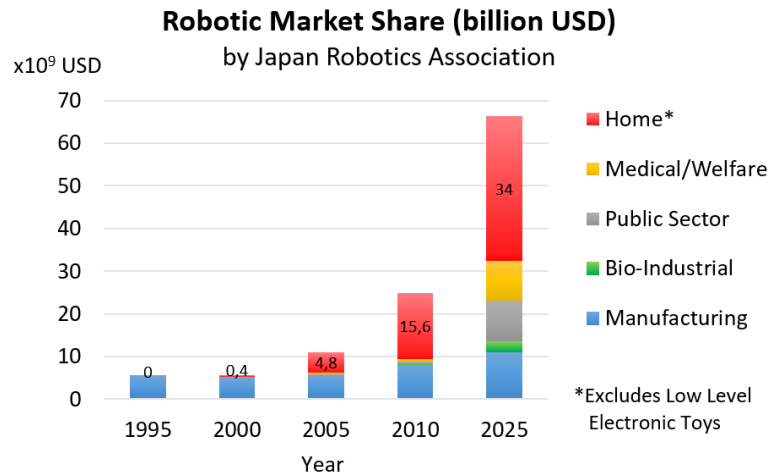


Fig. 1. Statistics and prognostication of the exponentially growing service robotics sector

The reach capabilities of mobile robots are strongly depending on the applied kinematic scheme, especially in non-industrial environments. In the households, the robots should be able to go all the places where people can go in order to perform tasks in different locations. From strictly this point of view, legged mobile robots would be perfect solutions. However, using mechanical limbs for movement has many other disadvantages compared to wheeled mobile robots: Much higher complexity, energy consumption and costs. Moreover, the current state of the art of walking robots is far from feasible applications.

This led the market to deal with the other restrictions of wheeled mobile robots by adjusting the working environment to be compliant with rolling wheels. However, the earlier (non-holonomic) drive schemas - like differential drive - have still too much kinematic restrictions to be useful in human environment. The unskillful motion capabilities are not just restricting the robot in solving tasks, but their social adaptivity and human interaction is also weak: Ethologist states a hypothesis that the same moving and “looking” direction (path driven orientation) makes the mobile robots moving like an artificial agent [1]. It is also hard for people to assume the upcoming motion state of these robots, as they just starts, stops and turns immediately without indication before.

The holonomic mobile robots can be driven in any translational direction, independently of the current orientation or continuous rotation of the robot posture (see

Fig. 2). This advantage makes the holonomic drive schemas a suitable trade-off between complicated legged robots and non-holonomic mobile robots.

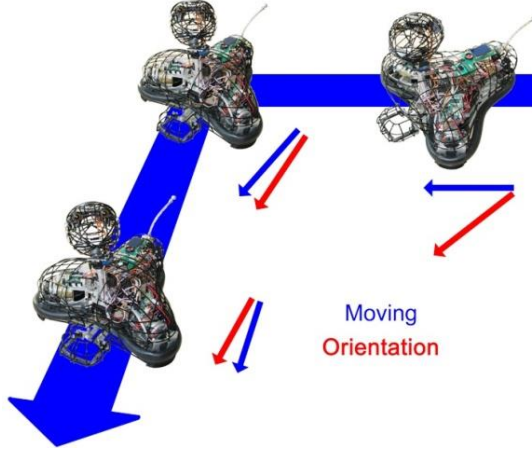


Fig. 2. Different moving direction and robot body orientation in case of an ethologically inspired holonomic mobile robot. The object-oriented behavior makes the robot motion more natural, and helps people to naturally predict the upcoming motion direction of the robot.

Holonomic drive schemas appeared more than three decades ago in mobile robotics. This advantageous characteristic enabled holonomic robots to operate in curvy narrow passages and crowded environments. Still, their widespread application was restricted due to two major drawbacks: the small rollers on the circumference of the omnidirectional wheels are not suitable for rough and soft terrains, either. While on hard surface, intense wheel slip is a common problem compared to traditional wheel based drives.

1.1 Goal of the dissertation

In general, many trajectory generators and path planners handle the capabilities of holonomic robots as direction independent constants. But in practice, the possible maximum acceleration of a holonomic drive often varies ($\pm 30\text{--}60\%$) according to the direction of the acceleration vector due to the inherent characteristics of robot dynamics. The current high-level controls have to consider these intensely changing limits, otherwise the result will not utilize the special capabilities of omnidirectional drive systems.

The major aims of the research are to:

- Measure and describe all direction dependent phenomena which significantly affect the mechanical capabilities of holonomic mobile robots.
- Provide appropriate model(s) to describe and handle the non-linearity of these robots.
- Assist the early robot design process with information on desirable mechanical capabilities.

- Provide control schema(s), which conform(s) to the current high-level control platforms and fit(s) into current robot control architectures without major rearrangements.

1.2 Structure of the dissertation

After the Introduction, Section 2 describes the background of mobile robot research focused on holonomic mobile robot platforms. Section 3 introduces a 3D phase space based methodology. Section 4 discusses the theoretical background of holonomic mobile robot control from the point of view of motion capabilities. Section 5 describes the robotic implementation and evaluation based on a universal Linux RTAI based control system. Section 6 presents the results and concludes the dissertation, while Sections 7 and 8 summarize the thesis in English and in Hungarian, respectively.

1.3 Nomenclature

1.3.1 Abbreviations

APF	Artificial Potential Field
iAPF	Improved Artificial Potential Field
ASIC	Application Specific Integrated Circuit
CNC	Computer Numerical Control
CoG	Center of Gravity
DWA	Dynamic Window Approach
FET	Field Effect Transistor
FPGA	Field Programmable Gate Array
GUI	Graphical User Interface
HAL	Hardware Abstraction Layer
IRV	Ideal Reference Velocity
ND	Nearness Diagram
MAD	Mean Average Deviance
MRPT	Mobile Robot Programming Toolkit
RISC	Reduced Instruction Set Computing
ROS	Robot Operating System
RTAI	Real-Time Application Interface
SLAM	Simultaneous Localization and Mapping
SPI	Serial Peripheral Interface
WG	Working Groups
WMR	Wheeled Mobile Robot

1.3.2 Roman letters

A_i		contact points of the wheels
A_p	[m ²]	surface area of 3D phase space
F	[N]	Force
G		goal position point of the path
I	[kgm ²]	moment of inertia
PP	[-]	Polsby-Popper score
R	[m]	radius of a circular path
R_a	[V]	armature resistance of DC motor
S		start position point of the path
V_a	[V]	armature voltage of DC motor
V_p	[m ³]	volume of 3D phase space
g	[m/s ²]	gravitational acceleration
h	[m]	height of the CoG measured from the floor
l_{brake}	[m]	braking distance
m	[kg]	mass
q	[m] or [rad]	robot posture: x, y coordinates of the position and orientation
r	[m]	radius of the circle coincident with the wheels
r_{wheel}	[m]	radius of the wheels
r_{sch}	[-]	Schwartzberg score
\underline{r}_{Ai}	[-]	vectors pointing to the contact points of the wheels
v	[m/s]	linear velocity

1.3.3 Greek letters

Λ	[-]	ratio of maximum linear velocities in case of non-zero and zero angular velocity constraints
ϕ_v	[-]	velocity phase-space
ϕ_a	[-]	acceleration phase-space
$k\phi$	[-]	speed constant of DC motor
Ψ	[-]	isoperimetric ratio normalized to the sphere (sphericity)
Ω	[rad/s]	angular velocity of DC motor armature
α	[rad]	angle of rotation of the robot between the start and goal positions
δ_{climb}	[rad]	maximum climbing ability (slope angle)
ε	[-]	relative error
λ	[-]	velocity reserve multiplier
μ	[-]	Coulomb friction coefficient
ξ	[rad/s ²]	angular acceleration
σ_f	[-]	friction reserve multiplier
σ_t	[-]	torque reserve multiplier
τ	[Nm]	torque
ω	[rad/s]	angular velocity

2 STATE OF THE ART

2.1 History of the holonomic wheel

The first holonomic wheel - patented in 1919 (see Fig. 3/a) - was the first that satisfied omnidirectional capabilities in a kinematic manner. However, the shape of straight cylindrical secondary rollers on the perimeter caused a discontinuous rolling surface. This disadvantageous characteristic strongly restricted its applicability. The current shape of the rolling surface of omniwheels was defined in a later patent in 1974 (see Fig. 3/b).

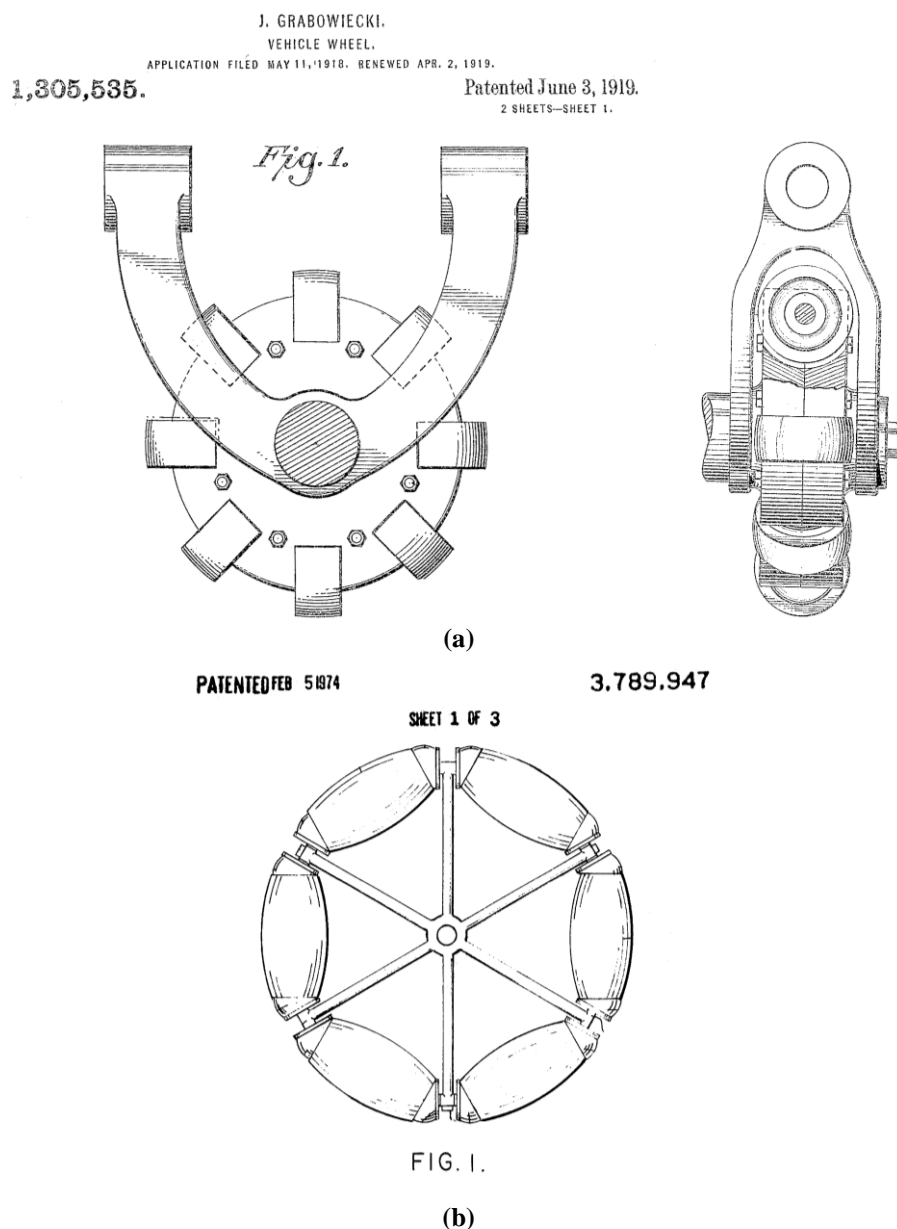


Fig. 3. Drawings of the patent of the first holonomic wheel from 1919 (a), and a later (1974) patent which defined the current shape of omniwheels (b)

2.2 Application in mobile robotics

Omniwheels appeared in mobile robotics in the early 1980s. The first evidence of an omniwheeled robot is from London in 1980 (see Fig. 4/a). The robot of Jean-Daniel Nicoud and his students at a Micromouse robotic competition called Euromicro used omniwheels to avoid all turning movements during the maze solving navigation. During these years, Nicoud played an important role in the invention and design evolution of early omnidirectional mechanical computer mouse concepts, which were actually applied omniwheels. He used optical encoders for tracking the rotation of a single ball made of hard rubber. His valuable results were used in the first commercial computer mouse launched by Logitech in 1982 (Logitech P4). Today, Nicoud is still active and running a special online shop for small scale robotic parts. In 2015, he sponsored the first Hungarian Half-size Micromouse competition by micro-motors and special mechanical parts.

The first 3-wheeled holonomic robot was introduced in 1984, at the International Personal Robots Congress in Mexico. The robot, named Fetal I. was constructed by Bill La (see Fig. 4/b).

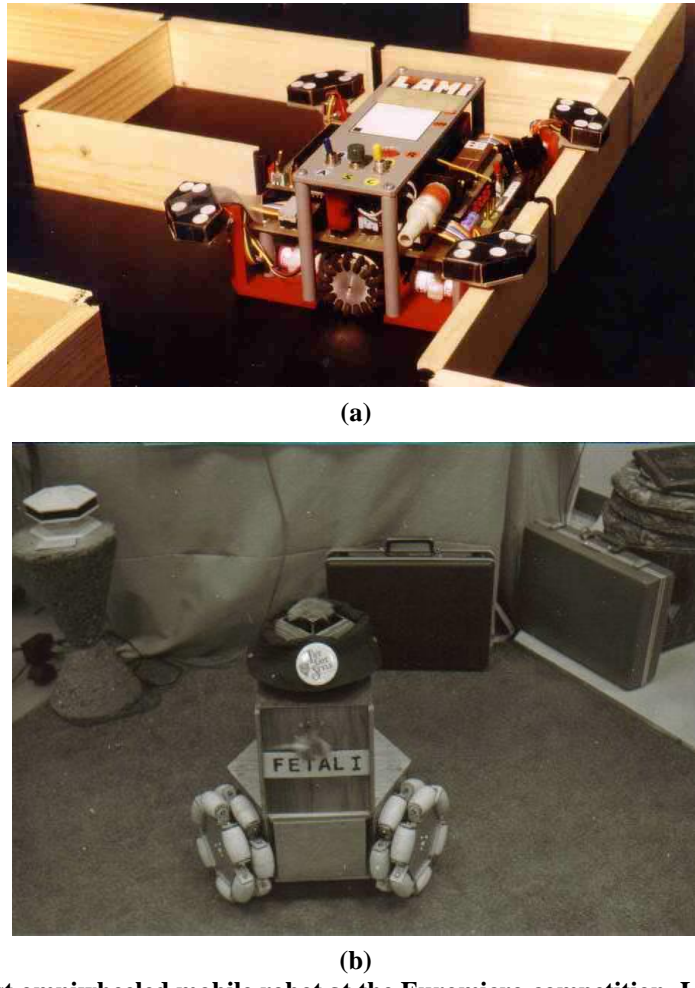


Fig. 4. The first omniwheeled mobile robot at the Euromicro competition, London, 1980 (a), and the first 3-wheeled arrangement at the International Personal Robots Congress, Mexico, 1984

A platform employing three omnidirectional wheels (instead of actuated caster wheels [2]–[8]) in a triangular formation is generally called a kiwi drive. The first scientific paper related to kiwi type holonomic mobile robot platforms was published in 1992 by Stephen Killough and Francois G. Pin [9]–[11]. Killough's design used three pairs of wheels mounted in cages, orthogonal to each other, and thereby achieved holonomic movement without using true omniwheels (see Fig. 5). (Some different interesting solutions were experimented, mostly based on driving balls or additional joints [12]–[15].)

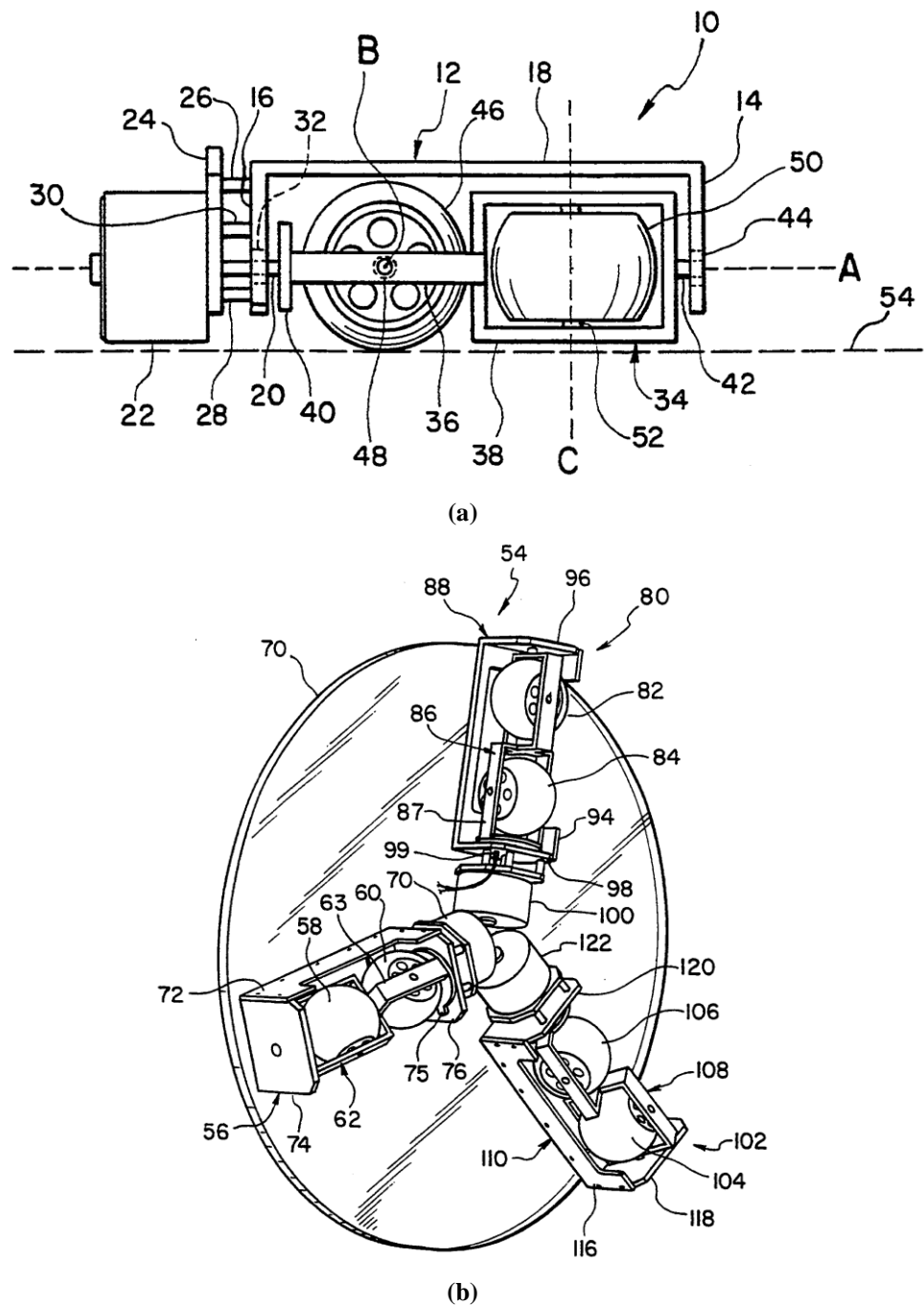


Fig. 5. Killough's patent drawings from 1994. The holonomic wheel, consisting of two traditional wheels in an orthogonal arrangement (a), and the isometric view of the kiwi drive scheme (b).

After Killough's publication, several research works focused on the modeling and control of these holonomic platforms. The kinematics were first described by Killough, and the dynamics are presented in several different forms. The general comparison of different drive schemes from kinematic and dynamic points of view were summarized in [16]. Path tracking for these robots is developed using different methods: Vazquez and Velasco-Villa derived the computed-torque control and trajectory tracking for omnidirectional robots [17], [18]; Kiattisin Kanjanawanishkul and Andreas Zell solved the path following problem by model predictive control [19]. The sliding mode control based approach can also be used, especially in systems including transport delay [20]–[22]. Moreover, an integral sliding mode control based method is also known [23]. Trajectory generation for omnidirectional vehicles is also developed for time optimal and collision free control solutions [24]–[29]. An extraordinary solution for kinematic control can be studied in [30], based on a parallel ant colony optimization (PACO) algorithm. Another parallel computing solution is presented in [31]; however, the applied neural network used for high level (vision and further sensors based) adaptive robot control instead of the kinematic/dynamic optimization of the kiwi drive. Nowadays, holonomic platforms are used in the industry and households [32], e.g. Mecanum wheel [33] based forklifts or security robots.

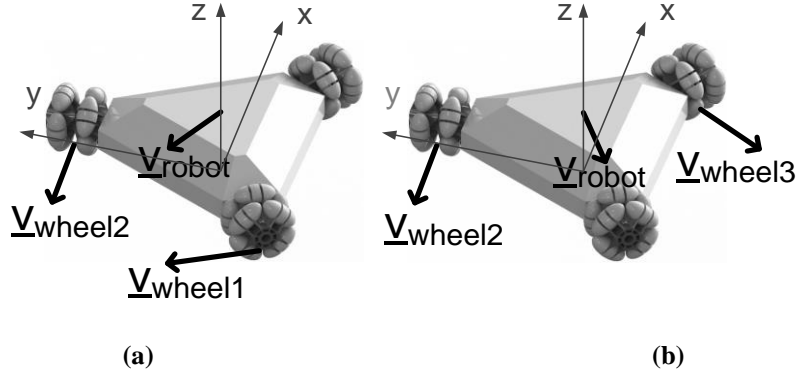


Fig. 6. Front (a) and rear (b) wheel driven cases of a kiwi drive mobile robot platform, where V_{wheel} is the constrained driving velocity of the wheels and V_{robot} is the linear velocity vector. Due to robot dynamics, the maximum acceleration of the robot is higher in case (b).

Regarding results in general for generation and tracking of time optimal trajectories, most methods apply constant velocity and acceleration limits to the robot body. Only a few of the methods deal with the possible maximum velocity and acceleration of the robot, which are rapidly changing during motion. Surprisingly, there are cases when the robot can go faster in a direction if it rotates during linear movement [34]. As an illustrative example, Fig. 6 shows a front and a rear wheel driven case, where the possible maximum acceleration (and deceleration) difference is often twofold.

2.3 Previous results focusing on the mechanical capabilities of holonomic robots

In 1995, one year after Killough's introduction of the kiwi drive [11], dynamical modelling of the continuous slip of omniwheels was introduced [35]. The dynamics was derived in generalized coordinates in a top view (2D) planar approach, neglecting the effect of the height of the CoG, thus ignoring the distinct load forces on the wheels.

In 2002, Robert L. Williams II, Brian E. Carter, Paolo Gallina and Giulio Rosati [36], [37] proposed the extensive modelling of holonomic movement considering wheel slip. However, their work mostly focused on slip caused by a single row omniwheel which is primarily designed for material handling industrial applications instead of mobile robots. They included the latter friction case for handling the non-continuous rolling surface [38] of the single wheel. They assumed that robot weight is equally distributed on each wheel, which neglects the effect (showed by Fig. 6) when robot operation is similar to a front or rear wheel driven vehicle. A similar transverse wheel slip theory was also published in connection with ball drives [39].

In 2003, T. Kalmár-Nagy presented the first 3D phase space for admissible controls, involving kinematics, and simplifying dynamics and motor parameters [40]. The dynamic equations were derived in general coordinates, without considering the height of the CoG in the vertical direction. The paper did not focus on wheel slip, therefore the changing load distribution on the wheels was neglected.

André Scolari Conceicao, A. Paulo Moreira, and Paulo J. Costa presented a method in 2006 for time optimal velocity control that considers maximum wheel speeds [41], called ideal reference velocities (IRV). This IRV method can be adapted and may work for the dynamics too, but it causes too many different equations for different wheel arrangements. The solution can be very difficult, especially when the robot is over-actuated by four or more wheels. In this work, a similar method is presented, which yields the same end results for the ideal velocity command but with a different and easier-to-implement approach: There is no need to express anything from inverse kinematic equations and no need to rearrange any of them. The IRV method defines a “factor of scale” variable marked with α . This factor can be calculated by simply writing the original velocity vector's components into the inverse kinematic equations, and the results are the required wheel speeds. After that, the allowable maximum wheel speed has to be divided by these values to get α . Therefore, in this paper, α is not only known as a factor of scale but has more meaning and is called velocity reserve multiplier, marked with λ . In case of dynamics, it is called acceleration reserve multiplier, marked with σ .

In the same year, Jianhua Wu, Robert L. Williams II and Jae Lew [34] also presented phase spaces as velocity and acceleration cones for kiwi drives. The cones

were derived with linear transformations using kinematic and dynamic models. The form of the velocity cone is correct, but in case of the acceleration cone, they assumed continuous equal weight distribution on all wheels, therefore their cubic shape model should only be used when the vertical position of the center of gravity (CoG) is close to the ground, otherwise it can easily cause wheel slip. Similar disadvantageous dynamic modelling simplifications can be found in [16], [21]–[25], [33]–[36], [39], and [41]–[57]. In general, the neglected distinct load forces (a hidden simplification) are caused by 2D planar modelling of the dynamics or thinking only in the generalized coordinates (x , y linear position, and angle of the robot posture, and their first and second derivatives).

Also in 2006, O. Purvin and R. D'Andrea first presented a trajectory generation method [59], [60], in which the distinct load forces (called weight transfer in their paper) were taken into account in case of a four-wheeled, over-constrained mechanism. However, they did not utilize the extremal capabilities of the direction dependent acceleration envelope. They reduced it into a unidirectional cylinder.

In 2008, Chuntao Leng, Qixin Cao and Yanwen Huang [47] made an improved artificial potential field (iAPF) method for a four-wheel omnidirectional robot. This publication was the first that considered the distinct load forces on the wheels during acceleration, but they used the load estimation only for motion efficiency according to changing rolling resistance. They assumed invariable loads on the wheels for calculating wheel slip constrained maximum acceleration. Instead of using phase space, they derived an anisotropic function to deviate from the original output result of the dynamic APF method.

In 2008-2011, H. Huang, C. Tsai and S. Lin presented a possible adaptive robust solution for several uncertain effects including the time-varying wheel loads [61]–[64]. Their adaptive control law is an experimental solution based on planar dynamic modelling, and works in polar space. It is also hard to apply their theory due to its extreme high calculation demand. Similar to their later published PACO solution for kinematics, it required an FPGA-SoPC system's calculation throughput [30].

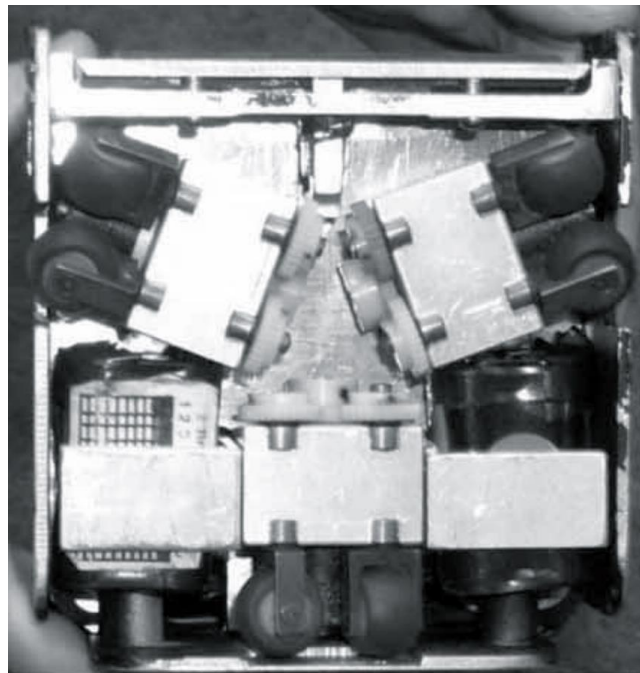
In 2009, J. Tar, J. Bitó, I. Gergely and L. Nádai published a dynamic model, which calculated the changing load forces [65]. However, their work did not focus on the traction of wheels. They applied positive non-zero constraints to load forces to avoid a tip-over situation and developed an adaptive PID control for trajectory tracking.

In 2015, B. Li, H. Du, W. Li and Y. Zhang published a dynamics for handling the height of the CoG [6], in case of a similar four-wheeled over-constrained mechanism as in case of [59]. But here, the drive scheme satisfies holonomic constraints by actuated caster wheels.

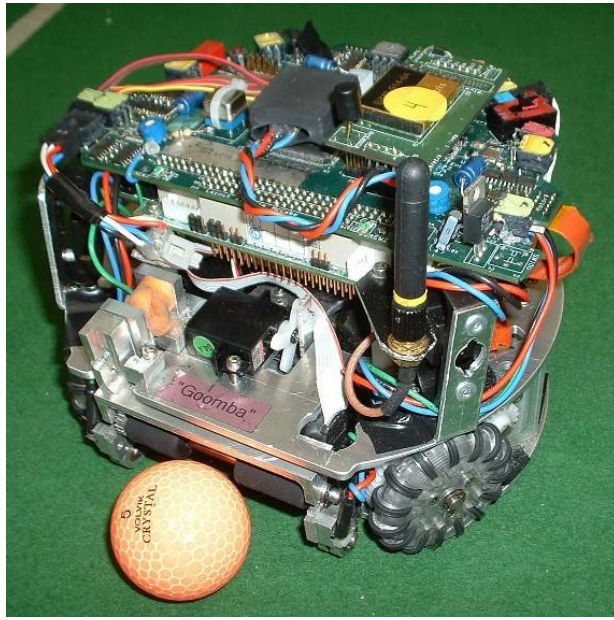
2.4 Relevant publications of Hungarian authors

Only few Hungarian authors published their results regarding holonomic mobile robots due to its specialty within the extensive field of general mobile robotics. However, some of the very few results played an important role in the evolution of holonomic mobile robot control.

Tamás Kalmár-Nagy was a co-author in several specific papers focused on the kinematics and the dynamics of holonomic mobile platforms. He started his specific experience by participating in the Cornell RoboCup Team who won the RoboCup 2000 competition in F180 (small size) category in Melbourne, Australia [66]. During that time, stock holonomic wheels for robots were rarely available. The team fabricated their own wheel constructions (see Fig. 7/a), which was based on a similar orthogonal concept as the early Killough's wheels [11].



(a)



(b)

Fig. 7. Robots of the Cornell RoboCup Team: Bottom view of the RoboCup 2000 winner (a), it used the same orthogonal wheel concept as Killough in 1994. A later design from 2004 (b), it used small rollers on the circumference of the wheel

Later on, they made “one-piece” omniwheels by small rollers on the circumference of the wheel (see Fig. 7/b), similarly to Jean-Daniel Nicoud’s technique at the Euromicro Micromouse robot competition in London, 1980. In the 2000s, the members of the Cornell RoboCup Team – including T. Kalmár-Nagy – published several papers about the innovative details of their successful robot: In 2002, they published a robot trajectory generation method constrained by kinematics and simplified dynamics at American Control Conference [24]. One year later, they extended their results with an updated robot mechanism, assembled with modern, two-row omniwheels. They defined the admissible controls as a rotated cuboid (as phase space of motor voltages) derived by linear transformation using simplified dynamics. Trajectory generation is based on a unidirectional conical phase space which was fully involved in the admissible cuboid [40]. This result was the first 3D phase space based approach in the field of the direction dependency of holonomic robots. In 2007, a near-optimal trajectory generation method was developed by using the same simplified dynamics caused by the 2D top view (x-y plane) approach, without considering the non-zero height of CoG [67]. In 2016, T. Kalmár-Nagy published a revised version of trajectory generation, based on the same simplified dynamics, and measured the theoretical results with a different, four-wheeled omnidirectional mechanism.

A comprehensive introduction of the 1999-2003 seasons of the multiple world champion Cornell RoboCup Team can be studied in [68].

During the past few years, Festo Didactic took a significant part in education and research with their stock holonomic robot, called Robotino [69]. The University of

Dunaújváros created an EEG based brain-to-computer interface based velocity controller for the omnidirectional Robotino [70]. At the Mechatronics Department of Budapest University of Technology, Robotino's state space model was presented with a simplified dynamic modelling, which neglected the wheels' inertia and the load distribution on the wheels [49].

2.5 Conforming with current high-level control platforms

Regarding results for the generation and tracking of time optimal trajectory, most methods apply constant velocity and acceleration limits to the robot body. Only a few of them deal with the possible maximum velocity and acceleration of the robot, which is rapidly changing during motion.

Although a number of proposals [24], [26], [46] handle the part of the non-linearity of the robot in different ways, still there is no practical approach that investigates the robot dynamics considering the effect of the height of the CoG and provides information on its limits for a feasible and robust implementation. The goal of this research was to define a reusable theory which conforms to existing, widely used mobile robot control practices, while being eligible for effortless and run-time efficient implementation.

Current high-level robot control platforms such as the Robot Operating System (ROS) [71] or the Mobile Robot Programming Toolkit (MRPT) [72] use constant limits at present. ROS and MRPT support velocity control mode by assigning a new velocity command to a mobile robot platform at each predefined time period. In fact, the decision about a new velocity command is not the result of an exact trajectory calculation as in the field of industrial robotics. Several online decision methods provide the new velocity reference based on real-time environment sensor data. The operation of these online reactive navigation methods is not strongly bounded to velocity and acceleration limits. The interpolation of a CNC machine fails to follow the exact trajectory if one of these boundary conditions is changed online. But practically, ROS has a local planner algorithm [73], which uses Dynamic Window Approach (DWA). DWA is not sensitive to parameter changes: it samples from the set of achievable velocities for just one simulation step given by the acceleration limits of the robot. Also, MRPT uses a Nearness Diagram (ND) Navigation [74] method for obstacle avoidance, which is a perception-action process, and it can simply work with updated velocity and acceleration limits as long as the limits are never set to zero.

The velocity limits are driven by the maximum speed of the wheels. Regarding the acceleration limits, the wheel slip, the tip-over situation and the maximum motor torque need to be taken into account. The overall result of these limits can also be provided to the high software level control in each command cycle as the allowed codomain of the new velocity command. This approach is necessary in order to make

the best use of the inherently changing characteristics of the robot in applications that require online path planning.

2.6 ISO Standardization

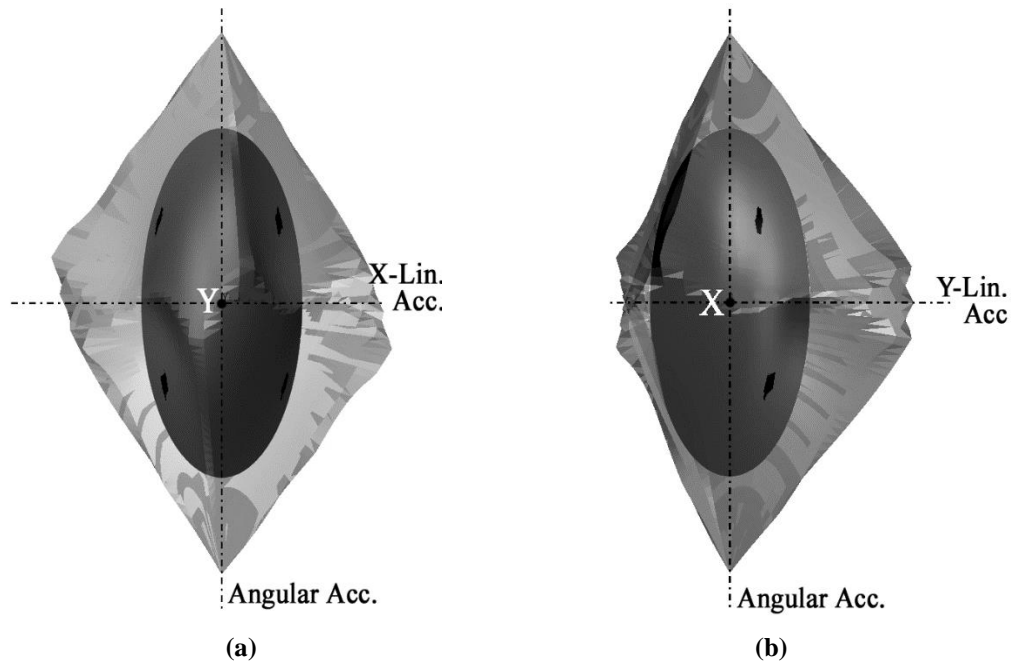
Currently, Industrial robots perform tasks in collaboration with humans in flexible and reconfigurable working environments, in manufacturing and beyond. In order to address the challenge of designing safety critical robot systems, ISO safety standards – such as ISO 10218 – have been regularly updated and extended over the last few years.

Today there are no standardized performance measurement criteria for mobile robots to compare different types of drive structures. Therefore, new standardization efforts have been started on service robots for medical and household applications in order to specify general safety requirements before serial products can enter the market. Apart from safety, other standardization efforts focus on the harmonization of terminology and the interchangeability of robot components. All standard development related to commercial mobile robots takes place in the ISO TC 184/SC 2 committee and is organized in Working Groups (WG). Several years ago, a study group on modular robot design was founded inside WG 8. One of its goals is to allow customers to easily compare the capabilities of different robots. WG 8 has started the development of a standard in order to measure performance. The current early draft includes instructions to measure speed, braking distance, climbing ability, etc. [75].

Clarification and demonstration of dynamic limitations can assist the standardization process. These limitations are not constant in case of holonomic mobile robots. Furthermore, the methodology of a (simple) benchmark measurement can be still different for the same type of robots if the geometry or the load distribution is different. Section 4 consists considerable proposals for the before mentioned problems.

3 PROPOSED PHASE SPACE TO DEFINE THE KINEMATIC AND DYNAMIC LIMITS OF HOLONOMIC WHEELED MOBILE ROBOTS

Time-optimal theories in the field of ground vehicles and mobile robots often use the friction circle model for modelling wheel slip [76]. But as the simple illustration of Fig. 6 shows, the direction-independent friction limits are not appropriate to avoid the wheel slip of omniwheels. Fig. 8 shows the calculated and verified acceleration space of a real kiwi drive platform with transparent body in the robot coordinate system. The solid body inside shows the possible maximum sized direction-independent assumption of the allowed acceleration vector set.



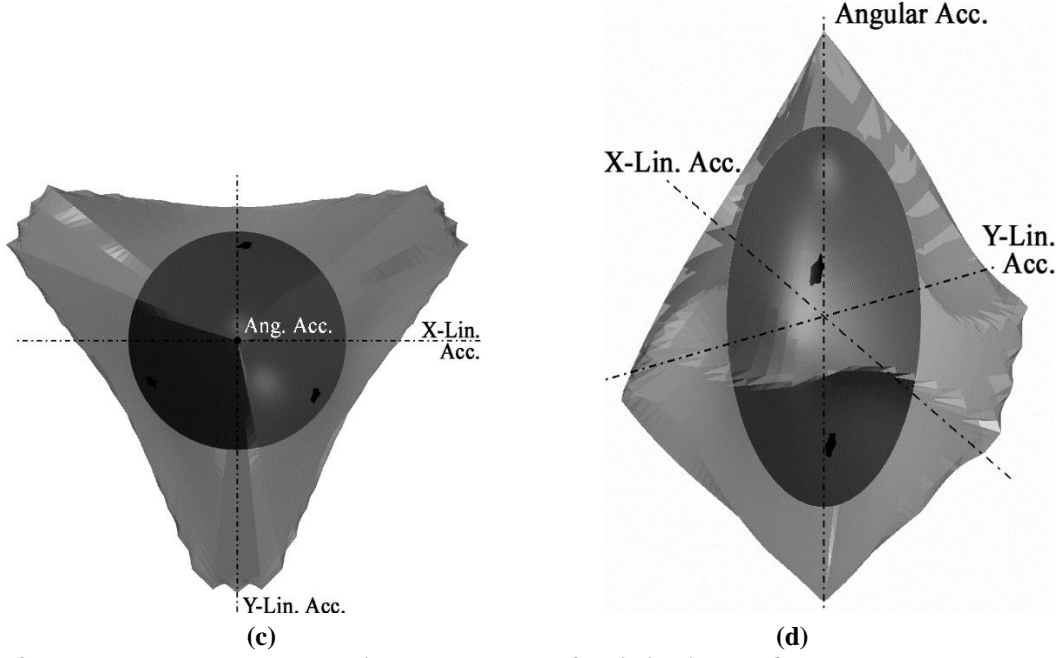


Fig. 8. Real and assumed acceleration phase spaces of a kiwi drive platform. The transparent body is the calculated and measurement-verified acceleration phase space. The solid body is the well-known and commonly used direction-independent model called friction circle. The volumetric difference represents the non-utilized capabilities of the robot dynamics. Axes x and y represent planar linear accelerations, and z represents angular acceleration. (a) is the x-z plane view, (b) is y-z plane view, (c) is x-y plane view, (d) is an isometric view.

As the volumetric difference shows, many valuable capabilities will be lost if the direction-independent assumption is used. Therefore, vector sets of allowed velocities and allowed accelerations have to be defined in a direction-dependent form in the field of all omniwheel based holonomic drives. These vector sets are marked as velocity space and acceleration space in the following sections [77]. In different applications, the similar kinematic and dynamic phase spaces of road vehicles were used to refine the snapping method of raw GPS tracks to roads [78], [79].

3.1 Practical application of direction dependent velocity and acceleration limits

The widely applied mobile robot control platforms like ROS or MRPT generate a semi-real-time velocity command based on the general target location and actual environment sensory data. The generated velocity preference ($v_{req}(n)$) should be further adjusted to conform with the robots motion state dependent mechanical capabilities. The servo controllers of the driving motors can be commanded after the kinematic and dynamic model based adjustments. The simplified block diagram of the control schema can be seen on Fig. 9.

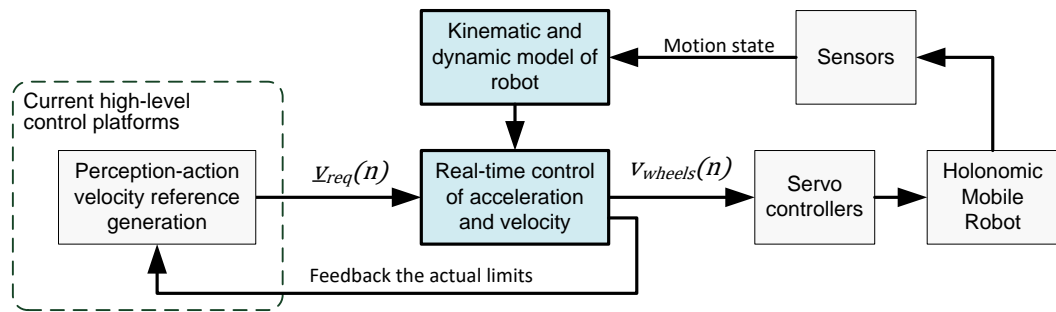


Fig. 9. Block diagram of control schema. The real-time controller of acceleration and velocity receives a preferred velocity command from the high-level robot control platform and adjust it according to the mechanical model and actual motion state of the robot.

Accept now that the strongly direction dependent velocity limits are changing smoothly (see later, in Section 5.1). Therefore, the actual limits (and the updated velocity reference) can be fed back to the local planner of the high-level control platform in order to adapt the next velocity preference to the current limits.

The following section describes the applied mechanical models, then the feasible realization of the derived control can be seen in Section 5.

4 MODELING OF OMNIWHEELED ROBOTS

The holonomic mobile robot platform is modeled as a rigid body. The robot motion can be described by the motion state of the CoG. The velocity and acceleration state of the robot body is described in the robot-coordinate system, which is fixed to the geometric center in the x-y directions and fixed to the floor in vertical direction (see Fig. 10).

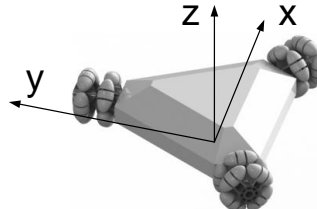


Fig. 10. Robot-coordinate system, fixed to the geometric center in the x-y direction and fixed to the ground in vertical direction.

The regular kiwi drive robot has three omnidirectional wheels, those axes are pointing to the geometric center of the robot body, and the wheels are placed to the circumference of the robot using equal spacing (120 degree angles between all axes).

4.1 Inverse kinematic model

Assumption I: The robot has n omniwheels in an optional arrangement.

Assumption II: The robot is modelled as a rigid body which moves on a two-dimensional, planar, horizontal surface.

Assumption III: The required linear and angular velocity of the CoG and their first derivatives are given.

Assumption IV: The CoG is in the geometric center of the robot in the x-y directions.

The velocity of the wheels can be calculated by the inverse kinematic equations (1, 2). First, the robot velocity vectors are calculated at each wheel contact point by the following equation:

$$\underline{v}_{A,i} = \underline{v}_{CoG} - \underline{\omega} \times \underline{r}_{A,i} \quad (1)$$

Where $\underline{v}_{A,i}$ is the linear velocity of the i^{th} wheel contact point, \underline{v}_{CoG} is the linear velocity of the CoG, $\underline{\omega}$ is the angular velocity of the robot, and $\underline{r}_{A,i}$ is the vector pointing from CoG to the corresponding wheel contact point.

The driving directional velocity vector ($\underline{v}_{drive,i}$) can be calculated for each wheel as the perpendicular projection of the contact point's velocity vector to the driving direction ($\underline{v}_{dir,i}$). (See Fig. 11.)

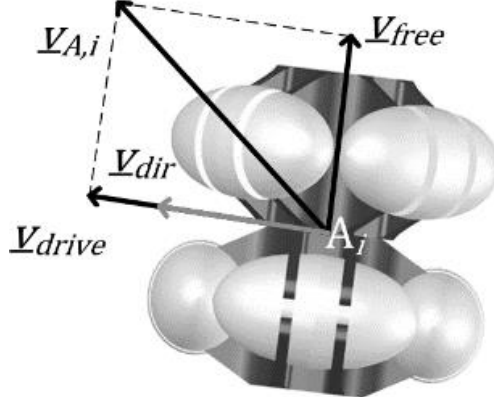


Fig. 11. Velocity vectors of an omnidirectional wheel (top view)

The cosine of the angle between two vectors can be calculated by their scalar multiplication. The drive speed of the wheel is as follows:

$$\underline{v}_{drive,i} = |\underline{v}_{A,i}| \frac{\underline{v}_{A,i} \cdot \underline{v}_{dir,i}}{|\underline{v}_{A,i}| \cdot |\underline{v}_{dir,i}|} \quad (2)$$

4.2 Calculating maximum velocities

In order to evaluate a feasible motion control, it is required to calculate the maximum velocity of the robot that can be achieved without exceeding the maximum velocity limits of the drives. According to *Assumption III*, the reference velocity of the CoG is given. A velocity reserve multiplier (λ) is proposed to express the maximum velocity of the CoG from the reference velocity of the CoG.

$$\underline{\omega}_{max} = \lambda \underline{\omega} \quad \underline{v}_{CoG,max} = \lambda \underline{v}_{CoG} \quad (3)$$

Where $\underline{\omega}$ is the angular velocity vector and \underline{v} is the linear velocity vector of CoG. λ can be calculated by the following formula because the inverse kinematics is expressed with linear equations for of any kinds of omniwheel based platforms:

$$\lambda = \min \left(\frac{v_{drive,i,max}}{|\underline{v}_{drive,i}(\underline{v}_{CoG}, \underline{\omega})|} \right) \quad (4)$$

Where $V_{drive,i,max}$ is the maximum velocity of the wheel. If the velocity reserve is above one, the robot is capable of reaching higher velocity. Under one, the robot reference velocity needs to be reduced to avoid actuator saturation.

The defined velocity reserve multiplier yields a representative index number, showing the amount of utilized resource during online computation. Using this definition, the implementation of a velocity limiter algorithm is greatly simplified compared to the previous IRV method [41] or to the linear transformation [34]. The main reason for simplification is that the computation uses the inverse kinematic equations which need to be computed in any case for driving a robot. The calculation example is presented later in Section 5.1.

No Jacobian matrix was used here to describe kinematics, because different Jacobian matrices can be derived for different omniwheeled robots. In our case, only linearity is important, therefore the velocity space can be applied to any kind of omniwheel arrangement (*Assumption I*).

4.3 Velocity phase space in case of a kiwi drive

This subsection defines the velocity phase space of regular kiwi drive robot by using the general inverse kinematic equations described before. The maximum velocity vectors can be represented by three scalars in case of the two-dimensional, planar, and horizontal surface. These velocities can be described by taking the first derivative of the generalized coordinates of the robot posture:

$$\underline{q} = \begin{bmatrix} q_x \\ q_y \\ \varphi_z \end{bmatrix} \quad (5)$$

$$\dot{\underline{q}}_{\max} = \begin{bmatrix} v_{CoG\ x,\max} \\ v_{CoG\ y,\max} \\ \omega_{z,\max} \end{bmatrix} = \lambda \begin{bmatrix} v_{CoG\ x} \\ v_{CoG\ y} \\ \omega_z \end{bmatrix} \quad (6)$$

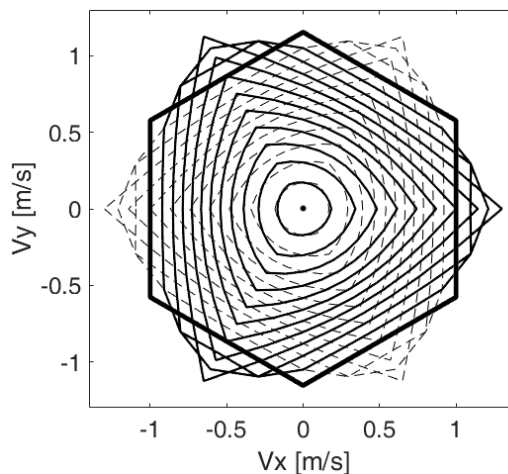


Fig. 12. Maximum linear velocities depending on direction and angular velocity. The bold hexagon corresponds to the limit of linear velocity when the angular velocity is zero. As the angular velocity grows (thick solid lines), the maximum linear velocity is often reduced. The dot in the center shows that the maximum linear velocity is zero when the robot is rotating with the maximum angular velocity. The dashed lines represents the linear velocity limit in case of negative angular velocity.

The maximum linear velocity can be plotted on a polar diagram that shows the maximum vector length, depending on the direction of the velocity vector (bold hexagon in Fig. 12). More curves for different angular velocities can be plotted. As it can be assumed, the maximum linear velocity is often reduced if the angular velocity grows. But as Fig. 12 shows, there are some exceptions: In some cases, the robot can increase linear velocity if it rotates during linear movement.

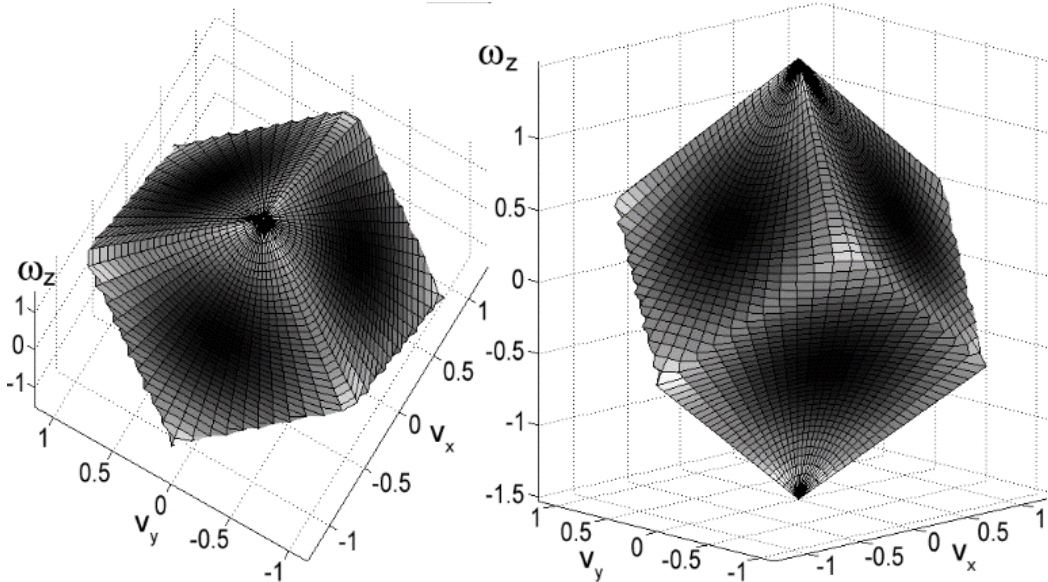


Fig. 13. Vector set of feasible velocities in the velocity space. Linear velocities are represented by the x and y axes, and angular velocity is represented by the z axis. The shade of the surface represents the distance of the surface from the origin, which is equal to the maximum length of the velocity vector.

The velocity vector (\underline{v}_{CoG}) has to be an element of the velocity phase space ϕ_v . The vector set of allowed velocities is as follows:

$$\underline{\dot{q}} \in \phi_v \quad (7)$$

That vector set forms a 3D body in the velocity space (see Fig. 13), because the robot posture has three dimensions. The x and y axes represent linear velocities and the z axis represents angular velocity. The grayscale shade of the surface represents the distance from the origin, which is equal to the length of the velocity vector.

4.3.1 Utilizing the peripheral areas of velocity phase space of kiwi drive robots

Wu, Jianhua, Williams, Robert L. Lew, and Jae [34] defined a unidirectional velocity cone (similar to the direction-independent phase space, marked with a solid body in Fig. 8), which highly restricts the kinematic capabilities of the robot by constraining lower, direction-independent maximum linear velocity. This restriction simplifies the path planning, as any general (Wheeled Mobile Robot) WMR path planner can be used to navigate the robot. However, significant capabilities of the kinematic characteristics remain unutilized due to the simplification mentioned before.

Notice that the ND and the DWA path planner algorithms of ROS and MRPT, respectively (described in details in Section 2.4), can handle non-constant extreme values of velocity and acceleration. Due to these characteristics, the widely applied path planner algorithms do not inhibit the feasible utilization of peripheral volumes in the phase space which are outside the trivial direction-independent velocity cones. The following part of this subsection reveals the hidden capabilities of the phase space volumes mentioned before.

In order to demonstrate the benefit, different directional extreme values of the length of the velocity vector are considered. Fig. 14 marks grey areas of the velocity space, where higher linear velocity can be achieved by accepting non-zero angular velocity.

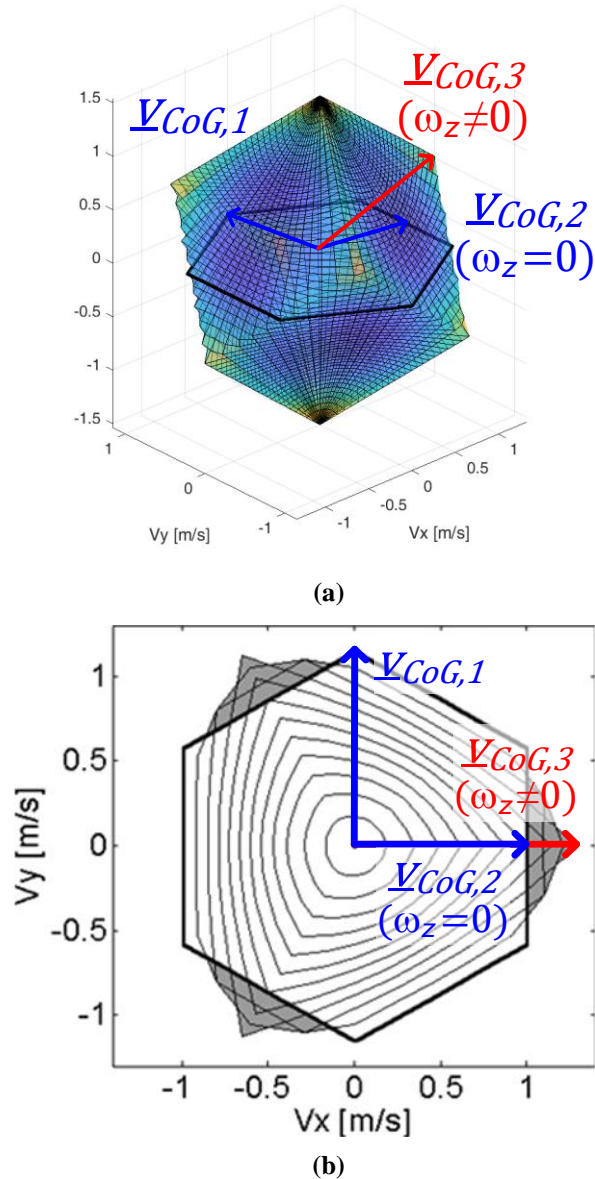


Fig. 14. 3D (a) and bottom view (b) of the velocity phase space. The bolded line hexagon shows the maximum linear velocity in case the angular acceleration is zero. The gray areas show the special areas where the linear velocity is higher while the angular velocity is non-zero.

The figure also marks three different possible extreme linear velocity vectors, where in case of the third ($\underline{v}_{CoG,3}$, marked with red) one the angular velocity is non-zero. The relative maximum absolute values of each linear velocity vector ($\underline{v}_{CoG,i}$) can be calculated by using the Jacobian form of kinematic constraints (9), constraining the maximum absolute values of the drive directional wheel velocities to one (8).

$$v_{drive,i} \in [-1 \dots 1] \quad (8)$$

$$\begin{bmatrix} v_{CoG,x} \\ v_{CoG,y} \\ \omega_z \end{bmatrix} = \begin{bmatrix} \frac{2}{3} & -\frac{1}{3} & -\frac{1}{3} \\ 0 & \frac{\sqrt{3}}{3} & -\frac{\sqrt{3}}{3} \\ -\frac{1}{3r} & -\frac{1}{3r} & -\frac{1}{3r} \end{bmatrix} \begin{bmatrix} v_{drive,1} \\ v_{drive,2} \\ v_{drive,3} \end{bmatrix} \quad (9)$$

The given maximum relative values for wheel velocities and the corresponding maximum relative velocity vectors in case of the generalized coordinates:

$$\begin{bmatrix} v_{drive,1} \\ v_{drive,2} \\ v_{drive,3} \end{bmatrix} := \begin{bmatrix} 0 \\ 1 \\ -1 \end{bmatrix} \Rightarrow \begin{bmatrix} v_{CoG,1,x} \\ v_{CoG,1,y} \\ \omega_{1,z} \end{bmatrix} = \begin{bmatrix} 0 \\ \frac{2\sqrt{3}}{3} \\ 0 \end{bmatrix} \cong \begin{bmatrix} 0 \\ 1.1547 \\ 0 \end{bmatrix} \quad (10)$$

$$\begin{bmatrix} v_{drive,1} \\ v_{drive,2} \\ v_{drive,3} \end{bmatrix} := \begin{bmatrix} 1 \\ -0.5 \\ -0.5 \end{bmatrix} \Rightarrow \begin{bmatrix} v_{CoG,2,x} \\ v_{CoG,2,y} \\ \omega_{2,z} \end{bmatrix} = \begin{bmatrix} 1 \\ 0 \\ 0 \end{bmatrix} \quad (11)$$

$$\begin{bmatrix} v_{drive,1} \\ v_{drive,2} \\ v_{drive,3} \end{bmatrix} := \begin{bmatrix} 1 \\ -1 \\ -1 \end{bmatrix} \Rightarrow \begin{bmatrix} v_{CoG,3,x} \\ v_{CoG,3,y} \\ \omega_{3,z} \end{bmatrix} = \begin{bmatrix} \frac{4}{3} \\ 0 \\ \frac{1}{3r} \end{bmatrix} \quad (12)$$

In the case of (12), the length of the linear velocity vector is 15.47% higher compared to (10):

$$\Lambda = \frac{\frac{4}{3}}{\frac{2\sqrt{3}}{3}} = \frac{2\sqrt{3}}{3} \cong 1.1547 = 115.47\% \quad (13)$$

Where Λ marks the ratio of maximum possible linear velocities in case of non-zero and zero angular velocity constraints.

The path planners restricted by the trivial direction independent velocity cone can only use (11) as maximum linear velocity. Consequently, in comparison with the proposal of [34], the utilization of case (12) eventuates in 33.3% additional benefit.

This comparison is shown in Fig. 15. In case of moving on a linear path, the velocity of the 2nd and 3rd wheels have to be reduced by half in order to get a straight path (see Eq. (11)). If these wheels are rotating with higher or maximum velocities, the

overall linear velocity of the robot will be reasonably higher. However, in this case the robot is moving on a circular curved path instead of a straight one.

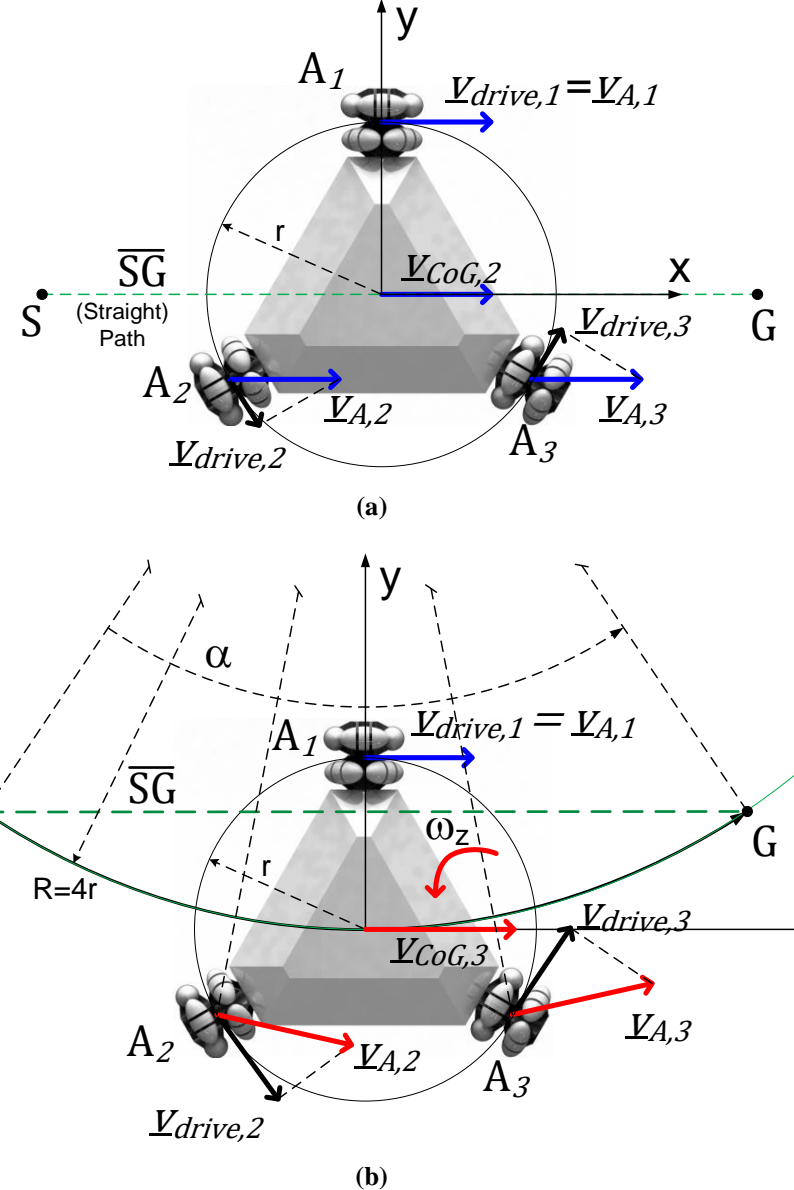


Fig. 15. Comparison of actual velocity vectors of the linear movement (a) with the corresponding rotating movement (b). In the second case, the absolute value of the linear velocity vector of the robot ($\underline{v}_{CoG,3}$) is 33.3% higher compared to the first case ($\underline{v}_{CoG,2}$)

Consequently, a hypothesis can be formulated by considering (13) and the above demonstration.

Hypothesis:

Can the robot reach a nearby goal position within a shorter duration by driving it along a longer circular path instead of the shortest straight one?

In order to evaluate the theory above, straightforward geometric consequences and the assumption of constant velocity were taken into account. The marginal utility of the curved path can be calculated by comparing the benefit of the available higher velocity with the additional length of the curved path.

The radius of the circular path (R) is equal to four times the radius of the circle coincident with the wheels (r), because the tangential velocity in case of Fig. 15 (b) is:

$$v_{CoG,3,x} = \omega_{3,z} \cdot R \quad (14)$$

Substituting and solving (14) will yield:

$$\frac{4}{3} = \frac{1}{3r} \cdot R \quad \Rightarrow \quad R = 4r \quad (15)$$

The length of the straight (16) and circular paths (17), respectively:

$$\overline{SG} = 2R \cdot \sin\left(\frac{\alpha}{2}\right) \quad (16)$$

$$\widehat{SG} = R \cdot \alpha, \quad (17)$$

where α is the total rotation of the robot body between the start and goal positions. See Fig. 15.

According to Equation (13), the marginal value of α is the non-zero solution of the following equation:

$$\overline{SG} \cdot \Lambda = \widehat{SG} \quad (18)$$

Substituting (16) and (17):

$$2R \sin\left(\frac{\alpha}{2}\right) \cdot \frac{2\sqrt{3}}{3} = R\alpha \quad (19)$$

Non-zero positive approximate solution for α :

$$\alpha \cong 1.83 \text{ [rad]} = 104.9 \text{ [deg]} \quad (20)$$

Substituting (15) and (20) into (16) will yield the length of the straight path representing marginal utility, where the duration of taking the straight and the curved path is equal.

$$\overline{SG}_{marginal} \cong 8r \cdot \sin\left(\frac{1.83}{2}\right) = 6.34r \quad (21)$$

The goal positions closer than this marginal distance can be reached within a shorter time along the circular path. The derivation of this result verifies the previously stated hypothesis, therefore, the following thesis can be formulated:

Thesis 1

Performing a movement between two positions takes less time for a 3-wheeled omnidirectional kiwi drive robot if it moves along a circular path in cases when the linear distance between the two positions is less than six times the radius of the circle coincident with the wheels.

Author publications in connection with the above thesis: [P1, P2, P4-P9, P20]

In practice, Ethon robots (used for evaluation) can reduce travel time to 90% of the original time along a one meter long distance:

Solving (16) for α by substituting the r parameter of the Ethon robot:

$$\overline{SG} = 8 \cdot 0.3 \cdot \sin\left(\frac{\alpha}{2}\right) = 1 \text{ [m]} \quad \Rightarrow \quad \alpha = 0.86 \text{ [rad]} \quad (22)$$

The length of the corresponding circular path is:

$$\widehat{SG} = 4r \cdot \alpha = 1.032 \text{ [m]} \quad (23)$$

The reduced relative time:

$$\frac{\widehat{SG}}{\overline{SG}} = \frac{1.032}{1} = 0.894 \cong 90\% \quad (24)$$

This means that travel time is reduced to 90% of the original time which is needed to take the one meter distance on the trivial straight path.

4.4 Inverse dynamic model

In practice, when velocity is at a lower rate, the acceleration limit problem can be solved by calculating the maximum accelerations; those can be achieved without exceeding the value of the friction coefficient. But when the wheel speed is at a higher rate, the electric motors that drive the wheels may not be able to produce enough torque to achieve wheel slip. In this case, the acceleration limit of the robot is constrained by the obtainable motor torque. Therefore, the torque-velocity characteristics of the motors also have to be considered. Finally, robots with higher CoG can tip over during a

powerful acceleration. All these three cases are investigated in connection with robot dynamics.

Assumption I of the kinematic model was further restricted to 3-wheeled kiwi drive for the rest of this subsection.

Based on *Assumption II*, the force and torque equations of the rigid body are used in order to construct the dynamic model of the robot.

According to *Assumption III*, the required linear and angular acceleration of the CoG is given.

(*Assumption IV* is still stated: The CoG is in the geometric center of the robot in the x-y directions.)

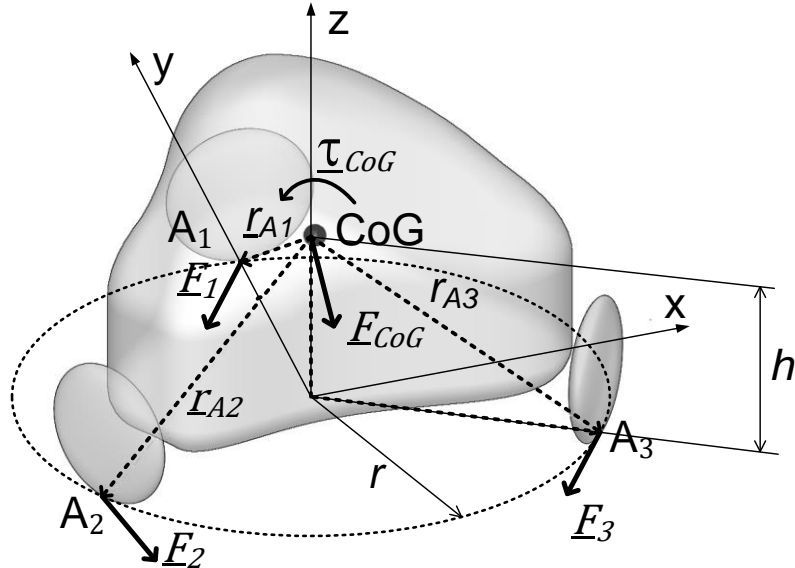


Fig. 16. Mechanic model of a three omniwheel based kiwi drive mobile robot platform

Fig. 16 explains the notations used in dynamic modeling: h is the height of the CoG from the ground plane; \underline{r}_{A1} , \underline{r}_{A2} , and \underline{r}_{A3} are vectors in the robot's coordinate system, pointing to the wheel's gripping points from the CoG; \underline{F}_1 , \underline{F}_2 , and \underline{F}_3 are wheel forces; \underline{F}_{CoG} and $\underline{\tau}_{CoG}$ are the force and torque vectors related to the CoG.

The $\underline{r}_{A,i}$ vectors of the kiwi platform according to Fig. 16:

$$\underline{r}_{A1} = \begin{bmatrix} 0 \\ r \\ -h \end{bmatrix}; \quad \underline{r}_{A2} = \begin{bmatrix} -\frac{\sqrt{3}}{2}r \\ -\frac{1}{2}r \\ -h \end{bmatrix} \quad \underline{r}_{A3} = \begin{bmatrix} \frac{\sqrt{3}}{2}r \\ -\frac{1}{2}r \\ -h \end{bmatrix} \quad (25)$$

The axial component (free rolling direction, see \underline{v}_{free} in Fig. 11) of the wheel force vector is zero. Therefore, the wheel forces can be split to load and drive components using radial and tangential unit vectors, respectively; see Fig. 17.

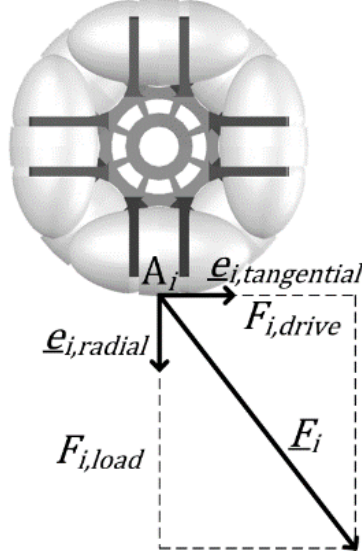


Fig. 17. Tangential and radial components of the wheel force

$$\underline{F}_i = F_{i,drive} \cdot \underline{e}_{i,tangential} + F_{i,load} \cdot \underline{e}_{i,radial} \quad (26)$$

Where $\underline{e}_{i,radial}$ and $\underline{e}_{i,tangential}$ are the unit vectors in the wheel coordinate system.

The \underline{F}_i wheel forces of the kiwi platform, expressed in the robot coordinate system, considering (26) and Fig. 16:

$$\underline{F}_1 = \begin{bmatrix} F_{1,drive} \\ 0 \\ F_{1,load} \end{bmatrix} \quad \underline{F}_2 = \begin{bmatrix} -\frac{1}{2}F_{2,drive} \\ \frac{\sqrt{3}}{2}F_{2,drive} \\ F_{2,load} \end{bmatrix} \quad \underline{F}_3 = \begin{bmatrix} -\frac{1}{2}F_{3,drive} \\ -\frac{\sqrt{3}}{2}F_{3,drive} \\ F_{3,load} \end{bmatrix} \quad (27)$$

The sum of load forces is equal to the vertical force caused by gravity, therefore the force and torque equations of the robot body:

$$\underline{F}_{CoG} = \begin{bmatrix} F_{CoG,x} \\ F_{CoG,y} \\ mg \end{bmatrix} = \underline{F}_1 + \underline{F}_2 + \underline{F}_3 \quad (28)$$

$$\underline{\tau}_{CoG} = \begin{bmatrix} 0 \\ 0 \\ \tau_{CoG,z} \end{bmatrix} = \underline{r}_{A1} \times \underline{F}_1 + \underline{r}_{A2} \times \underline{F}_2 + \underline{r}_{A3} \times \underline{F}_3 \quad (29),$$

where m is the mass of the rigid body. In case of the kiwi robot, drive and load directional force components are expressed as equations (30-35) to assist implementation described in Section 5.4 and the understanding of further chapters.

$$F_{1,drive} = -\frac{\tau_{CoG,z} - 2rF_{CoG,x}}{3r} \quad (30)$$

$$F_{1,load} = -\frac{2hF_{CoG,y} - rF_{CoG,z}}{3r} \quad (31)$$

$$F_{2,drive} = -\frac{\sqrt{3}(\sqrt{3}\tau_{CoG,z} - 3rF_{CoG,y} + \sqrt{3}rF_{CoG,x})}{9r} \quad (32)$$

$$F_{2,load} = \frac{hF_{CoG,y} + rF_{CoG,z} + \sqrt{3}hF_{CoG,x}}{3r} \quad (33)$$

$$F_{3,drive} = \frac{\tau_{CoG,z} + rF_{CoG,x} + \sqrt{3}rF_{CoG,y}}{3r} \quad (34)$$

$$F_{3,load} = \frac{\sqrt{3}(\sqrt{3}hF_{CoG,y} - 3hF_{CoG,x} + \sqrt{3}rF_{CoG,z})}{9r} \quad (35)$$

In case of a rigid body, force and torque can be expressed with accelerations in the following form:

$$\underline{F}_{CoG} = m \cdot \underline{a}_{CoG}, \quad \underline{\tau}_{CoG} = \underline{I}_{CoG} \cdot \underline{\xi} \quad (36),$$

where \underline{a} is the linear acceleration vector of the CoG, \underline{I} is the inertia matrix, and $\underline{\xi}$ is the angular acceleration vector. Substituting (36) into equations (30-35), the load and drive directional wheel force components are obtained from the given required robot acceleration state.

4.5 Defining the friction reserve multiplier

Using the Coulomb friction model, the maximum allowed drive force that can be applied to a wheel without slipping depends on the wheel load force and the Coulomb friction coefficient (μ):

$$\left| \frac{F_{i,drive}}{F_{i,load}} \right| = < \mu \quad (37)$$

By expressing the wheel force components with (36), the required friction coefficient is obtained for each wheel from the given required acceleration vectors:

$$\left| \frac{F_{i,drive}(\underline{\xi}, \underline{a}_{CoG})}{F_{i,load}(\underline{\xi}, \underline{a}_{CoG})} \right| = \mu_{i,required} < \mu \quad (38)$$

Dividing the available friction coefficient by the required friction coefficient yields a friction reserve multiplier. The lowest value has to be chosen to prevent any of the wheels from slipping.

$$\sigma_f = \min \left(\frac{\mu}{\mu_{i,required}} \right) \quad (39)$$

The dynamics are expressed with linear equations (30-36), therefore the possible maximum accelerations can be expressed with the friction reserve multiplier for each acceleration vector:

$$\underline{a}_{CoG,max} = \sigma_f \underline{a}_{CoG}, \quad \underline{\xi}_{max} = \sigma_f \underline{\xi} \quad (40)$$

The friction reserve multiplier can also be called wheel slip based acceleration reserve multiplier. The validation of the wheel slip based acceleration space is based on direction dependent acceleration tests described in Section 5.5.

4.6 Maximum acceleration of the robot considering the maximum torque of electric motors

In the previous subsection, maximum acceleration was calculated to avoid the occurrence of wheel slip. The motor torque limit at an appropriate motor velocity has to be further considered. The goal is to express the maximum acceleration in the robot coordinate system that is achievable at the actual linear and angular velocity. In this paper, a direct drive robot with DC motors is investigated. The characteristics of achievable torque based acceleration space do not change in case of gearboxes and different types of electric motors: only the scale varies.

In our case (and in most cases), the electrical time constant of the motor is smaller than the mechanical one by two orders of magnitude, therefore the armature inductance can be neglected. A close estimation of the maximum output torque of the motor at maximum armature voltage can be obtained by:

$$\tau_{i,max}(\Omega_i) = \frac{(V_{a,max} - k\phi\Omega_i)k\phi}{R_a} \quad (41),$$

where $k\phi$ is the speed constant of the DC motor and Ω is the angular velocity in rad/s of the armature shaft. $V_{a,max}$ is the maximum armature voltage and R_a is the armature resistance. We can express Ω from the drive directional velocity (Fig. 11) of the appropriate wheel:

$$\Omega_i = \frac{v_{i,drive}}{r_{wheel}} \quad (42),$$

where r_{wheel} is the radius of the wheel. The maximum torque can be expressed with the maximum force of the wheel in the driving direction:

$$\tau_{i,max} = F_{i,drive,max} \cdot r_{wheel} \quad (43)$$

Substituting (42) and (43) into (41) yields the maximum force of the wheel depending on the maximum velocity of the wheel:

$$F_{i,drive,max}(v_{i,drive}) = \frac{(v_{a,max} - \frac{k\phi v_{i,drive}}{r_{wheel}})k\phi}{R_a \cdot r_{wheel}} \quad (44)$$

Dividing the available drive forces by the required drive forces, a motor torque reserve multiplier σ_t could be phased in. Following the calculation for each wheel, the lowest result has to be considered as a limit, similar to the case of the velocity reserve multiplier.

$$\sigma_t = \min \left(\frac{F_{i,drive,max}(v_{i,drive})}{F_{i,drive}(\underline{\xi}, \underline{a}_{CoG})} \right) \quad (45)$$

There is a linear relationship between forces and accelerations, therefore maximum accelerations can be expressed with a motor torque related acceleration reserve multiplier.

$$\underline{a}_{CoG,max} = \sigma_t \underline{a}_{CoG}, \quad \underline{\xi}_{max} = \sigma_t \underline{\xi} \quad (46)$$

4.7 Calculating the maximum acceleration of the robot avoiding a tip-over situation

The robot can tip over during a powerful acceleration if the vertical position of the CoG (h in Fig. 16) and the friction coefficient are relatively high [80]. At the time when the tip-over starts, the load force of one of the wheels (31, 33, 35) becomes zero. Therefore, the solution of the following inequality for each wheel will present the limits for a given linear acceleration vector:

$$F_{i,load}(\underline{a}_{CoG}) > 0 \quad (47)$$

The wheel load forces are independent of the angular acceleration. The solution of inequality (47) is trivial in case two of the linear acceleration vector components (z and x or y directional) are zero. If x and y directional components are non-zero, the following solution is proposed: the direction of the linear acceleration vector is fixed and the maximum length of the vector needs to be calculated. As the ratio of vector components is constant, $a_{CoG,x}$ and $a_{CoG,x,max}$ can be expressed in the following form, proposing a c scalar multiplier:

$$a_{CoG,x} = c a_{CoG,y}, \quad a_{CoG,x,max} = c a_{CoG,y,max} \quad (48)$$

(This c multiplier can also be expressed by obtaining the tangent of the direction of the linear acceleration vector in the x-y plane.) Substituting (48) into the wheel load forces, the maximum accelerations can be calculated by solving the inequalities below

for each wheel. The results are relevant in the unsafe direction; the acceleration in the opposite direction can be infinite by the side of the actual wheel.

The criteria of the first wheel can be calculated by expressing (31) with acceleration:

$$F_{1,load} = -\frac{2hma_{CoG,y1}-rmg}{3r} > 0 \quad (49)$$

Solving (49) yields:

$$-\infty < a_{CoG,y1} < \frac{gr}{2h} \quad (50)$$

The criteria of the second wheel can be calculated by expressing (33) with (48) and with acceleration:

$$F_{2,load} = \frac{h m a_{CoG,y2} + r m g + \sqrt{3} h m c a_{CoG,y2}}{3r} > 0 \quad (51)$$

Solving (51) yields:

$$\begin{cases} if -\frac{gr}{h+\sqrt{3}ch} < 0 \Rightarrow -\frac{gr}{h+\sqrt{3}ch} < a_{CoG,y2} < \infty \\ if -\frac{gr}{h+\sqrt{3}ch} > 0 \Rightarrow -\infty < a_{CoG,y2} < \frac{gr}{h+\sqrt{3}ch} \end{cases} \quad (52)$$

The criteria of the third wheel can be calculated by expressing (35) with (48) and with acceleration:

$$F_{3,load} = \frac{\sqrt{3}(\sqrt{3}h m a_{CoG,y3} - 3h m c a_{CoG,y3} + \sqrt{3}r m g)}{9r} > 0 \quad (53)$$

Solving (53) yields:

$$\begin{cases} if -\frac{\sqrt{3}(gr)}{\sqrt{3}h - 3ch} < 0 \Rightarrow -\frac{\sqrt{3}(gr)}{\sqrt{3}h - 3ch} < a_{CoG,y3} < \infty \\ if -\frac{\sqrt{3}(gr)}{\sqrt{3}h - 3ch} > 0 \Rightarrow -\infty < a_{CoG,y3} < -\frac{\sqrt{3}(gr)}{\sqrt{3}h - 3ch} \end{cases} \quad (54)$$

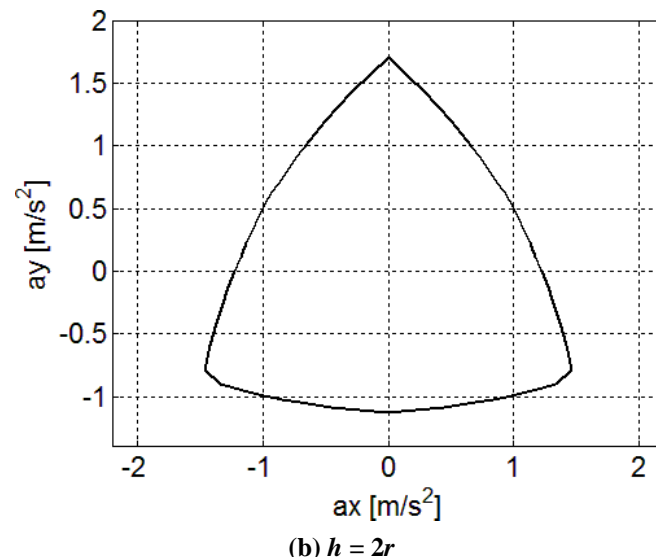
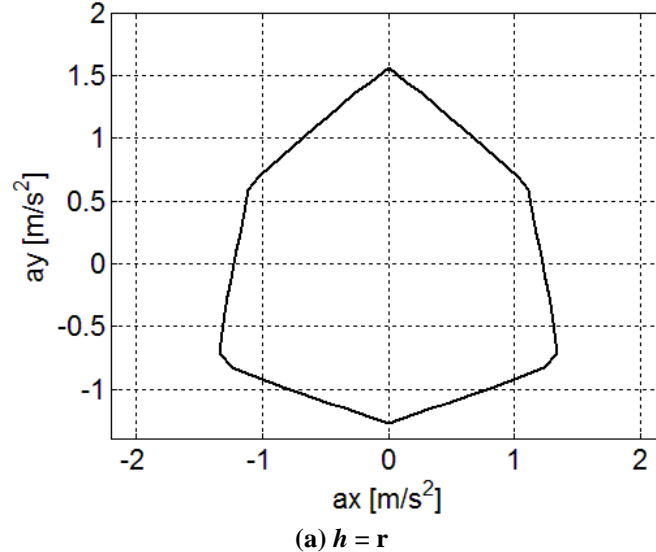
$a_{CoG,x,i}$ can be expressed by substituting (48) to (52) and (54). To avoid a tip-over situation in all three directions, the intersection of the three compound inequalities needs to be considered.

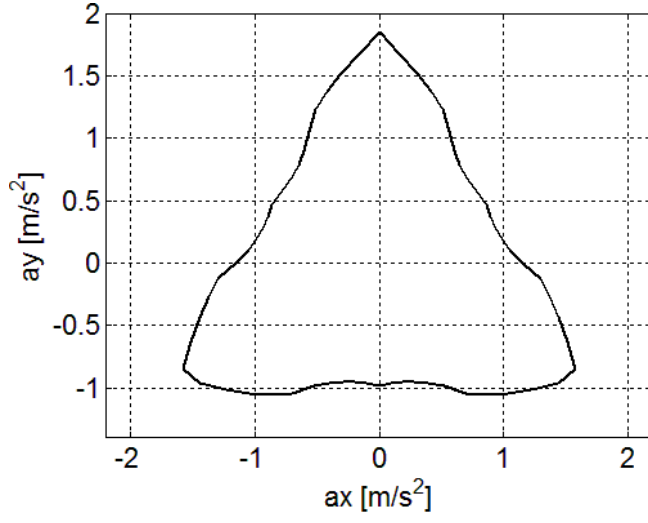
4.8 Visualizing the acceleration space

The robot acceleration vector expressed in generalized coordinates has to be an element of the acceleration phase space ϕ_a , the vector set of allowed accelerations:

$$\underline{\dot{q}} \in \phi_a \quad (55)$$

The acceleration limit of those caused by wheel slip is a constant phase space; it is independent from the motion state of the robot; its characteristics only depend on constant robot parameters (r, h , see Fig. 16). This can be visualized in Fig. 18 for different heights of the CoG (h) related to the radius (r) of the circle coincident with the wheels. It shows the x - y section plane where the angular acceleration is zero.



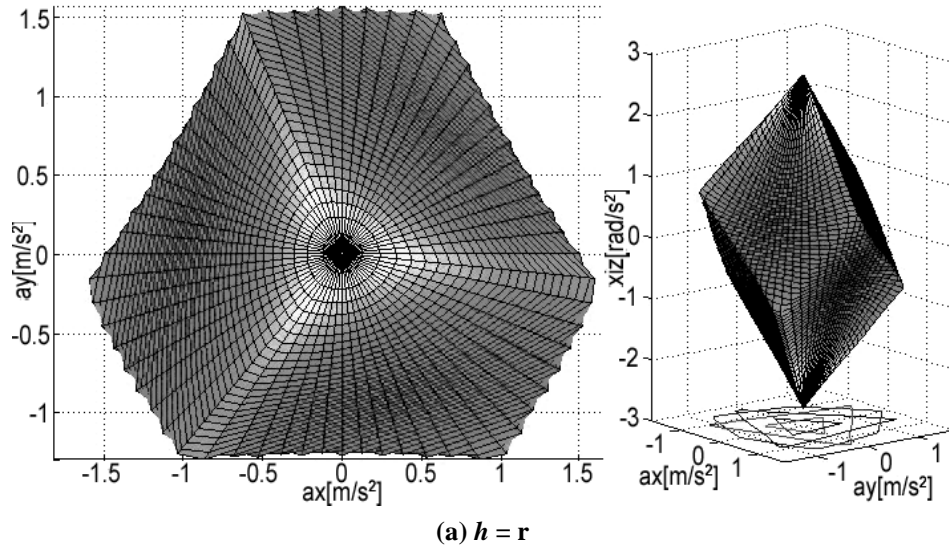


(c) $h = 3r$

Fig. 18. *x-y section plane of the wheel slip constrained acceleration phase space, for different heights of the CoG (h) related to the radius (r) of the circle coincident with the wheels when the angular acceleration is zero*

Similar to the velocity, the acceleration vector set forms a 3D body in the acceleration space. Fig. 19 shows the wheel slip based acceleration phase space. Axes x and y represent linear accelerations and axis z represents angular acceleration. The shade of the surface represents the distance from the origin, which is equal to the length of the acceleration vector.

If h was zero (which is not possible in case of a real robot) the shape of the acceleration phase space diagram would be the same as that of the velocity diagram [34]. Normally, the load density between wheels is unequal during acceleration; hence the diagram is significantly distorted compared to the velocity phase space.



(a) $h = r$

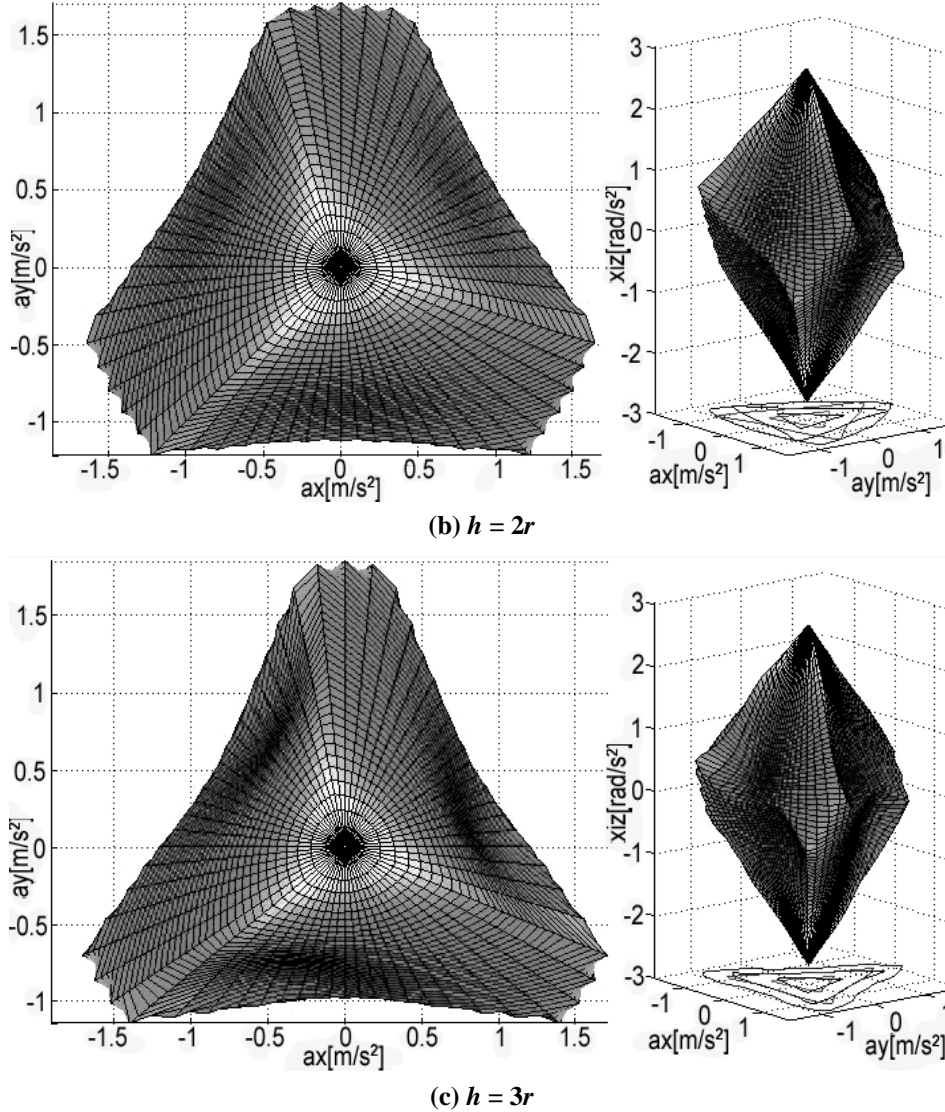


Fig. 19. Acceleration phase space constrained by wheel slip. The shade of the surface represents the distance of the surface from the origin, which is equal to the maximum length of the acceleration vector.

The shape of the constrained acceleration phase space of the motor torque is the same as in the case of the velocity, see Fig. 13. Only the scale varies as the actual maximum torque of the motor changes depending on the actual velocity.

The acceleration space caused by the tip-over constraint does not depend on angular acceleration. Hence only the x - y section of the space is informative, and it shows the boundary of the safe area for the linear acceleration vector (see Fig. 20).

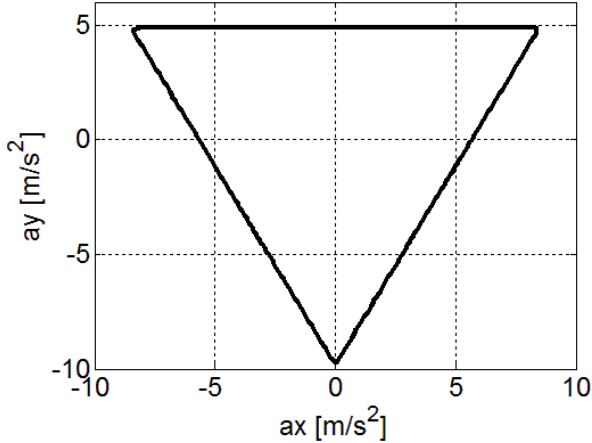


Fig. 20. The x-y section plane of the tip-over situation constrained acceleration phase space

The overall acceleration space of the robot will be the intersection of the three acceleration spaces constrained by wheel slip, motor torque and the tip-over situation.

4.9 Investigation of 3D phase spaces

3D kinematic and dynamic phase spaces (or velocity and acceleration spaces, respectively) can describe the limits of all planar mobile robots when the motion state of the robot body is described by 3 DoF generalized coordinates. However, the “as-is” true visualization is still hard to be used for further objective performance measurements to differentiate the robots’ similar types of capabilities in measurable scalar scales.

4.9.1 Braking distance and climbing ability

Braking distance (for safety) or climbing ability can be trivially defined by picking the minimum and maximum linear accelerations from the section of the acceleration space where the angular acceleration is zero (see Fig. 21).

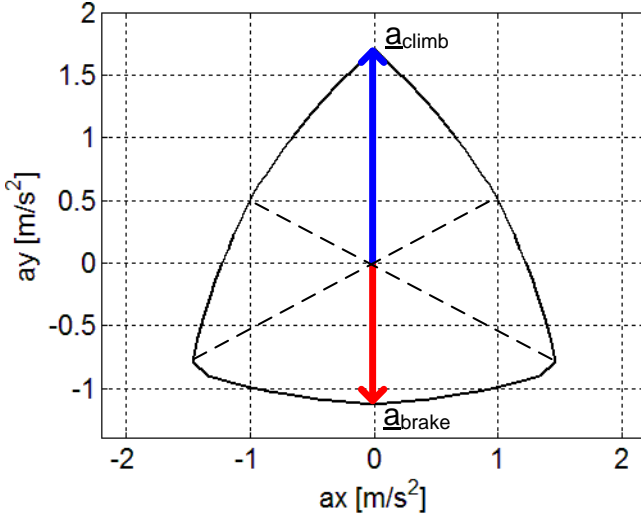


Fig. 21. *x-y section plane of the (wheel slip constrained) acceleration phase space. The minimum acceleration has to be chosen for defining the safety braking distance (worst case principle), while the maximum can be used for calculating the climbing ability.*

As the overall acceleration space of a robot contains all the phenomena (also μ and g) that can affect maximum acceleration significantly, therefore the maximum braking distance for any given linear velocity can be calculated assuming that the robot's angular velocity is zero:

$$l_{brake,max} = \frac{|\underline{v}_{0,Cog}|^2}{2 \cdot a_{brake}} = \frac{|\underline{v}_{0,Cog}|^2}{2 \cdot \min(|\underline{a}_{Cog}|_{\xi=0})}, \quad (56)$$

where \underline{v}_0 is the initial linear velocity vector at the start of braking and a_{brake} is the length of the shortest linear acceleration vector when the angular acceleration is zero.

The maximum climbing ability (slope angle) can also be calculated by the length of the possible maximum linear acceleration vector:

$$\delta_{climb,max} = \arctan\left(\frac{a_{climb}}{g}\right) = \arctan\left(\frac{\max(|\underline{a}_{Cog}|_{\xi=0})}{g}\right) \quad (57),$$

where a_{climb} is the length of the longest linear acceleration vector when the angular acceleration is zero, and g is the length of gravitational acceleration ($\sim 9,81$).

4.9.2 Direction independency and the compactness of the phase space

During my research, experience with different robot geometries showed that the acceleration limits of some robots are more sensitive to direction, while others' are more robust. It is easier to control a more direction-independent robot smoothly. Moreover, if the robot's mechanical limits are near constant, then the control strategy can be simplified without losing the majority of the robot's capabilities. This observation formed the base of further investigation of direction dependency.

The kinematic or dynamic limits of a holonomic robot are absolutely direction-independent if the length of the velocity or acceleration vector is constant, respectively, while the direction of the vector is changing. If the length of the vector deviates according to the changing direction, then the velocity/acceleration limit is the function of the direction. From the above simple principle, it can be stated that if the deviation is somewhat higher then the robot should be more direction-dependent. The question is, how deviation can be measured, what are the existing (e.g. statistical) methods or tools, and which of them can serve as a valid performance measurement on direction independency?

The problem with standard deviance, variance, mean average deviance or other similar statistical calculations is that they are based on a sampled data set and independent of the order of the samples. This can cause contradictory results in practice, because functions with high derivatives can give smaller deviation values compared to a smooth larger curve which is more favorable for robot control. (Taking the first derivative into account provides no benefit in practice, either.)

Visually, the compactness of the 3D phase space reveals a lot about direction dependency: The absolute direction-independent phase space is a sphere, while a highly direction-dependent shape is well distorted and more indented.

At this point of the research, a hypothesis can be formulated about the existence of a method based on a compactness measurement, which reveals to the direction independency of wheeled mobile robots. Also, the mandatory objectives have to be defined from the point of view of unidirectionality in (holonomic) mobile robotics. By taking these considerations into account, the following hypothesis can be formulated in order to characterize the goal of further methodology research.

Hypothesis:

There is calculation method based on a compactness measure, which refers to the kinematic and dynamic unidirectionality (direction independency) of wheeled mobile robots and possess the following attributes:

- It has to be applicable to all type of controllable planar wheeled mobile robots.
- It has to be a generic method, which can be derived the same way as in case of the previously defined robots.
- The result of the calculation in case of the velocity has to express definitely whether the kinematic constraints of the drive system are holonomic or not.
- The result of the calculation in case of velocity and acceleration limits has to express definitely if the corresponding limit is independent of the direction of the corresponding vector.
- The result has to be independent of the scale of the limits.
- The result has to be independent of the orientation of the limits.
(Applicable in case if the limits are direction dependent.)
- The method has to be robust: No special cases are allowed, which can corrupt the method by changing the result significantly against trivial intuitive impressions which are driven by practical aspects.

In the following pages, the common traditional and more special methods are evaluated in order to find a method which meets the criterial characteristics stated in the hypothesis.

There are more than thirty existing theories for geometrical compactness [81], [82], the most relevant methods from the point of view of phase space unidirectionality are the convex hull ratio, the Reock ratio, the Polsby-Popper and the Schwartzberg methods.

4.9.2.1 Convex hull ratio

The principle of convex hull based measurements is shown in Fig. 22. 2D or 3D compactness is defined as the area or volume ratio of the original shape and the convex hull, respectively. It is more likely to indicate the convexity of the phase space, and it can yield the same results (equal to 1) in case of all convex phase spaces, regardless of its unidirectionality. Also note that it cannot be interpreted to non-holonomic kinematics, because it gives a division by zero in case of all non-volumetric phase spaces.

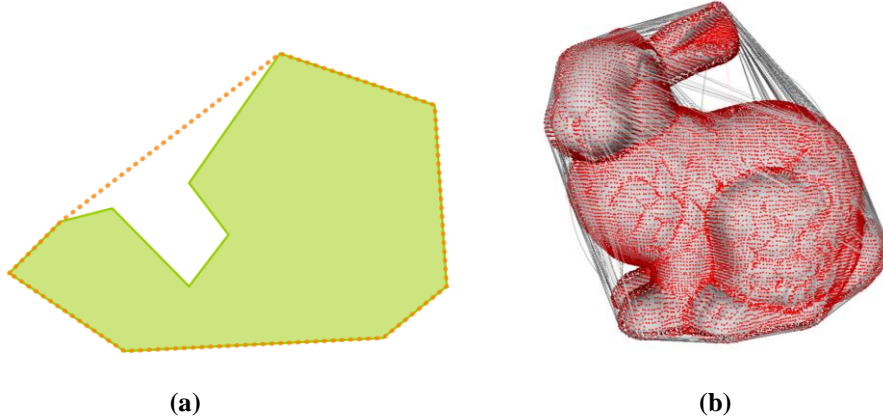


Fig. 22. Compactness measurement of a 2D (a) and a 3D (b) shape by a convex hull. 2D/3D compactness is defined as the area/volume ratio of the original shape and its convex hull, respectively.

4.9.2.2 Reock ratio

The further three compactness measurement methods are more suitable due to their spherical approach based on similarity. Ernest C. Reock [83] uses a bounding circle and a bounding sphere for 2D and 3D compactness definitions, respectively. The Reock score is the surface or volume ratio of the original shape and the bounding circle/sphere, see Fig. 23. This method yields a value of 1 for omnidirectional phase spaces and lower values for all direction-dependent cases, and yields a value of zero in case of all non-holonomic kinematics.

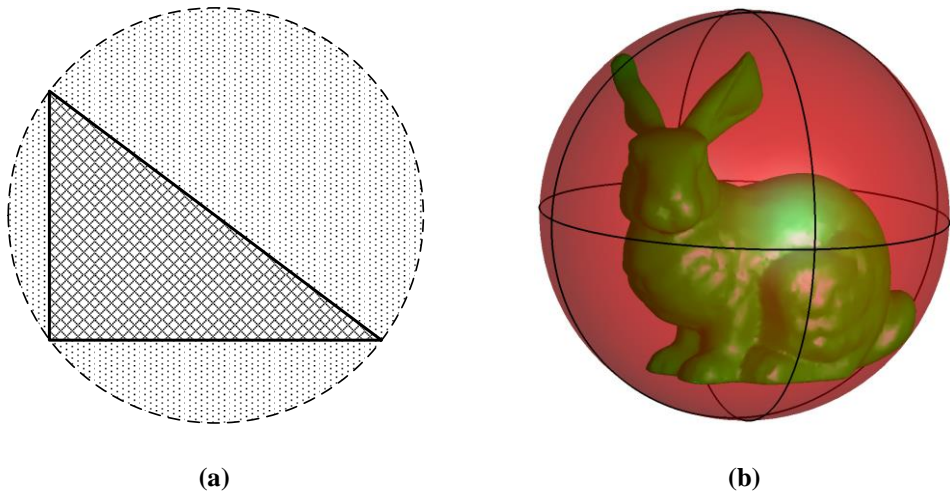


Fig. 23. Principle of the Reock score in 2D (a) and 3D (b). 2D/3D compactness is defined as the ratio of the surface/volume of the original shape and the bounding circle/sphere, respectively.

The characteristics of the Reock score in case of different real phase spaces causes that the ratio decreases with a very high amount when the shape has any narrow extremal protrusion while changes less in case of sharp concave dents. While the narrow extremal protrusion of the phase space can be neglected and left unused, concave internal sharp dents are dangerous weak states of the velocity or acceleration space, where the robot cannot achieve commanded motion. The previously mentioned phase

spaces can occur in case of a very high CoG or other geometries, where the CoG is a few centimeters away from the geometric center on the x-y plane (see Fig. 24).

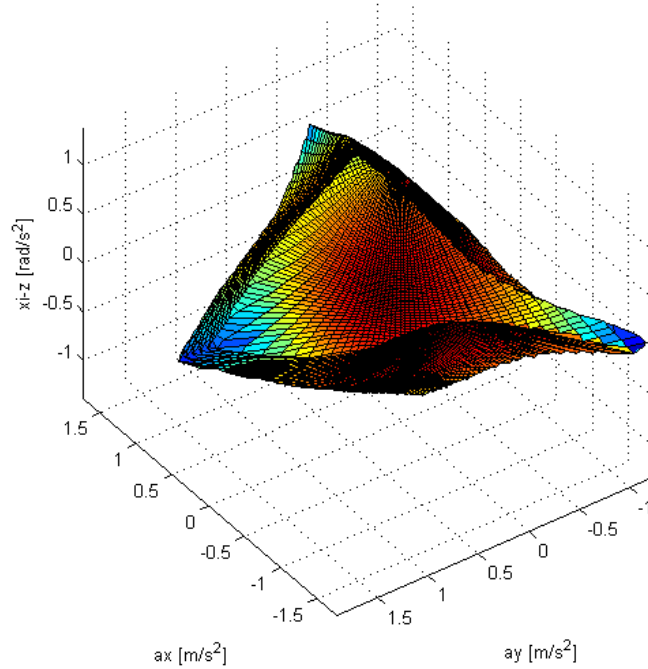


Fig. 24. An example where the Reock score yields a very low value, caused by one narrow extremal protrusion which could be left unused by the robot control. The relatively high protrusion is caused by a 5 cm horizontal offset of the CoG measured from the geometrical center on the x-y plane, where the robot diameter is 60 cm.

4.9.2.3 Polsby-Popper, Schwartzberg, and isoperimetric ratio

The Polsby-Popper and Schwartzberg methods use the isoperimetrical inequality, which is based on the ratio of a circle's perimeter and area in case of a 2D approach. The Polsby-Popper method [84] defines a circle, the circumference of which is equal to the investigated 2D shape, and compares the area of the circle with the area of the original shape:

$$PP = \frac{4\pi A}{p^2} \quad (58),$$

where PP is the Polsby-Popper score, A is the surface Polsby-Popper circle (see Fig. 25/a), and p is the perimeter of the investigated shape (which is equal to the perimeter of the Polsby-Popper circle).

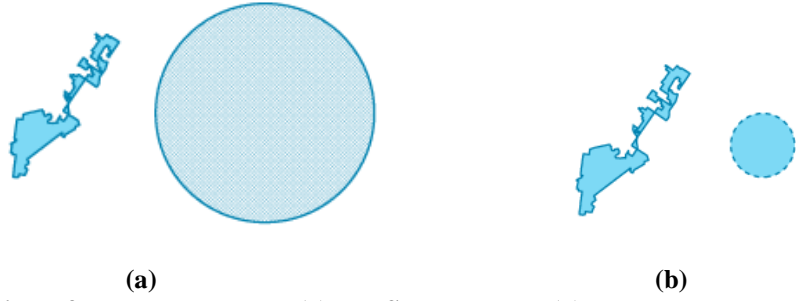


Fig. 25. Principle of the Polsby-Popper (a) and Schwartzberg (b) compactness scores. The first one compares the surfaces in case of equal perimeters, while the second one compares the perimeters in case of equal surfaces.

While Schwartzberg [85] defines a smaller circle, the area of which is equal to the investigated 2D shape, and compares the circumference of the circle with the perimeter of the investigated shape:

$$r_{sch} = \frac{4\pi \sqrt{\frac{A}{\pi}}}{p} \quad (59),$$

where r_{sch} is the Schwartzberg score, p is the perimeter of the Schwartzberg circle and A is the area of the investigated shape (which is equal to the area of the Schwartzberg circle).

The above 2D compactness scores can be interpreted to 3D by using the volume and surface area of a closed 3D shape. The volumetric (3D) isoperimetric ratio, which is equal to the volume of a closed 3D shape divided by its surface area, can be normalized to the isoperimetric ratio of the sphere. This is also called sphericity, and calculated by the following formula:

$$\Psi = \frac{\pi^{\frac{1}{3}} (6V_p)^{\frac{2}{3}}}{A_p} \quad (60),$$

where Ψ is the isoperimetric ratio normalized to the sphere, and V_p and A_p are the volume and surface area of the measured phase space, respectively. The isoperimetric ratio first applied in the field of geology by Hakon Wadell in 1935 [86]. He used the method to measure the roundness of quartz particles.

This method is free from all previously mentioned problems related to the phase space compactness measurement of holonomic mobile robots. Furthermore, it has the following advantageous characteristics, which enables it to provide a comparable performance measure on the direction independency of holonomic mobile robots:

1. Dimensionless number between 0 and 1, where a higher value represents a more direction independent robot.

$$\Psi \in [0 \dots 1] \quad (61)$$

2. The volume is zero in case of surfaces, therefore it yields a value of zero for all non-holonomic kinematics, while
3. It yields 1 for absolute unidirectional (direction-independent) cases.
4. It can be applied to all planar wheeled mobile robots, as they have two or three dimensional phase spaces.
5. It is independent of scale and orientation.
6. It is not overly dependent on some extreme point of the phase space, while these points can hardly be used for trajectory planning.

According to the above characteristics, the following thesis can be stated:

Thesis 2

The unidirectionality of the kinematic and the dynamic capabilities of any planar wheeled mobile robot can be described by a scalar indicator by using the isoperimetric quotient applied to the closed volume of the velocity and to the acceleration phase spaces, respectively.

$$\Psi = \frac{\pi^{\frac{1}{3}} (6V_p)^{\frac{2}{3}}}{A_p} \quad (62),$$

where Ψ is the isoperimetric ratio normalized to the sphere, and V_p and A_p are the volume and surface area of the measured phase space, respectively.

Author publications in connection with the above thesis: [P1-P3, P5, P10-P19]

In practice, the value of the isoperimetric ratio of the (wheel slip based) acceleration phase space of a 3-wheeled kiwi drive platform is between 0.6 and 0.8. The robot can be considered as strongly direction-dependent in the lower portion of the interval, under 0.7. In this case, the maximum deviation of the maximum length of the velocity or acceleration vector is over 50%.

The isoperimetric ratio of common regular objects and the effect of the variable aspect ratios can be found in [87]. The diagrams in this article can assist the simplification of a real phase-space to a regular object, like a cone [34] by visualizing the isoperimetric quotient as the function of the aspect ratio.

4.9.3 Effect of the height of the CoG on unidirectionality

As previously discussed, the distortion of the wheel slip based acceleration space is higher when the height of the CoG is higher (see Fig. 19). Intuitively, the phase space based on a higher CoG seems more direction-dependent, as the shape has sharper protrusions and also some concave areas.

The (theoretically) zero height of the CoG, measured from the ground, causes that the load forces on the wheels are independent of the actual acceleration state. In other words, the weight transfer effect [88] is neglected. This implies the same cubical shape as in case of the velocity space [34] (see Fig. 26/a). As the height of the CoG increases, the original hexahedron becomes more distorted (see Fig. 26/b).

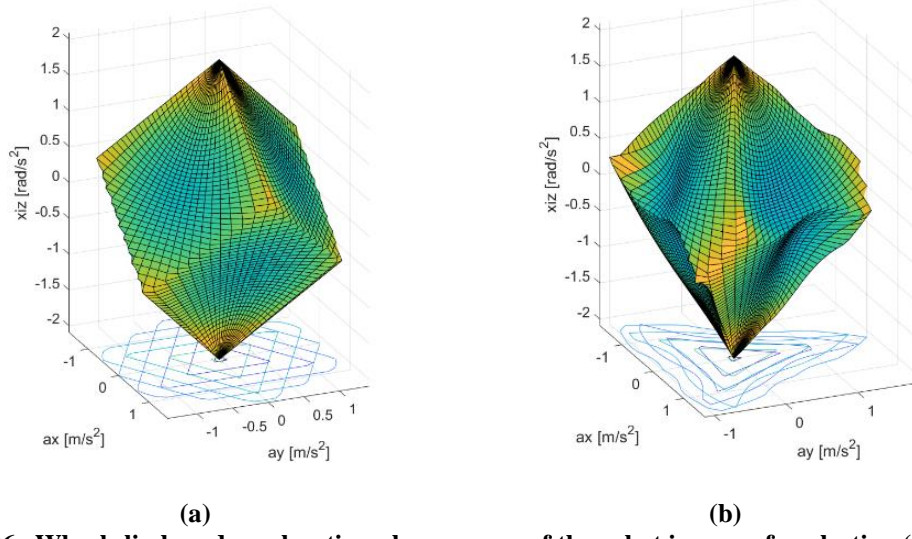


Fig. 26. Wheel slip based acceleration phase spaces of the robot in case of neglecting (a) and considering (b) the effect of the CoG height.

Hypothesis:

From the above facts it can be assumed that the value of the isoperimetric ratio in case of zero CoG height is equal to the isoperimetric ratio of a regular hexahedron if the z directional moment of inertia is adjusted to get edges of equal length. This also means that this value should be the upper limit of the isoperimetric quotient, which cannot be reached in case of a real robot, where the CoG height must be a positive non-zero value. Additionally, it can be supposed that the value of the isoperimetric ratio decreases as the height of the CoG increases.

In order to clarify the above assumptions, the isoperimetric ratio was calculated as the function of CoG height by numerical calculations. The numerical method should use proper resolution for generating the approximate closed 3D shape of the phase space because numerical volume and surface measurements are affected significantly in case of relatively low resolution [81]. Therefore, resolution was tested by trial, being increased until it enabled precise results (low deviation to resolution changes) but remaining not overly calculation demanding. The proper resolution is between 1 and 2.5 degrees in case the phase space is generated in polar space. The higher resolution phase-space and the corresponding generated Alpha shape can be seen in Fig. 27.

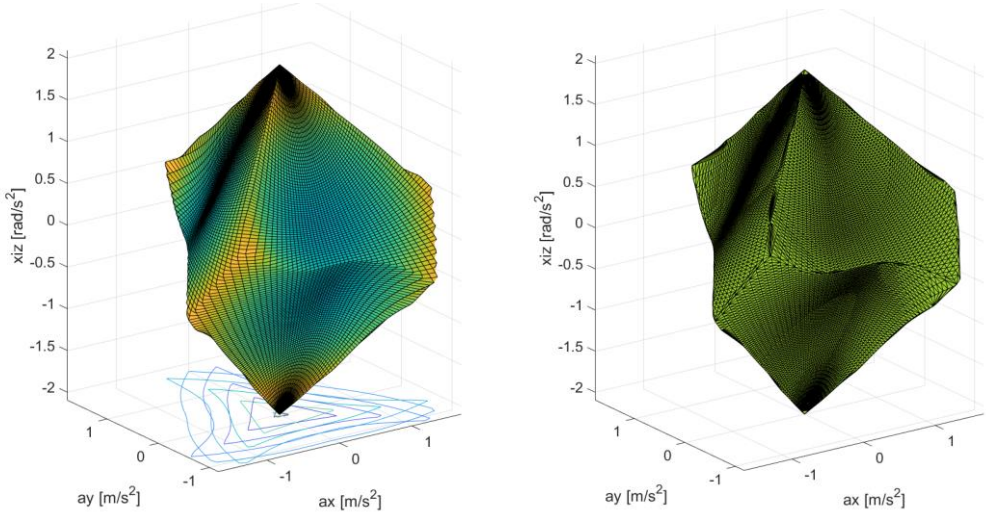


Fig. 27. Higher resolution phase space for volume and surface calculations (a) and the generated Alpha shape

In order to calculate the isoperimetric ratio as the function of the CoG height, the same calculation has to be repeated several times. The height of the CoG has to be quantized: One step is selected as the 1/10 of the radius of the circle coincident with the wheels (r), and the interval is $[0.1r-4.5r]$. Above $4.5r$, the phase space becomes chaotic, and in case of this high CoG, the wheel slip constrained acceleration space is not relevant due to an earlier tip-over situation. The result of the calculation series is shown in Fig. 28.

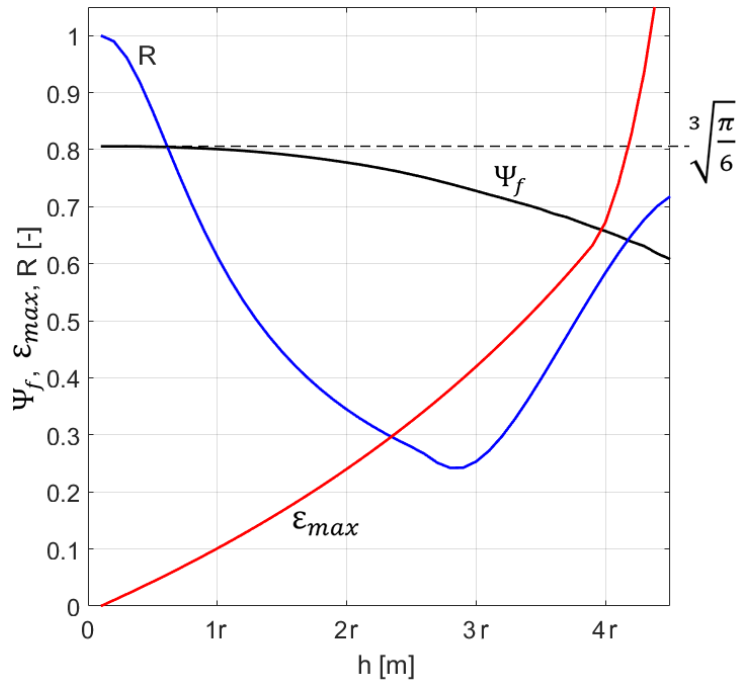


Fig. 28. Unidirectionality as the function of CoG height (Ψ_f), maximum error (ϵ_{max}) and linear correlation (R) of vector length compared to the case of zero CoG height.

The evaluation of the numerical simulation and resulting function diagram proves the previously stated hypothesis, therefore, the following thesis can be stated:

Thesis 3

The unidirectionality of the wheel slip constrained maximum acceleration of a 3-wheeled omnidirectional kiwi drive robot monotonically increases when the height of the center of gravity decreases, but never reaches the sphericity of a regular hexahedron.

$$\lim_{h \rightarrow 0} (\Psi_f(h)) = \lim_{h \rightarrow 0} \left(\frac{\frac{1}{\pi^3} (6V_p(h))^{\frac{2}{3}}}{A_p(h)} \right) = \frac{\frac{1}{\pi^3} (6a^3)^{\frac{2}{3}}}{6a^2} = \sqrt[3]{\frac{\pi}{6}} \approx 0.806 \quad (63)$$

$$\Psi_f(h) < \sqrt[3]{\frac{\pi}{6}}, \quad \{h \in \mathbf{R} \mid h > 0\} \quad (64)$$

where h is the positive non-zero height of the CoG, measured to the ground, Ψ_f is the unidirectionality of wheel slip constrained maximum acceleration, V_p and A_p are respectively the volume and surface area of the wheel slip constrained acceleration phase space, and a is the length of a regular hexahedron (positive, non-zero, scalar value).

Author publications in connection with the above thesis: [P1, P2, P11-P13, P16-P20]

In practice, the maximum relative error (ε_{\max}) is over $\pm 25\%$ when the height of the CoG (h) is higher than the diameter of the circle coincident with the wheels ($2r$) compared to the model which neglects the vertical position of the CoG. In this case ($h > 2r$), it is recommended to use a model which handles the effect of the vertical position of the CoG. Therefore, the wheel slip can be avoided in a way that the inherent characteristics of acceleration capabilities remain utilized by allowing higher accelerations in favorable directions.

According to the above evaluation, the calculated value of unidirectionality assists decisions on a possible simplification or – maybe the absolute negligence – of the direction-dependent model which is used for controlling robot motion.

5 EVALUATION

The proposed calculation of velocity and acceleration limits were first tested and visualized in offline calculations. After the calculations, embedded microcontroller and PC based implementations are described in Subsections 5.3 and 5.4. Finally, the proposed and implemented methods were validated and evaluated.

5.1 Calculation examples and kinematic simulation

In case of the velocity space, the velocity limiter algorithm was tested based on the kinematic model. For the acceleration space, a Matlab application is shared to visualize vector spaces in case of different robot and environmental parameters.

5.1.1 Kinematic simulation – Limits based on velocity space

Fig. 29 shows the linear velocity of the robot (b) and the velocity of each wheel (a) during a linear movement while the robot was rotating continuously.

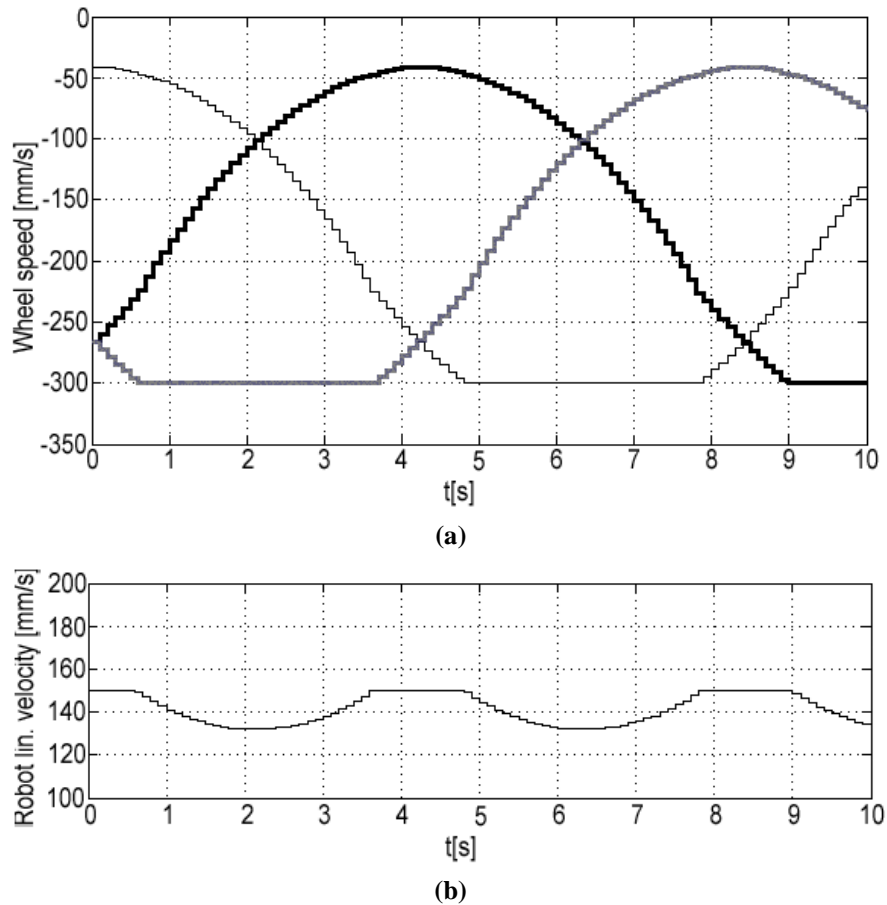


Fig. 29. Peripheral velocity of each wheel, where the three different plots represent wheels 1, 2 and 3 (a) and the limited linear velocity of the robot (b)

During the discrete time simulation, the maximum wheel velocity in the drive direction (v_{drive} in Fig. 11) was 300 mm/s. The reference linear velocity of the robot in the world coordinate system was 150 mm/s, and the reference angular velocity was 0.5 rad/s. As the diagrams show, when any of the wheel speeds saturates, the overall robot velocity gets limited according to the characteristics described in Fig. 12 to avoid path deviation. Notice that the velocity of CoG performs only smooth changes with no discontinuities or higher slopes. This favorable characteristic was utilized later in the robotic implementation section.

5.2 Acceleration space - Application for assisting robot design

A comprehensive Matlab model with user interface was developed in order to evaluate wheel slip, motor torque and tip-over based acceleration spaces. The application can also visualize the intersection of the three different vector sets, presenting the overall acceleration capabilities of a kiwi drive based mobile robot. The unidirectionality (isoperimetric ratio) of the closed phase spaces (wheel slip and tip-over) is calculated by using the Alpha shape of the original plot. The automatically generated Alpha shape can be visualized over the original color plot by setting a checkbox. The Graphical User Interface (GUI) of the application is shown in Fig. 30.

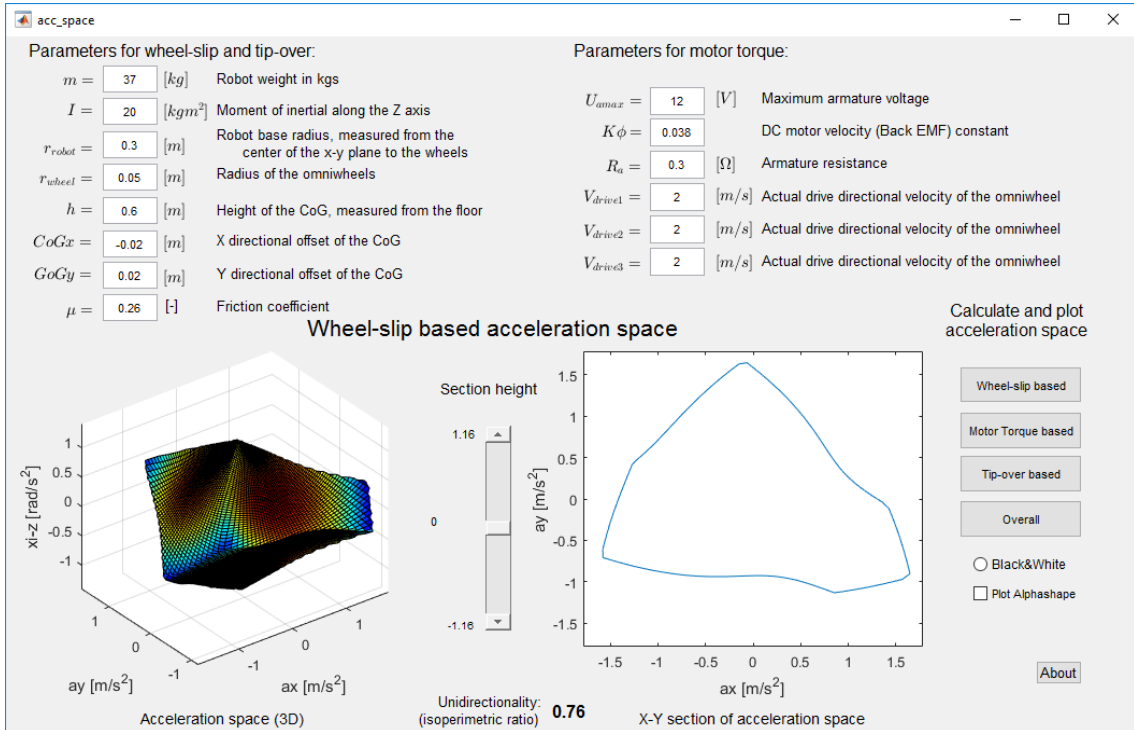


Fig. 30. Graphical user interface of the acceleration space visualizer Matlab application

The proposed simulation software assists the determination of a robot's geometrical and mass properties at the beginning of the mechanical design process. The typical available parameters of the driving electric motors can be given, therefore the

visualized results can assist the right motor selection for the previously defined robot mechanics.

5.3 Robotic implementation based on decentralized hardware architecture

This section gives a general overview of the development of the applied open-source robot control architecture, which enabled the implementation and testing of phase space related theories. The decentralized motion control system was adapted to the experimental holonomic kiwi-drive based robot. The robot named Ethon and its kiwi drive arrangement are shown in Fig. 31. The Ethon robot was the second generation of the mobile robot series [38], [89]–[95] developed for Ethological model based robot behavioral control.

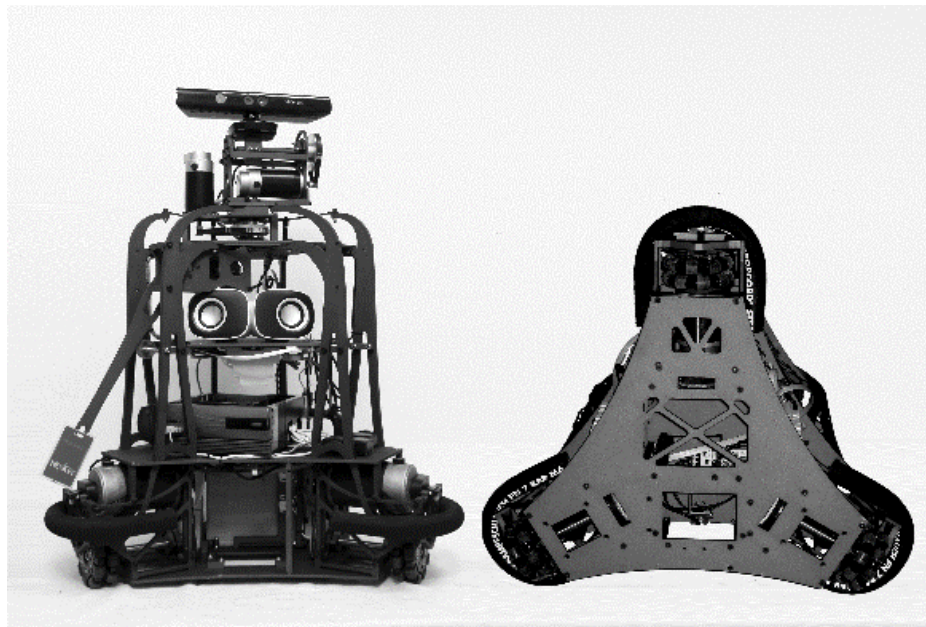


Fig. 31. Experimental robot and its drive system in the bottom view

5.3.1 Applicability Criteria for Compliance with Reliability Requirements

The development and implementation of complex robotic algorithms are straightforward in case of centralized hardware architectures. However, the applicability of these architectures is highly restricted because decentralized solutions have become dominant in the industry and mobile robotics. In most cases, centralist solutions are special devices, which cannot be modified and are hard to repair. The debug process is much more difficult, because the system cannot be tested by each module separately. Furthermore, a possible fault during operation often causes global problems in the whole motion control system, and sometimes it causes the loss of control over the whole robot.

The theories presented in the previous sections are developed in order to comply with widespread decentralist systems, which can contain a PC in case of high computing demand. These criteria ensure applicability and reliability.

The structure and realization of decentralist hardware architectures are highly affecting the operation of control algorithms. E.g. a longer time delay and jitter of communication protocols between the different controllers can easily degrade the control stability. Similarly, the applied torque and acceleration can be corrupted if the position controller of the drive motor does not compensate the available (battery) voltage, which is a changing parameter. The exact knowledge of these kinds of system characteristics is necessary to meet the operation requirements and enable accurate measurements. The relevant principles and some key details of the applied hardware architecture are presented in the following subsections.

5.3.2 General overview of stock hardware architectures for robotic research

In the field of mobile and industrial robotics, testing and measurement procedures require detailed knowledge of the hardware architecture to perform complex development tasks. Most of the professional stock hardware elements on the automation market are closed systems and allow no direct access to low-level servo control or real-time reading of encoder positions. Due to these types of restrictions, the implementation of sophisticated control algorithms is hardly possible using industrial stock systems. Cost-effective open source solutions (e.g. Arduino) lack compatibility and due to their hobby purposes, they have long timings and computing jitters which cause too much unwanted phase shifting for a sophisticated closed loop control. Other special systems developed for research like Matlab dSpace need a huge free space in a mobile robot and the power consumption restricts testing and application possibilities.

Facing these kinds of drawbacks and restrictions in the combination of many different stock architectures led to the development and application of an industrial grade but open source motion control architecture, which strongly accelerated daily work and research activities. The following subsection introduces the open source LinuxCNC and the development of the applied hardware architecture.

Further notable own previous experiences in non-Cartesian centralist and Cartesian decentralist robot control architectures can be found in [96] and [97].

5.3.3 Introduction to robot control with LinuxCNC

LinuxCNC (the former name was Enhanced Machine Controller or EMC) is an open source x86 PC based software for controlling industrial robots and CNC machines up to 9 axes. The project was originally founded more than two decades ago by the US NIST (National Institute of Standards and Technology) in order to provide a vendor-

neutral solution for numerical control [98]. It uses Linux kernel with real-time extensions (RTAI or RTLinux), and can control the linear axes or rotational joints of a robot using RS274-NGC standard (G-code) as operation input. It can handle the operation of all peripheral elements, e.g. sensors or grippers. The GUI of LinuxCNC (see Fig. 32) can be customized for specific kinds of usage e.g. interfacing with custom robots.

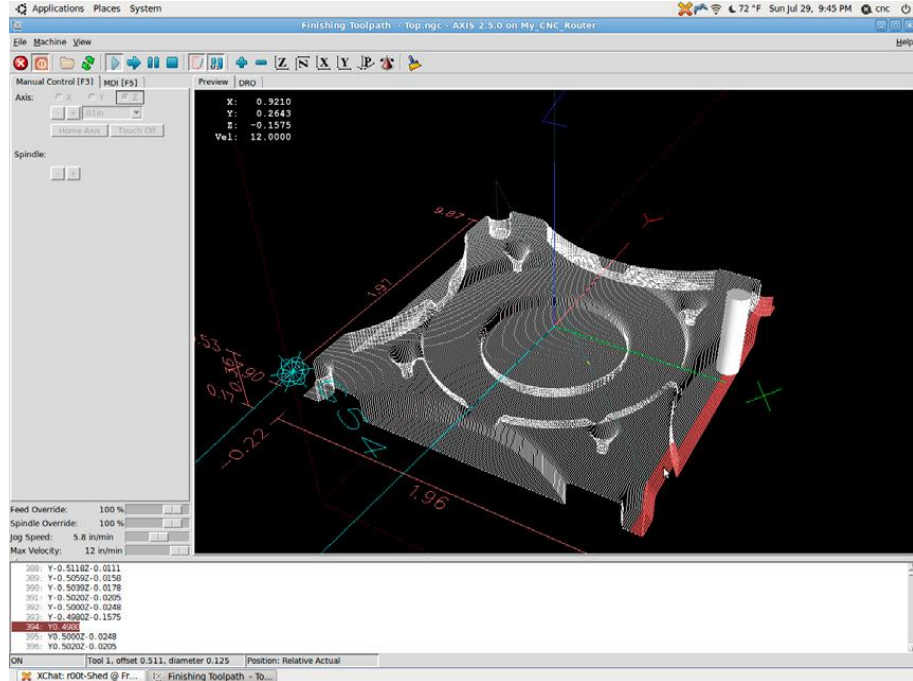


Fig. 32. Default graphical user interface of LinuxCNC for numerical control

As the entirety of the project is open source, it is possible to implement inverse kinematics, hence the software system is capable to control any non-Cartesian as well.

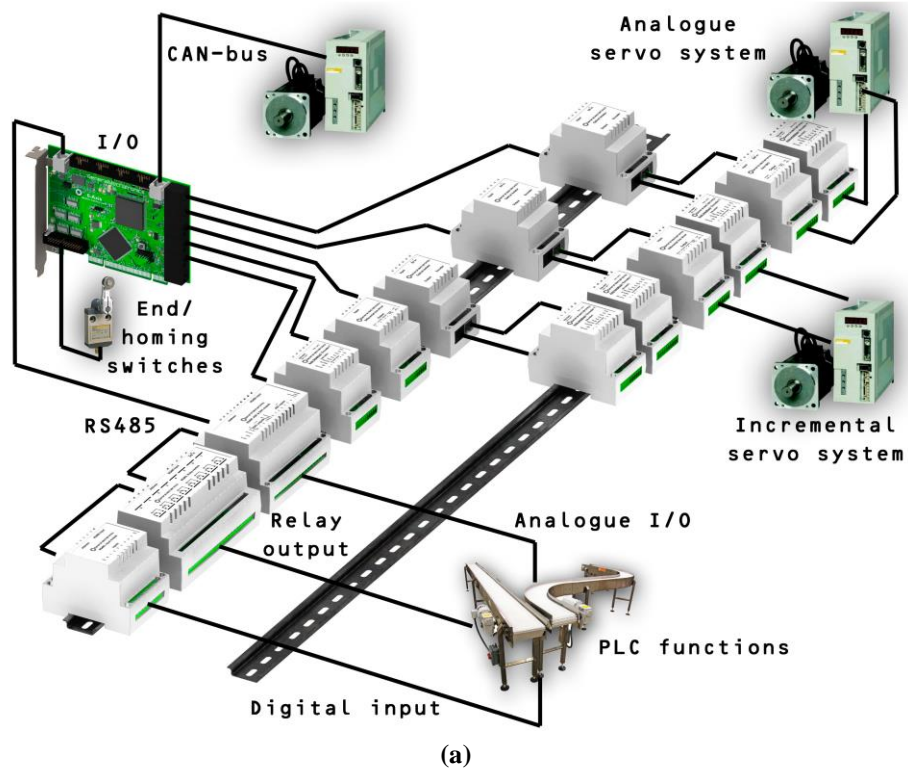
5.3.4 Interfacing with LinuxCNC

LinuxCNC provides a PC software suite from the GUI to low-level system functions, while the connection of servos and their power electronics need to be solved in order to operate a machine or robot. The earlier x86 PCs featured an LPT port which still exists on some motherboards, but the lack of I/Os and the slow data transmission rate restricted its application. Another real-time interface opportunity is the 32-bit PCI-bus, which is still in use in most industrial PCs or Mini-ITX type low-end motherboards which can be operated on a mobile robot. Its 133 MHz bus clock speed enables the implementation of low latency I/O signals eligible for closed loop control. Therefore, the GM6-PCI Motion Control card and its modular signal interface extensions were developed in cooperation with Bence Kovács and Ferenc Tajti [77]–[81]. Due to its early success within the LinuxCNC developer community, General Mechatronics Ltd. was founded in 2012 and a market ready version of the system was released within the same year. Since then, over 30 systems have been ordered by other universities and

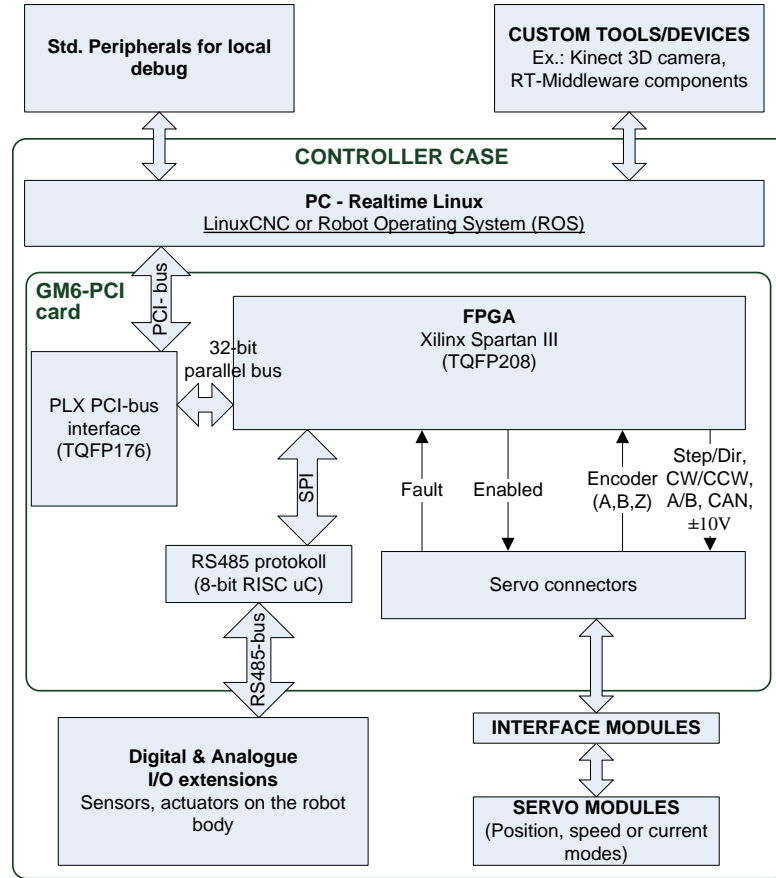
research institutes as well as some industrial customers in the CNC or robotic automation industries.

5.3.4.1 General system layout

The hardware architecture of the system layout is shown in Fig. 33. The PC installed with LinuxCNC is hosting the PCI card, which is the core gateway for all other modular elements including connecting servos, actuators and sensors.



(a)



(b)

Fig. 33. System layout (a) and functional block diagram (b) based on GM6-PCI motion control card

The system consists of different types of interchangeable modules to connect different types of servo controllers and other actuators or sensors. This flexibility enabled a wide application range from CNC machines to mobile robots.

5.3.4.2 PCI bus interface

The backbone of the PCI card is based on a PCI bridge Application Specific Integrated Circuit (ASIC), (PLX Technology, PLX9030) and a Field Programmable Gate Array (FPGA), (Xilinx/Spartan 3E), shown in Fig. 33. The FPGA configuration is stored in a serial dataflash and uploaded every time when the circuit gets power supply and bus clock signals.

The machine side interface consists of 6 axis connectors, CAN and RS485 bus, isolated low-speed and non-isolated high-speed I/Os. The PCB was rooted on a standard size PCI card only on two layers. The elimination of internal layers enabled a short time development caused by accessible outer nets. Cost-effective repairs of the card are also possible because of the low heat transfer of the simple two layer construction. To comply with Electro Magnetic Immunity (EMI) and Electro Magnetic Conductivity (EMC) requirements, the majority of the bottom layer is one consistent ground plane.

Therefore, most of the parts and signal nets must be placed on a single top layer. These boundary conditions required parallel hardware development process with simultaneous schematic and PCB design, in which case the schematic design was strongly driven by routing constraints as well. A significant space was also gained by placing a large TQFP-176 package in an unconventional diagonal way, see Fig. 34.

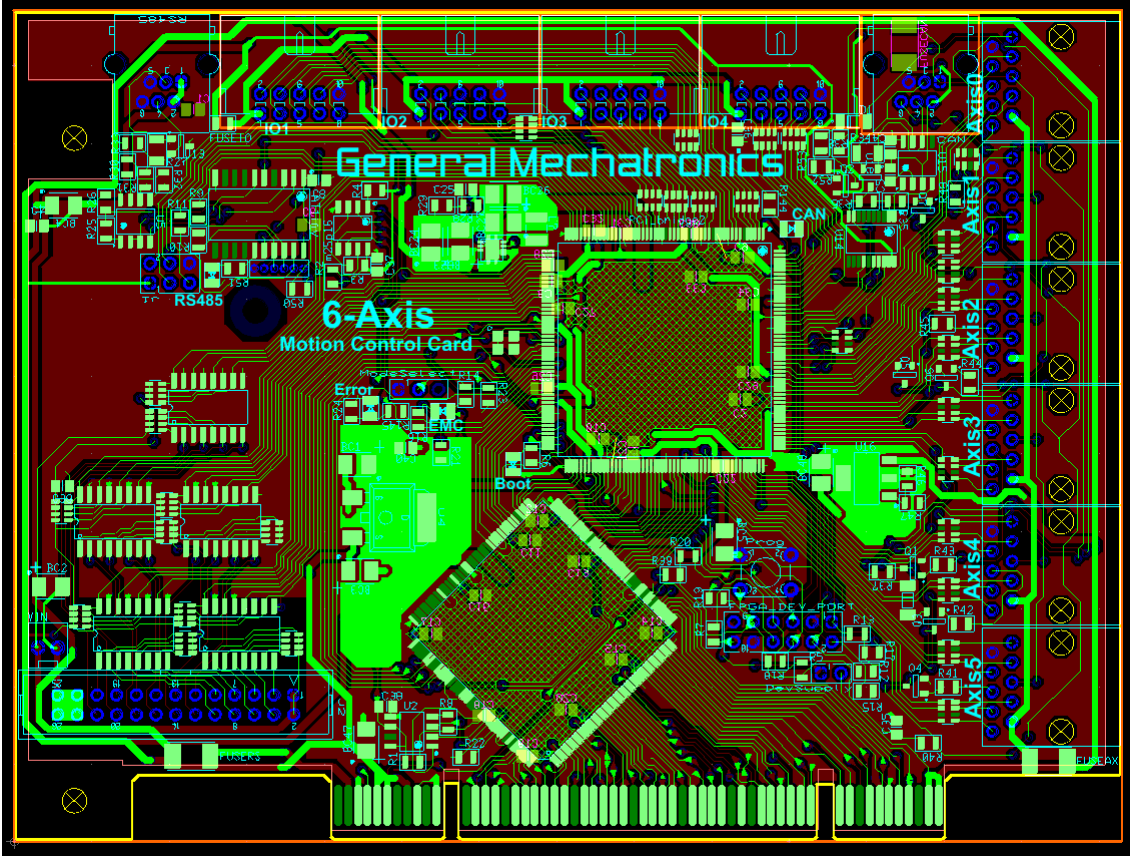
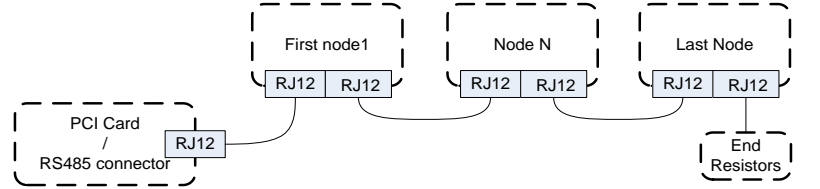


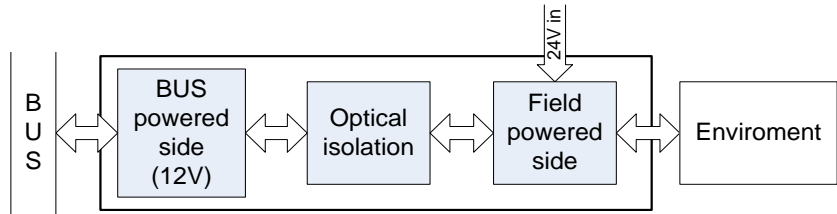
Fig. 34. PCI interface rooted on two layers with the diagonal placement of PCI bridge ASIC

5.3.4.3 Field or chassis bus

A simple 9-bit RS485 protocol was developed to extend the general purpose digital and analogue signals along the robot body. The bus is managed by a separate 8-bit RISC microcontroller on the PCI card, which communicates with the FPGA via SPI. The protocol includes enumeration and fault handling in case of a node error. Therefore different types of local interface modules can be connected in a serial chain (see Fig. 35/a) according to the actual robot's actuator and sensor locations. Each module has a unique, four bit long address on the bus, hence up to 16 modules can be chained to one PCI card.



(a)



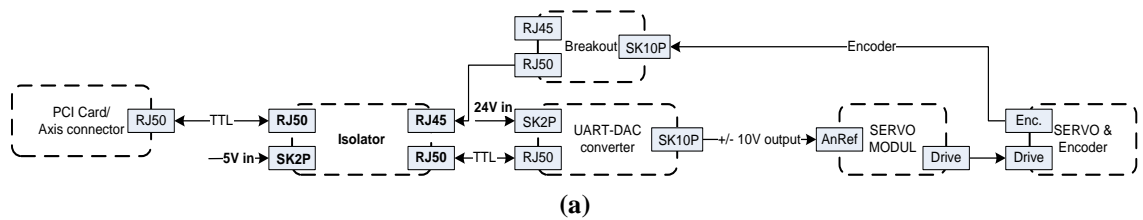
(b)

Fig. 35. RS485 extension bus (a) and general module isolation concept

Basically, the modules have a bus powered and an application powered side with an optical isolation separating them, see Fig. 35/b. This ensures safe operation and overvoltage protection for the low voltage control electronics. During startup the driver exports the pins and parameters of all available modules. These pins are configured (connected) to a function in the hardware abstraction layer (HAL) configuration of LinuxCNC.

5.3.4.4 Servo interfaces

The wide range servo compatibility of the system was a key requirement during specification to ensure the possibility of comparison measurements with different types of servos. This is ensured by a modular concept, where different types of interface modules can be connected in multiple combinations to provide several options with less different hardware elements. Consequently, a single hardware element performs one basic signal function, like optical isolation, differential line conversion or digital-to-analogue (DAC) conversion. This setup results in nine possible different useful interfaces with the necessity of only four different hardware elements. Fig. 36 shows the connection block diagram of two different examples, a classic analogue system (a) and an incremental differential system with encoder feedback (b).



(a)

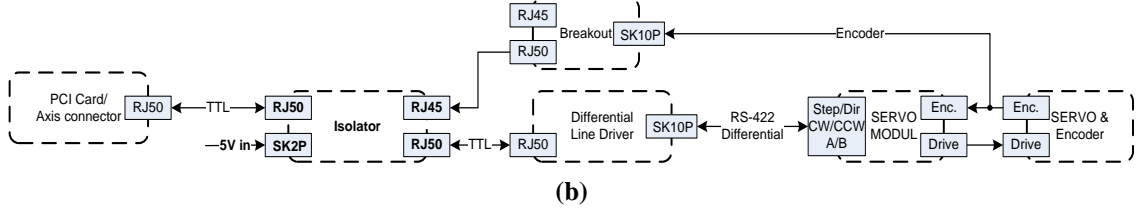


Fig. 36. Examples of (a) analogue and (b) differential incremental servo interfaces

5.3.5 Servo amplifiers

Servo amplifiers are key elements in any motion control system, as they are always part of the high-speed closed loop control. Small unwanted dead times in power electronics or in feedback signal processing can affect the current and motion control significantly. Industrial grade stock servo packs contain many unknown and undocumented filters, additional feedforward and adaptive solutions. Therefore, using them as a black box highly restricts accurate and comparable measurements. In order to keep the closed loop control system transparent, self-developed brushed DC servo controllers were used on robots for driving the wheels and other on-board actuators. The installed servo amplifiers can be seen on a holonomic mobile robot in Fig. 37.



Fig. 37. Brushed DC servo amplifiers installed on mobile robot

5.3.5.1 Hardware description

The block diagram of the servo controller is shown in Fig. 38.

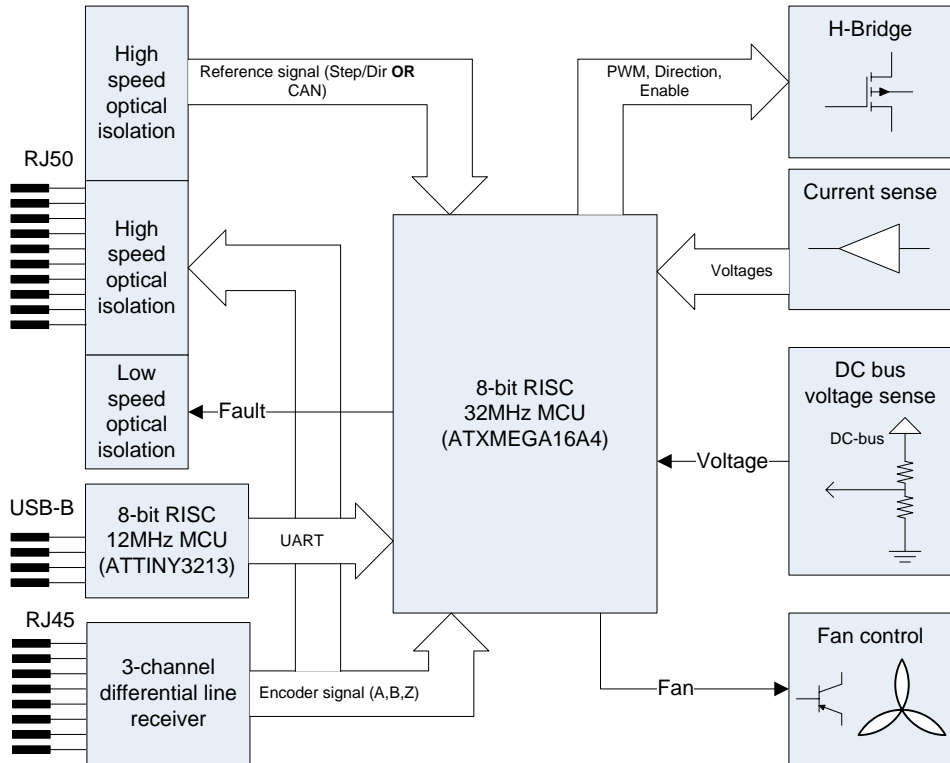
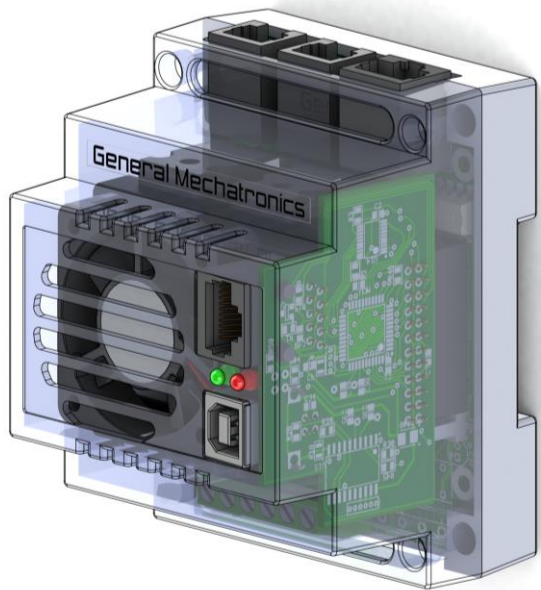


Fig. 38. Block diagram of the brushed DC servo controller

All the signals to and from the PCI card are optically isolated. The reference signal can be CAN messages or conventional Step/Dir signals. The encoder signals are first handled by a differential receiver, which can host absolute signals referenced to ground due to a resistor network before the differential inputs of the receiver. After the line receiver, the encoder signals are connected to the microcontroller and fed back to the PCI card for diagnostics and to allow centralized control. Finally, one additional fault line is connected to the reference connector to indicate any fault conditions. The H-bridge is built up from discrete elements to maintain the flexibility of adjusting switching and dead times. For current sensing, a hall-effect current sensor ASIC and an operation amplifier for each half-bridge were used. For sensing the DC bus voltage, a simple resistor divider was used with a low-pass RC-filter. For active coolant, a small brushless DC fan was added, which can be adjusted according to thermal load. The 3D model and photos of the realized servo controller module can be seen on Fig. 39.



(a)



(b)



(c)

Fig. 39. DC servo amplifier
3D model (a), electronics (b), enclosure (c)

5.3.5.2 Functional operation, cycle times and control strategy

The firmware of the servo controller is organized in (real-time) timer interrupts. The sampling time of current sensing and current control can be adjusted with the PWM frequency. The motion control (velocity and position loop) frequency can be set from 500 Hz up to 3 kHz. However, 1 kHz default timing is necessary if the controller is used via CAN-bus position reference. The robot current is sampled two times in each PWM cycle and the timing of the sampling is adjusted continuously to avoid measurement during half-bridge switching transients. (During switching between low-side and high-side power-FETs, the overshoots and small gate-ringing effects can significantly corrupt analogue current sensing.)

Sign-magnitude driving schema was applied to the H-bridge, while the motor current is controlled by a PI loop, where a current limit avoids overloads. A higher threshold-level overcurrent sensing shuts down overall gate drivers in case of a possible shoot-through type short circuit along low-side and high-side FETs.

Driving direction change is continuous, which means that the left and right side half-bridges are driven in 50-50% PWM duty ratio when the motor voltage is not driven. An unbalance between the two half-bridge duty ratios causes an effective duty ratio on the motor windings. The most important advantage of continuous driving direction change is the eliminated dead time of the drive direction change caused by the switching operation mode change of FET drivers. The practical benefit is 20-30% stiffer position control (possible higher proportional term) caused by this costless dead time elimination.

Position control can be (digital) P, PD or PID, with optional position feedforward. The DC-bus voltage level can vary by 10 to 40% according to transient loads and actual battery charge. This voltage level deviation affects position control by its second power, if the load is assumed as a resistive load. Therefore, an important performance improvement was achieved by compensating the P-term according the continuously measured DC-bus voltage level. Without this compensation, a mobile robot servo control can easily start oscillating by the same P(I)D parameters when the battery is fully charged, and then will totally lose its stiffness under lower battery conditions.

5.3.5.3 Parameter settings and tuning

A Windows based PC application was implemented in Delphi 7 for parameter settings and tuning of the servo-controller. An isolated low-speed USB interface was used between the PC and the controller. PWM frequency, cycle times, current limits, maximum duty ratio, reference and feedback signal options need to be set first. Then a control strategy and its parameters need to be entered. The performance of the control can be checked by step, ramp, and triangle form test reference signals, after a successful dataset upload. A screenshot of the tuning software with a step response test signal is shown in Fig. 40.

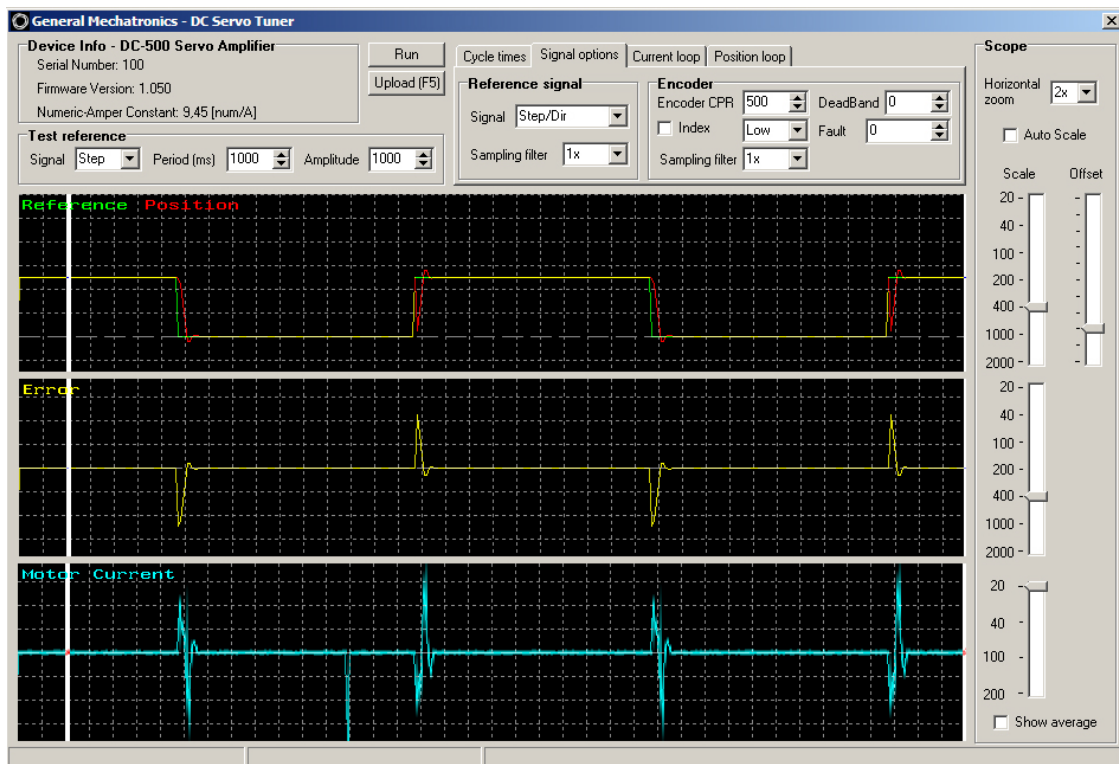


Fig. 40. Screenshot of the software during configuration and servo tuning

5.4 Application of velocity and acceleration space theories

This section provides a reference design to the application of velocity and acceleration space theories complying with commonly used decentralist mobile robot control architectures [95]. The implementation enables the validation of the dynamic model, especially the case of *Assumption II* in Section 4.4, which handles the robot dynamics as one rigid body.

The functional block diagram of the robot hardware is shown in Fig. 41. The global control architecture of most mobile robots is decentralized due to diagnostic and operational feasibility reasons. Accordingly, the motors are driven by independent servo controller modules described in the previous section, and they receive command references from a separated trajectory controller, as in the case of robust industrial applications. Each servo controller can stop the whole robot by indicating fault condition in case of overcurrent, high position error, encoder fault or communication error. In this application, a PD type algorithm is configured to control servo motors.

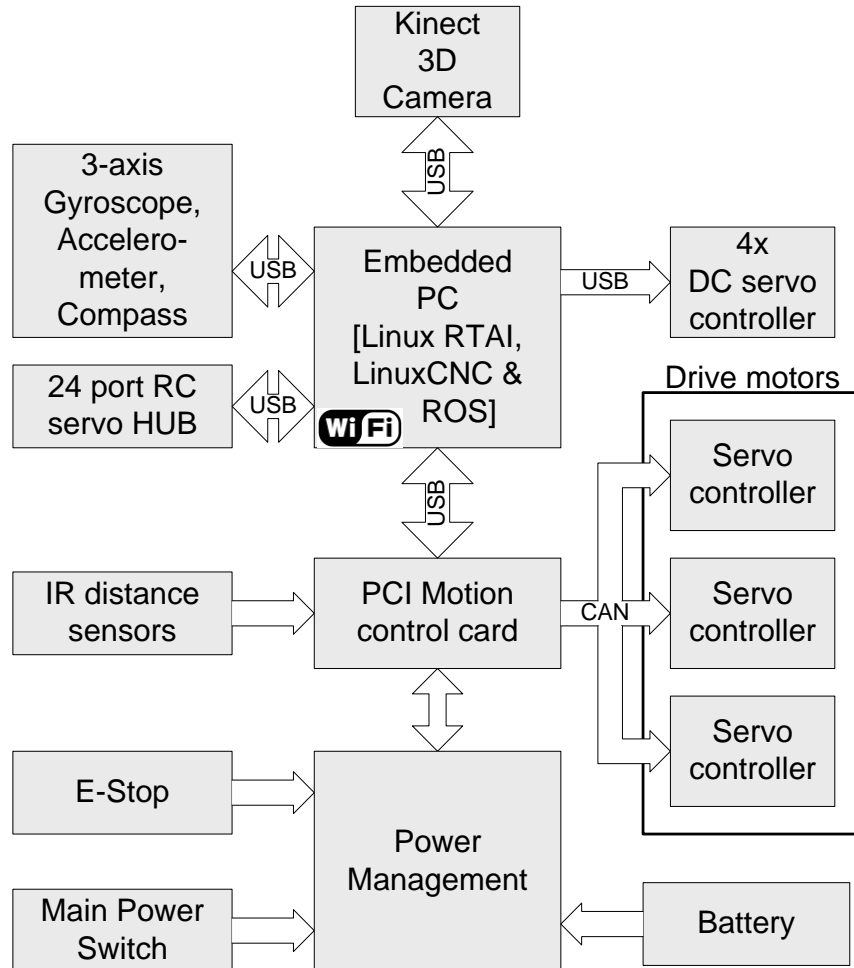


Fig. 41. Functional block diagram of the decentralist robot control architecture

On the PC, the LinuxCNC core performs the interpolation and generates the position reference for the servo controllers. On the other hand, the high-level robot control logic was implemented in ROS framework and provides goal positions for LinuxCNC via TCP local host interface.

ROS runs an SLAM (Simultaneous Localization and Mapping) algorithm using depth information obtained from a Kinect device for global self-localization. It performs sensor fusion using acceleration, gyroscope and magnetic sensor information for improving odometry [38]. The robot is equipped with multiple infrared and ultrasonic distance sensors for obstacle avoidance and safety. More peripherals are connected to the embedded PC in order to control additional actuators on the robot and to interface with sensors and the camera.

The proposed theories were implemented on a microcontroller platform and also on PC as an open source ROS package in order to enable reusability and portability in case of other kiwi drive based robots.

5.4.1 Embedded implementation example of dynamic acceleration and velocity controls

In this arrangement (see Fig. 42), the PC operates the trajectory planner algorithm and provides the requested velocity references (v_{req}) in the robot coordinate system with the corresponding timestamps. A simple microcontroller based motion control and I/O card continuously adjusts the length of the velocity vector according to the mechanical capabilities of the robot, and it feeds back the actual velocity and acceleration reserve information to the trajectory planner. The circuit also provides real-time position reference in 1 kHz sample rate for the wheels by calculating the inverse kinematics described in Section 4.1.

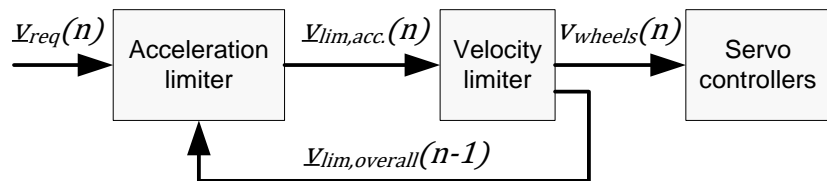


Fig. 42. Functional block diagram of limiter functions

The requested acceleration state can be derived from the requested new velocity reference by using the robot's actual velocity. The overall motion state is processed through the acceleration and velocity limiter functions; their operation is shown in Fig. 43. The orientations of the requested velocity and acceleration vectors are fixed, and only the vector lengths can be multiplied by the calculated velocity and acceleration reserve multipliers, respectively.

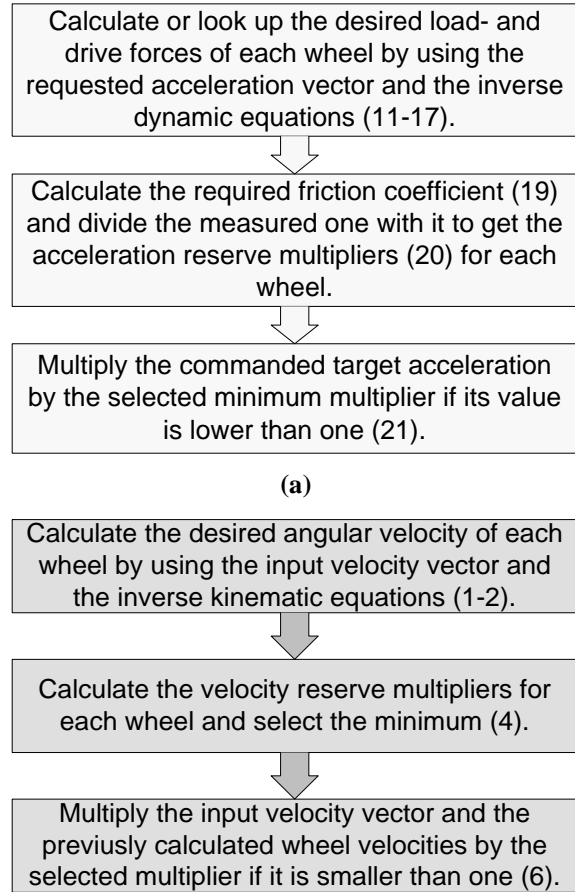


Fig. 43. Structure of acceleration (a) and velocity limiter algorithms (b)

The acceleration limiter algorithm can also increase acceleration using the reserve multiplier in case its value is higher than one. This operation is relevant in case of emergency braking, when the robot should stop with the possible maximum acceleration (deceleration), overriding the original smooth motion profile commanded by the trajectory planner.

Theoretically, a possible fault – incontinuous motion – can occur if the velocity limiter reduces the speed significantly, exceeding the maximum acceleration value. But in practice, the saturation of wheel velocities causes only very smooth changes in the velocity profile, as shown in Fig. 29 (b). The velocity deviation caused by the velocity limiter during a control cycle is in a lower order of magnitude compared to the allowed maximum acceleration. Therefore, the acceleration limit does not need to be reconsidered after velocity limitation.

5.4.2 Reusable open source ROS C++ catkin package

The velocity and acceleration limiter algorithms were also implemented in C++. The source is compliant with catkin, the official build system of ROS. This compliance enables reusability in other kiwi drive based applications. In this arrangement, the PC

runs ROS and the presented ROS catkin package calculates velocity references for each wheel, considering the robot's real capabilities.

In general, ROS consists of many different packages which provide different types of services like camera vision or trajectory planning [71]. From the computation point of view, the calculations are performed in *nodes* and the communication between the nodes is handled by *topics*. A topic can contain several messages and a node can publish or subscribe to a particular topic and its messages. Conventionally, the velocity command in the robot coordinate system is published in the *Twist* message, which contains two three-dimensional vectors: linear and angular velocity. The presented *kiwi_controller* catkin package uses this general Twist message as velocity input and adjusts the length of the given velocity vectors considering kinematics and dynamics. The package controls the driving motors according to the robot's capabilities.

The operation is similar to the microcontroller embedded implementation (Fig. 43). During the migration into C++, the arithmetic was changed from fixed to floating point, in order to make it transparent and to assist portability to different projects. Publishing this new package, ROS developers have the availability to control a kiwi platform considering kinematics and also dynamics related to intense wheel slip.

5.5 Evaluation of the results

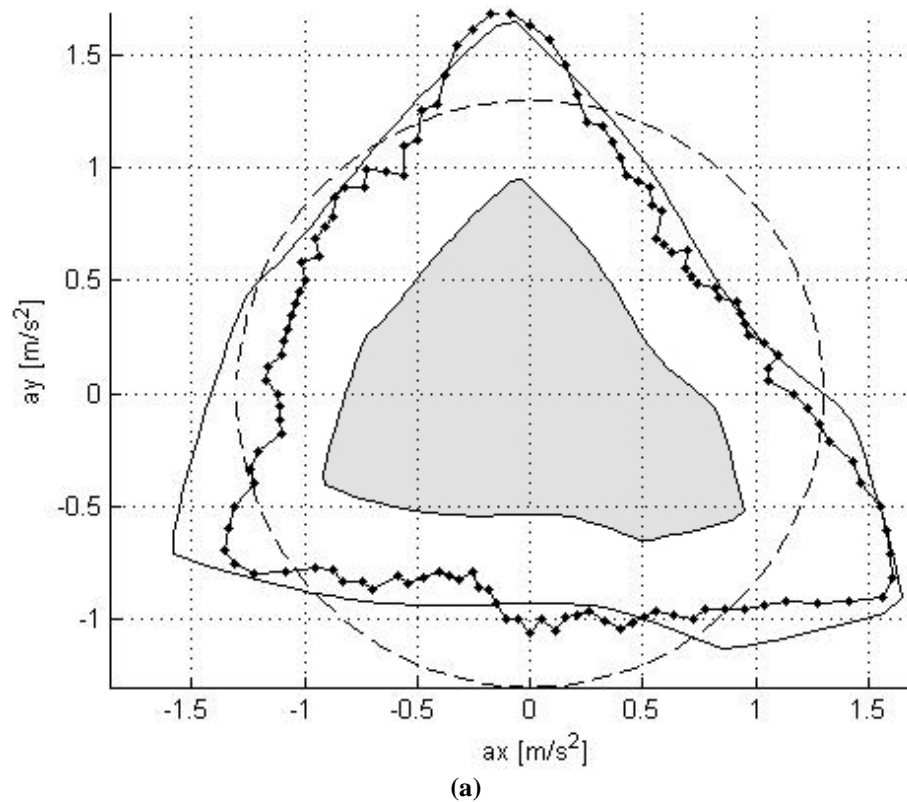
Firstly, the non-trivial wheel slip based acceleration space was validated by predefined acceleration tests considering wheel slip, as the boundary of slip has to be properly correlated to the maximum accelerations given by the acceleration space. Then the validated model was compared to a common trivial assumption. After discussing the comparison, the model sensitivity to the CoG was indicated. Finally, the application of a safety reserve was proposed for a feasible implementation.

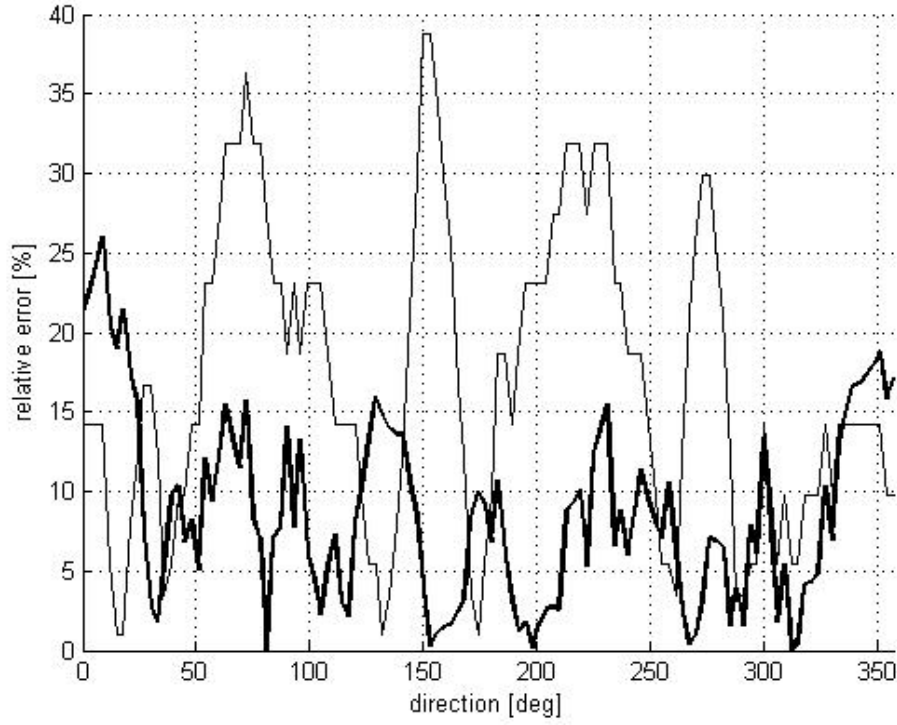
5.5.1 Wheel slip tests to validate the dynamic model

A sufficient number of acceleration tests were performed to measure the acceleration threshold of wheel slip depending on the direction of the acceleration vector.

The tests were triggered by a position reference command. The robot was controlled by a linear trajectory planner, constrained by an asymmetrical trapezoidal velocity profile. A trial acceleration value was given for the acceleration phase and half of that value was used for the deceleration phase to avoid wheel slip during stopping. If considerable wheel slip occurred during the acceleration phase (because the acceleration threshold was exceeded), the robot's reached goal position was different compared to the commanded reference position. Each test case with the same parameters was performed 3 to 5 times near the threshold of wheel slip to refine the end result.

The measurements were taken in two arbitrary planes of the acceleration space in all directions with a 3-degree resolution: one plane corresponds to zero angular acceleration (and velocity) and another plane corresponds to non-zero angular acceleration (0.4 rad/s^2). In case of the second plane, it was more difficult to recognize the occurrence of a wheel slip because the orientation of the robot also changed in case of good traction. This explains the higher average of standard deviations (24%) of the measurement series compared to the first plane where the average value was only 11%. The evaluated measurement results are shown in Fig. 44 and Fig. 45.





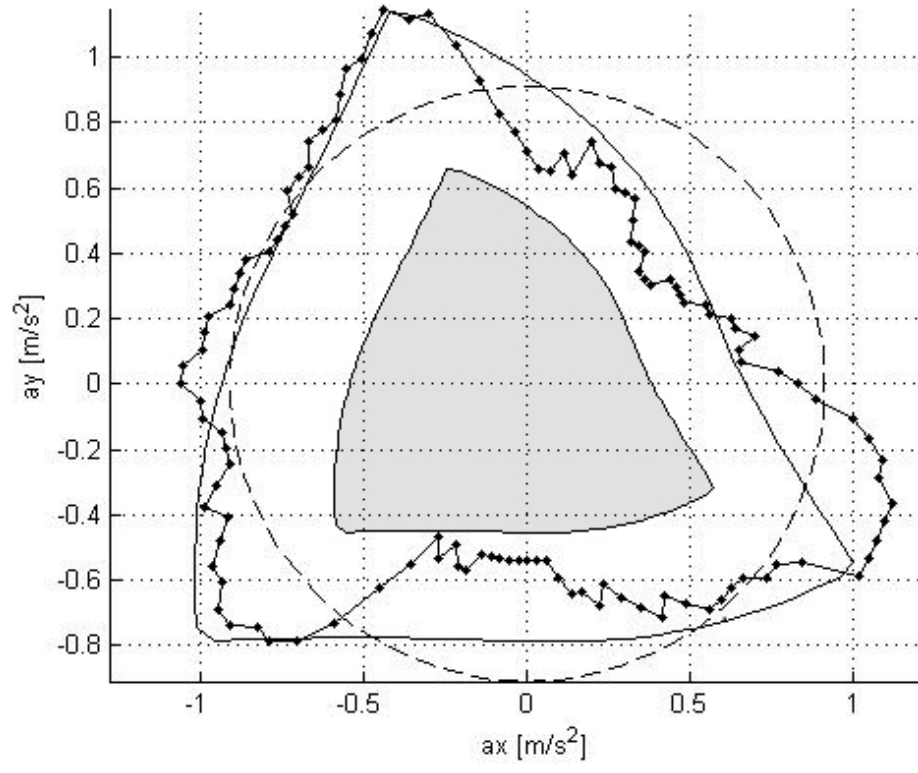
(b)

Fig. 44. (a) Slip test results of the acceleration space at zero angular acceleration, where the dotted line is measurement data, the continuous line is the calculated dynamic model, the dashed line is direction-independent abstraction and the gray area is the safe area of the acceleration vector.
 (b) The absolute value of relative errors, where the thin line is direction-independent abstraction and the thick line is the simulated dynamic model.

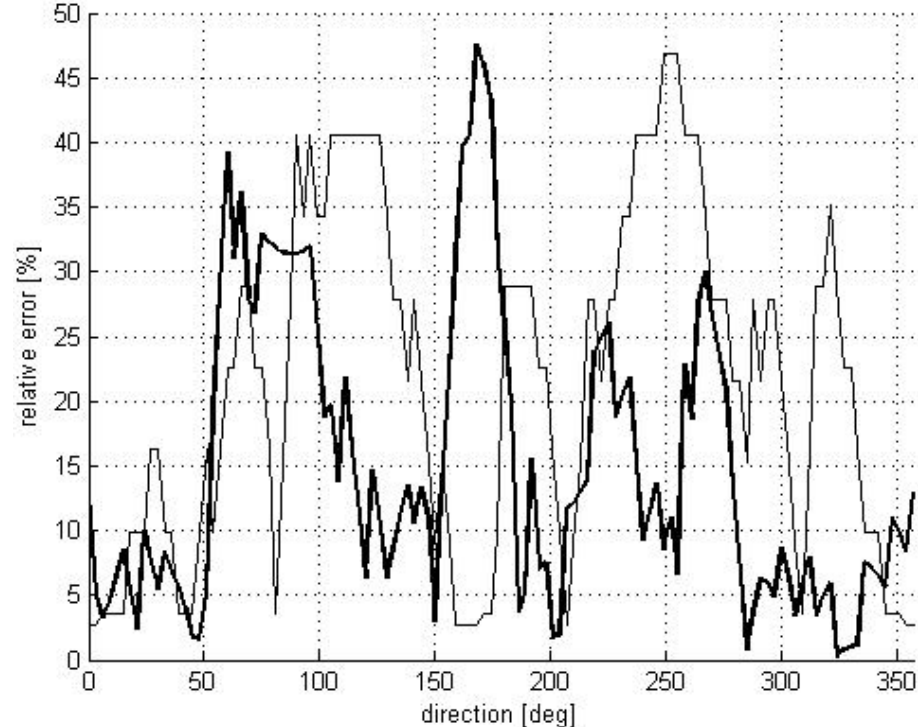
TABLE I

ERROR PROPAGATION BETWEEN THE WHEEL SLIP LIMITED
 ACCELERATION SPACE AND THE MEASURED DATA FOR 0 [RAD/S²]
 ANGULAR ACCELERATION

	Direction-independent model	W.-slip limited acceleration space	Unit
Mean average deviation (MAD)	0.2211 17	0.1146 8.75	[m/s ²] [%]
Linear correlation coeff.	n.a. (-5x10 ⁻¹⁵)	0.8947	[-]



(a)



(b)

Fig. 45. (a) Slip test results of the acceleration space at 0.4 rad/s^2 angular acceleration, where the dotted line is measurement data, the continuous line is the calculated dynamic model, the dashed line is direction-independent abstraction and the gray area is the safe area of the acceleration vector.

(b) The absolute value of relative errors, where the thin line is direction-independent abstraction and the thick line is the simulated dynamic model.

TABLE II
 ERROR PROPAGATION BETWEEN THE WHEEL SLIP LIMITED
 ACCELERATION SPACE MODEL AND THE MEASURED DATA FOR 8.7
 [RAD/S²] ANGULAR ACCELERATION

	Direction-independent model	W.-slip limited acceleration space	Unit
Mean average deviation (MAD)	0.1947	0.1259	[m/s ²]
Linear correlation coeff.	21.4	15	[%]
	n.a. (-8x10 ⁻¹⁵)	0.7365	[-]

5.5.2 Evaluation of model efficiency

A common direction independent abstraction was taken into account to measure the efficiency of the wheel slip limited acceleration space: The acceleration space was approximated by a simple conical shape, therefore the acceleration limit is a scalar and direction-independent constant, bounded only to angular velocity as most of the recent implementations. The curves of direction-independent approximation are plotted by dashed lines in Fig. 44 (a) and Fig. 45 (a). The relative errors are shown in Fig. 44 (b) and Fig. 45 (b), comparing the direction-independent abstraction and the wheel slip limited acceleration space to the measured limits. Tables I and II show the propagation of errors. The proposed model and the direction-independent abstraction were compared to the measurement results by using mean average deviance (MAD) and a linear correlation coefficient. There is a strong linear correlation between the proposed model and the measured results, while the MAD values are more capable of representing the practical, matter-of-fact benefit of the usage of the proposed model.

5.5.3 Model sensitivity to the position of the CoG

The dynamic model had to be extended according to the investigated robot because the robot's CoG was not in the geometric center: The x and y directional position offsets were both around 20 mm, due to the asymmetric placement of the battery and the robotic arm. A relevant experience is that the model is significantly sensitive to relatively small position offsets, especially in cases of considerable angular acceleration.

In case dynamic equations are pre-calculated offline (a lookup table is used to store acceleration space), the position of the CoG cannot be changed in run time. If

there is a considerable moving mass (e.g. a manipulator) on the robot, the results of the dynamic equations should be recalculated online, depending on the actual position of the CoG, and the dynamic reaction force of the moving mass should be added to equations (28, 29).

The reference model parameters of the robot were the following:

Position offset of the CoG:

$$offset_x = -0.02 \text{ [m]}, \quad offset_y = 0.02 \text{ [m]} \quad (65)$$

Friction coefficient:

$$\mu_x = 0.26 \quad (66)$$

Robot weight, moment of inertia along axis z and gravity:

$$m = 37 \text{ [kg]}, \quad I_z = 20 \text{ [kgm}^2\text{]}, \quad g = 9.81 \text{ [\frac{m}{s}^2]} \quad (67)$$

Robot radius and height of the CoG:

$$r = 0.3 \text{ [m]}, \quad h = 0.35 \text{ [m]} \quad (68)$$

5.5.4 Defining the safe area by applying a safety reserve

As equation (39) shows, there is a linear connection between the acceleration reserve multiplier and the available friction coefficient. A safety reserve should be applied to avoid wheel slip in real conditions when the friction coefficient is slightly changing. This can be carried out by choosing a lower available friction coefficient than what was measured. The gray area shows the safe area of the acceleration vector in Fig. 44 and Fig. 45, where the safe friction coefficient is 58% of the one originally measured as the boundary of the safe area.

6 CONCLUSION

6.1 Significantly improved wheel slip based acceleration space

The difference can be twofold between two acceleration limits constrained by different orientations, see Fig. 18 (c) and Fig. 44 (a). This is a significant difference compared to previous assumptions [16], [21]–[25], [33]–[36], [39], [41]–[57]: they assume equal wheel load distribution and therefore, neglect the twofold difference.

This means that it is not possible to implement efficient motion control for omnidirectional mobile robots without considering the changing load force distribution. This is especially relevant if the robot contains a manipulator which applies reaction forces to the robot during motion and interacts with its environment [53], [56], [57], [104], [105], because the wheel load distribution is extremely inhomogeneous. The same situation occurs in case of walk-assist robots [106]. The omnidirectional-type cane robot [48], [107] can push or pull with 2 to 4 times higher force without wheel slip in a given direction if the kiwi drive platform dynamically changes its orientation within ± 30 degrees to reach a more stable orientation against the acting force (see Fig. 18). A very special use case can be found in [108] and [109], where the omnidirectional climbing robot moves on non-planar and/or non-horizontal surfaces. 3D dynamic modelling – considering the real position of the CoG – is necessary here.

The defined velocity and acceleration reserve multipliers provide representative index numbers showing the amount of utilized resources. Using these definitions, the implementation of limiter algorithms is greatly simplified compared to the IRV method [41] or to the linear transformation [34].

6.2 Reusable open source implementation

A reusable open source ROS C++ catkin package is available under the link in the appendix: Developers have the off-the-shelf solution to control a kiwi platform considering kinematics and also dynamics related to intense wheel slip. The algorithm can be parametrized by simple measurements, without the necessity of any special equipment.

By using the proposed dynamic model, a Matlab application user interface was developed in order to evaluate wheel slip, motor torque and tip-over based acceleration spaces. The application can also visualize the intersection of the three different vector sets, presenting the overall acceleration capabilities of a kiwi drive based mobile robot. The unidirectionality (isoperimetric ratio) of the closed phase spaces (wheel slip and tip-over) is calculated by using the Alpha shape of the original plot. The automatically

generated Alpha shape can be visualized over the original color plot by setting a checkbox. The Graphical User Interface (GUI) of the application is shown in Fig. 30.

6.3 Comparing holonomic mobile robots

The velocity and acceleration spaces describe and visualize the kinematic and the dynamic capabilities of a mobile robot. These phase spaces can be applied to any types of mobile robots moving in a planar environment.

6.3.1 Braking distance and climbing ability

The maximum (worst case) braking distance and maximum climbing ability can be determined by the selection of the minimum and the maximum vector lengths, respectively, on the top-view cross-section of the acceleration space, which corresponds to zero angular acceleration.

6.3.2 Direction independency

Calculation of the isoperimetric quotient of the closed volume of the phase spaces enables the objective comparison of different types of holonomic drive structures from the point of view of direction dependency.

6.3.3 Standardization efforts in the field of mobile robotics

These performance measurements can be proper methods during the ISO standardization processes focused on the standard comparison of service robots, as the ISO 18646-1 standard is currently under development. The early draft includes instructions to measure speed, braking distance, climbing ability, etc. The proposed methods give a clear recommendation to the aforementioned issues [75].

7 THESIS

In the following, I summarize the novel, applicable results, which were developed during the detailed investigations of kinematic and dynamic phase spaces.

If the top view of the velocity phase space is investigated (Fig. 46), it can be noticed that there are motion states where the robot can reach higher linear velocities if its angular velocity is not zero, thus the robot rotates during horizontal motion.

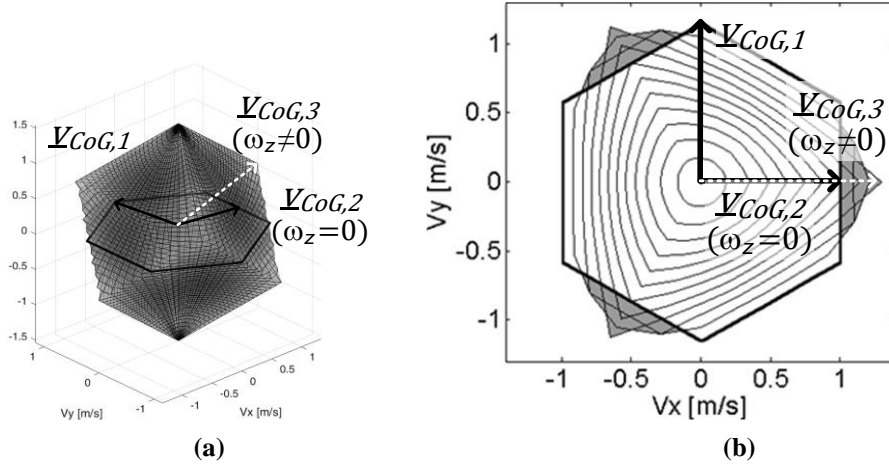


Fig. 46. 3D (a) and bottom view (b) of the velocity phase space. The bold contoured hexagon shows maximum linear velocity in case angular acceleration is zero. Black vectors mark maximum linear velocities in case of zero angular velocity, while the dashed vector is the maximum linear velocity vector when angular velocity is unconstrained.

The relative lengths of the corresponding linear velocity vectors (71) can be calculated by using the Jacobian form of kinematics (69) and by constraining maximum drive directional velocities (70).

$$\begin{bmatrix} v_{CoG,x} \\ v_{CoG,y} \\ \omega_z \end{bmatrix} = \begin{bmatrix} \frac{2}{3} & -\frac{1}{3} & -\frac{1}{3} \\ 0 & \frac{\sqrt{3}}{3} & -\frac{\sqrt{3}}{3} \\ -\frac{1}{3r} & -\frac{1}{3r} & -\frac{1}{3r} \end{bmatrix} \begin{bmatrix} v_{drive,1} \\ v_{drive,2} \\ v_{drive,3} \end{bmatrix} \quad (69)$$

$$v_{drive,i} \in [-1 \dots 1] \quad (70)$$

$$\begin{bmatrix} v_{CoG,1,x} \\ v_{CoG,1,y} \\ \omega_{1,z} \end{bmatrix} = \begin{bmatrix} 0 \\ \frac{2\sqrt{3}}{3} \\ 0 \end{bmatrix}; \quad \begin{bmatrix} v_{CoG,2,x} \\ v_{CoG,2,y} \\ \omega_{2,z} \end{bmatrix} = \begin{bmatrix} 1 \\ 0 \\ 0 \end{bmatrix}; \quad \begin{bmatrix} v_{CoG,3,x} \\ v_{CoG,3,y} \\ \omega_{3,z} \end{bmatrix} = \begin{bmatrix} \frac{4}{3} \\ 0 \\ \frac{1}{3r} \end{bmatrix} \quad (71)$$

It can be calculated that maximum linear velocity is 15.47% higher in case non-zero angular velocity is accepted. This statement led to the investigation whether the robot can reach a nearby goal position within a shorter duration by driving it along a longer circular path instead of the shortest straight path.

7.1 Thesis 1.

Performing a movement between two positions takes less time for a 3-wheeled omnidirectional kiwi drive robot if it moves along a circular path in cases when the linear distance between the two positions is less than six times the radius of the circle coincident with the wheels.

Publications in connection with the above thesis: [P1, P2, P4-P9, P20]

7.1.1 Background explanation

By using the previously calculated higher relative velocity and the length of the corresponding circular path, the marginal utility of the curved path compared to the straight can be derived:

$$\overline{SG} < 8r \cdot \sin\left(\frac{\alpha}{2}\right) \approx 6.34 r \quad (72)$$

where: \overline{SG} is the linear distance between the Start (S) and the Goal (G) positions, r is the radius of the circle coincident with the wheels, and α is the positive, non-zero solution of the following equation:

$$4 \sin\left(\frac{\alpha}{2}\right) = \sqrt{3} \alpha \quad \alpha \approx 1.83 \text{ [rad]} \quad (73)$$

The corresponding motion state and the used notations are shown in Fig. 47.

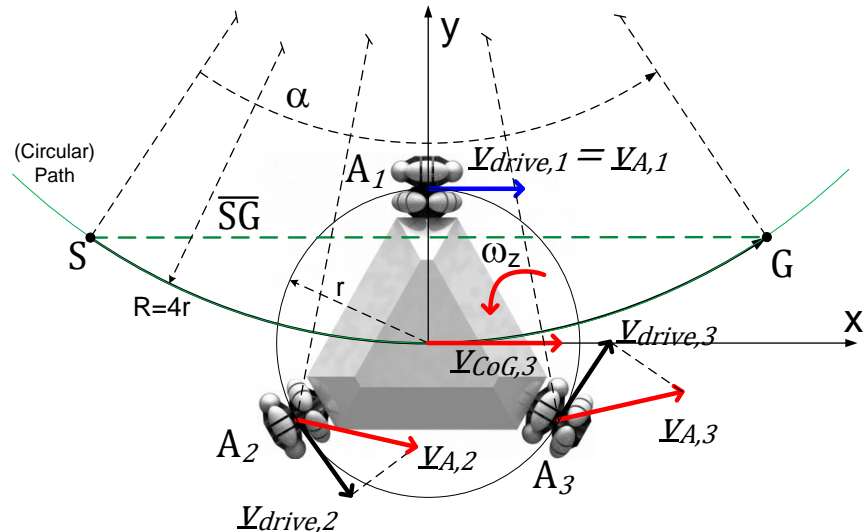


Fig. 47. Actual velocities in case of the circular path which is faster than the straight one, and the applied notations

7.1.2 Practical application

The Ethon robot ($r = 30$ cm) used for experimental measurements can reduce the travel time by 10% of the original time along a one meter long distance.

During my research, experience with different robot geometries showed that the acceleration limits of some robots are more sensitive to direction, while others' are more robust. This initiated the elaboration of a generic unidirectionality quotient which conforms to mobile robotics driven objectives.

7.2 Thesis 2

The unidirectionality of the kinematic and the dynamic capabilities of any planar wheeled mobile robot can be described by a scalar indicator by using the isoperimetric quotient applied to the closed volume of the velocity and to the acceleration phase spaces, respectively.

$$\Psi = \frac{\frac{1}{n^3} (6V_p)^{\frac{2}{3}}}{A_p} \quad (74)$$

where Ψ is the isoperimetric ratio normalized to sphere; and V_p and A_p are the volume and surface area of the measured phase space, respectively.

Publications in connection with the above thesis: [P1-P3, P5, P10-P19]

7.2.1 Background explanation

The isoperimetric quotient is mostly applied in the field of geology, in cases where the sphericity of a stone needs to be determined, thus it can be assumed that significant erosion has taken place in its location. The principle of the isoperimetric quotient is that the sphere has the highest volume per surface area ratio and all other shapes have lower ratios. The isoperimetric ratio normalized to sphere yields a value of 1 in case of a sphere, and lower values in case of all different closed volumes.

The isoperimetric ratio normalized to sphere has the following advantageous characteristics, which enables it to give a comparable performance measure of the direction independency of holonomic mobile robots:

- Dimensionless number between 0 and 1, where a higher value represents a more direction-independent robot.
- The volume is zero in case of surfaces, therefore it yields a value of zero for all non-holonomic kinematics, while
- It yields 1 for absolute unidirectional (direction-independent) cases.
- It can be applied to all planar wheeled mobile robots, as they have two or three dimensional phase spaces.
- It is independent of scale and orientation.
- It is not overly dependent on some extreme point of the phase space, while these points can hardly be used for trajectory planning.

7.2.2 Practical application

The isoperimetric ratio is a generic and objective indicator, which can be applied to all types of planar wheeled mobile robots and represents the direction independency of the motion capabilities of the robot.

In practice, the value of the isoperimetric ratio of the (wheel slip based) acceleration phase space of a 3-wheeled kiwi drive platform is between 0.6 and 0.8. The robot can be considered as strongly direction-dependent in the lower portion of the interval, under 0.7. In this case, the maximum deviation of the maximum length of the velocity or acceleration vector is over 50%.

Having found out the above, during the investigation of the distortion of the wheel slip constrained acceleration phase space caused by the height of the CoG in connection with unidirectionality, I derived the following correspondence:

7.3 Thesis 3.

The unidirectionality of the wheel slip constrained maximum acceleration of a 3-wheeled omnidirectional kiwi drive robot monotonically increases when the height of the center of gravity decreases, but never reaches the sphericity of a regular hexahedron.

$$\lim_{h \rightarrow 0} (\Psi_f(h)) = \lim_{h \rightarrow 0} \left(\frac{\frac{1}{\pi^3} (6V_p(h))^2}{A_p(h)} \right) = \frac{\frac{1}{\pi^3} (6a^3)^2}{6a^2} = \sqrt[3]{\frac{\pi}{6}} \approx 0.806 \quad (75)$$

$$\Psi_f(h) < \sqrt[3]{\frac{\pi}{6}}, \quad \{h \in \mathbf{R} \mid h > 0\} \quad (76)$$

where h is the (positive non-zero) height of the CoG, measured from the ground, Ψ_f is the unidirectionality of wheel slip constrained maximum acceleration, V_p and A_p are respectively the volume and surface area of the wheel slip constrained acceleration phase-space, and a is the length of a regular hexahedron (positive, non-zero, scalar value).

Publications in connection with the above thesis: [P1, P2, P11-P13, P16-P20]

7.3.1 Background explanation

The distinct load forces on the wheels and their effect are the function of the height of the CoG measured from the ground, where the negligence of the changing load forces corresponds to the zero height of the CoG. This simplification causes the same cubical shape as in case of the velocity space [34], see Fig. 48/a, in which the top view cross section at zero angular acceleration is a regular hexagon. As the height of the CoG is increasing, the original hexahedron is being distorted continuously (Fig. 48/b).

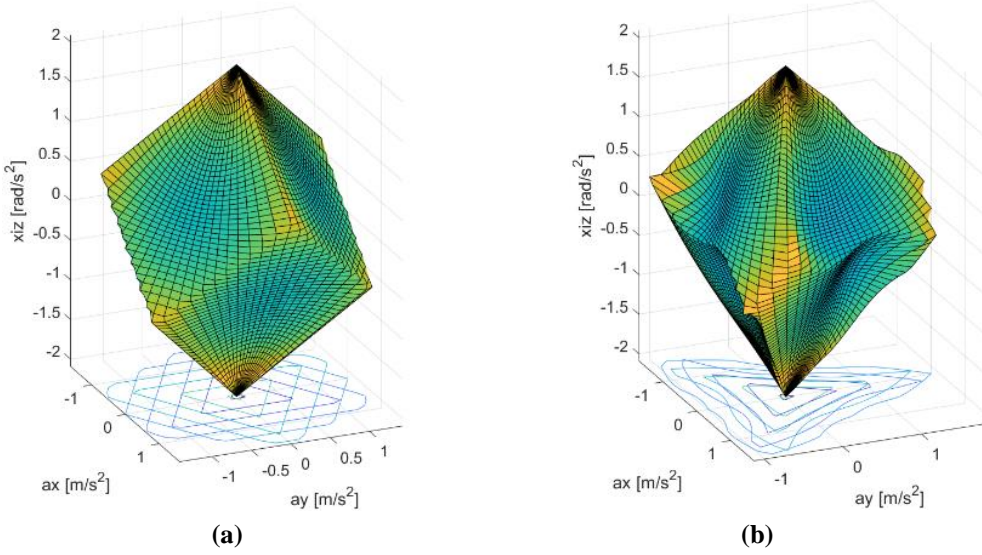


Fig. 48. Wheel slip based acceleration phase spaces of the robot in case of neglecting (a) and considering (b) the effect of the CoG height.

I have investigated the correspondence between the distortion and the direction independency by running numerical calculations, where the isoperimetric quotient was calculated according to the 2nd thesis in case of different heights of the CoG (see Fig. 49).

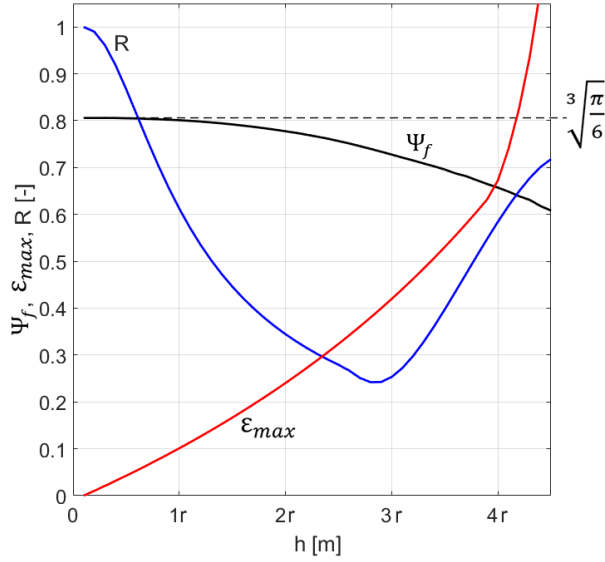


Fig. 49. Unidirectionality as the function of CoG height (Ψ_f), maximum error (ϵ_{max}) and linear correlation (R) of vector length compared to the case of zero CoG height. r is the radius of the circle coincident with the wheels.

During simulation, the maximum relative error, $\epsilon_{max}(h)$ and the linear correlation $R(h)$ were also calculated, compared to the model which neglects the height of the CoG.

The result proves that direction independency decreases as the height of the CoG increases. Furthermore, it can be observed that the generic unidirectionality quotient

starts to decrease asymptotically from the value of the isoperimetric ratio of the regular hexahedron (approximate: 0.806).

7.3.2 Practical application

In practice, the maximum relative error (ε_{\max}) is over $\pm 25\%$ when the height of the CoG (h) is higher than the diameter of the circle coincident with the wheels ($2r$) compared to the model which neglects the vertical position of the CoG. In this case ($h > 2r$), the wheels can slip irregularly and it is recommended to use a model which handles the effect of the vertical position of the CoG. Therefore, wheel slip can be avoided in a way that the immanent characteristics of acceleration capabilities remain utilized by allowing higher accelerations in favorable directions.

According to the above evaluation, the calculated value of unidirectionality assists decisions on a possible simplification – or maybe the absolute negligence – of the direction-dependent model which is used for controlling robot motion.

In order to assist the applicability of the dynamic model above, a C++ implementation is shared, based on the open source Robot Operating System (ROS). The algorithm can be parametrized by simple measurements, without the necessity of any special equipment.

Also by using this model, a Matlab application user interface was developed in order to evaluate wheel slip, motor torque and tip-over based acceleration spaces. The application can also visualize the intersection of the three different vector sets, presenting the overall acceleration capabilities of a kiwi drive based mobile robot. The unidirectionality (isoperimetric ratio) of closed phase spaces (wheel slip and tip-over) is calculated by using the Alpha shape of the original plot. The automatically generated Alpha shape can be visualized over the original color plot by setting a checkbox. The Graphical User Interface (GUI) of the application is shown in Fig. 50.

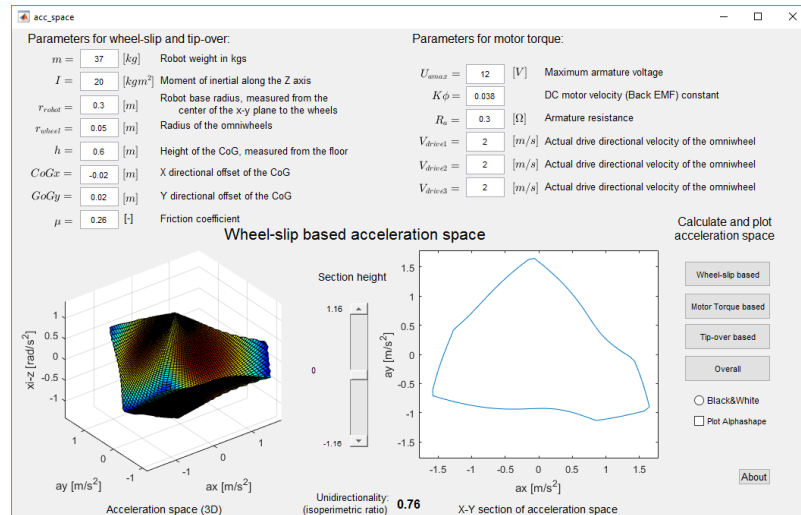


Fig. 50. Matlab application for assisting the robot design process

8 TÉZISEK MAGYARUL

A továbbiakban a kiwi hajtású robot kinematikai és dinamikai fázistereinek részletesebb vizsgálata során fellelt új, alkalmazható eredményeket mutatom be.

A kinematikai fázistér $\omega_z = 0$ (nulla szögsebesség) felülnézeti síkját és a teljes fázistér felülnézetét tekintve („0” ábra) belátható, hogy vannak olyan mozgásállapotok mely esetekben a robot nagyobb lineáris sebesség elérésére képes, ha a szögsebessége nem nulla, azaz helyváltoztatás közben forgómozgást is végez.

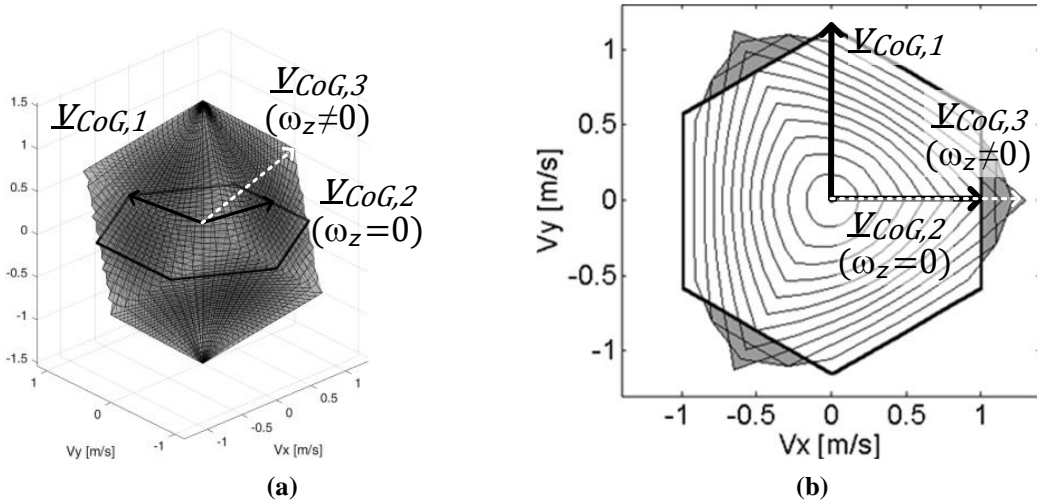


Fig. 51. Kiwi hajtású robot kinematikai fázisterének 3D és alulnézete, ahol a vastag hatszög jelöli a nulla szögsebességhoz tartozó síkot. A nulla szögsebességnél irányonként elérhető maximális lineáris sebességet fekete vektorok ($v_{CoG,1}$ és $v_{CoG,2}$) jelölik, míg a nem nulla szögsebességhoz a fehér szaggatott vektor ($v_{CoG,3}$) tartozik.

A vonatkozó sebességvektorok (79) lineáris komponenseinek relatív hossza a kinematikai kényszerek Jacobi alakjával (77) és a kerekek maximális hajtásirányú sebességének egységnyi megválasztásával (78) határozható meg.

$$\begin{bmatrix} v_{CoG,x} \\ v_{CoG,y} \\ \omega_z \end{bmatrix} = \begin{bmatrix} \frac{2}{3} & -\frac{1}{3} & -\frac{1}{3} \\ 0 & \frac{\sqrt{3}}{3} & -\frac{\sqrt{3}}{3} \\ -\frac{1}{3r} & -\frac{1}{3r} & -\frac{1}{3r} \end{bmatrix} \begin{bmatrix} v_{drive,1} \\ v_{drive,2} \\ v_{drive,3} \end{bmatrix} \quad (77)$$

$$v_{drive,i} \in [-1 \dots 1] \quad (78)$$

$$\begin{bmatrix} v_{CoG,1,x} \\ v_{CoG,1,y} \\ \omega_{1,z} \end{bmatrix} = \begin{bmatrix} 0 \\ \frac{2\sqrt{3}}{3} \\ 0 \end{bmatrix}; \quad \begin{bmatrix} v_{CoG,2,x} \\ v_{CoG,2,y} \\ \omega_{2,z} \end{bmatrix} = \begin{bmatrix} 1 \\ 0 \\ 0 \end{bmatrix}; \quad \begin{bmatrix} v_{CoG,3,x} \\ v_{CoG,3,y} \\ \omega_{3,z} \end{bmatrix} = \begin{bmatrix} \frac{4}{3} \\ 0 \\ \frac{1}{3r} \end{bmatrix} \quad (79)$$

A fenti – robot koordinátarendszerben értelmezett – vektorokat összehasonlítva belátható, hogy a forgó mozgást is megengedve 15,47%-al nagyobb lineáris sebesség

érhető el. E megállapítás vezetett annak vizsgálatához, hogy célszerű lehet-e a robotnak az egyenes helyett egy körív pályán haladnia egy közelí pozíció gyorsabb eléréséhez.

1. tézis

Két pont közötti utat az egyenesnél rövidebb idő alatt tesz meg körív pályán egy háromkerekű omnidirekcionális kiwi hajtású robot, ha a pontok egyenes vonalon mért távolsága kisebb, mint a robot alapkörének a sugarának hatszorosa.

Kapcsolódó publikációk: [P1, P2, P4-P9, P20]

8.1.1 Háttér magyarázat

Tekintetbe véve a körív pálya – start és cél pontok között – euklideszi távolság nál nagyobb hosszát, valamit a körív pályán elérhető nagyobb sebességet, az alábbi összefüggéssel írható le a körív pálya egyenes pályához viszonyított határhaszná:

$$\overline{SG} < 8r \cdot \sin\left(\frac{\alpha}{2}\right) \approx 6.34 r \quad (80)$$

ahol: \overline{SG} a start (S) és a cél (G) pontok között mért euklideszi távolság, r a robot alapkörének sugara, amely a kerekek tapadási pontjain halad át, α pedig a következő egyenlet pozitív, nem nulla megoldása:

$$4 \sin\left(\frac{\alpha}{2}\right) = \sqrt{3} \alpha \quad \alpha \approx 1.83 \text{ [rad]} \quad (81)$$

A vonatkozó mozgásállapotot és az alkalmazott jelöléseket a „Fig. 52” ábra szemlélteti.

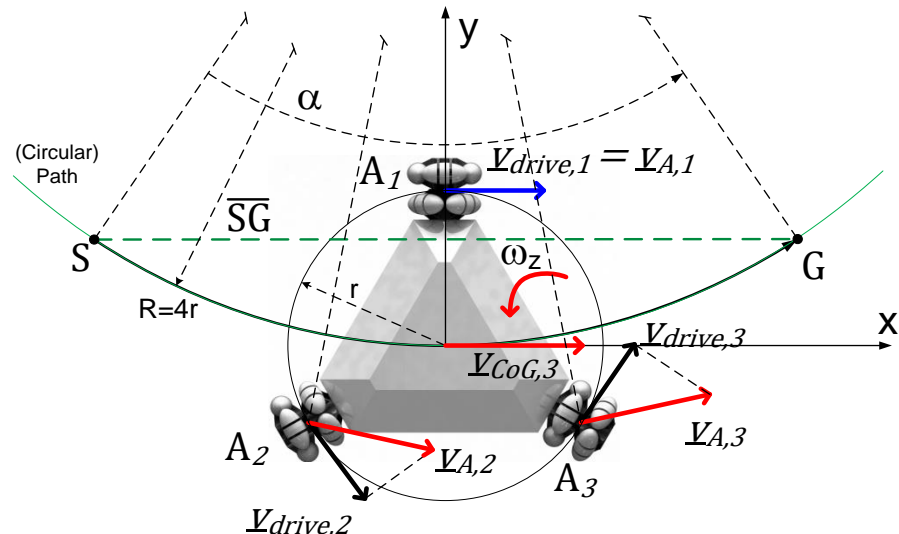


Fig. 52. Az egyenesnél gyorsabb, körív menti mozgáspálya pillanatnyi sebesség vektorai és az alkalmazott jelölések

8.1.2 Gyakorlati alkalmazás

A mérésekhez használt robot esetében, ahol $r = 30$ cm, az eredeti menetidő 10%-al csökken, ha a robot a gyorsabb, körív pályán halad egy 1 méterre lévő cél eléréséhez.

Kutatási tevékenységem során azonos holonomikus hajtástípusok esetén is, az eltérő geometria miatt jelentős eltéréseket tapasztaltam a kinematikai és dinamikai fázisterek alakjai-, így a robotok kinematikai és dinamikai irányfüggetlensége között. Ennek okán határoztam meg a robotok kinematikai és dinamikai fázisterének jellegére vonatkoztatott általános irányfüggetlenségi tényezőt, amely az alkalmazhatósági szempontrendszernek megfelelve szolgál objektív indikátorként:

8.2 2. tézis

Minden, síkon mozgó, kerék hajtotta mobil robot kinematikai és dinamikai irányfüggetlensége az alábbi összefüggés szerinti skalár mérőszámmal jellemzhető, rendre az általánosított koordináták szerinti fázisterek zárt térfogatára alkalmazott izoperimetrikus hányados gömbre normalizált alakjával.

$$\Psi = \frac{\pi^{\frac{1}{3}} (6V_p)^{\frac{2}{3}}}{A_p} \quad (82)$$

ahol V_p a fázistér térfogata, A_p a fázistér határfelületének területe, Ψ pedig a gömbre normalizált izoperimetrikus hányados.

Kapcsolódó publikációk: [P1-P3, P5, P10-P19]

8.2.1 Háttér magyarázat

Az izoperimetrikus hányados meghatározása elsősorban a geológiában jellemző vizsgálati módszer, ahol a közelminták szabályos gömbtől való eltérésének mérőszámaként alkalmazzák. Elve, hogy a gömb alakzat térfogat/felület aránya a legnagyobb, és minden ettől eltérő forma esetében az arányszám alacsonyabb. Az izoperimetrikus hányados gömbre normalizált alakja gömb esetén 1-et, míg minden attól eltérő zárt térbeli alakzat esetén kisebb skalár értéket ad.

Az izoperimetrikus hányados az alábbi tulajdonságai miatt bizonyul alkalmas eszköznek a robotok irányfüggetlenségének leírására:

- 0 és 1 közötti, dimenzió nélküli szám, ahol a nagyobb szám irányfüggetlenebb robotot jelöl.
- Felület esetén a tár fogat nulla, emiatt minden nem holonomikus robot kinematika esetében nulla értéket ad,
- míg teljesen irányfüggetlen esetben veszi fel az 1 értéket.
- minden síkon mozgó mobil robotra, azaz két vagy háromdimenziós fázistérre alkalmazható.
- Nem függ a mértéktől és az orientációtól.
- Nem függ aránytalan mértékben pár esetleges extrém pontjától a fázistérnek, az ilyen pontok csak nehézkesen használhatóak a pályatervezés során.

8.2.2 Gyakorlati alkalmazás

Az izoperimetrikus hárnyados valamennyi síkon mozgó, kerék hajtotta mobilrobot esetében egy objektív, összehasonlító mérőszámként alkalmazható, amely megmutatja, hogy az adott robot mozgási képességei milyen mértékben irány függetlenek.

A gyakorlatban egy kiwi hajtású holonomikus mobilrobot kinematikai és dinamikai irányfüggetlenségi tényezői nagyságrendileg a 0,6-0,8 tartományba esnek. A tartomány alsó felében, 0,7 alatti érték esetén a robot fázistere jelentősen irányfüggőnek tekinthető, ekkor már 50%-nál nagyobb eltérések tapasztalhatók a maximális sebesség vagy gyorsulás mértékében az irány változásával.

A fenti tapasztalatokat követően, a gyorsulástér súlypont helyzetétől függő torzulása, valamit az ezzel összefüggő irányfüggetlenség vizsgálata során jutottam a következő megállapításra:

8.3 3. tézis

Egy háromkerekű omnidirekcionális kiwi hajtású robot kerekek tapadása által meghatározott maximális gyorsulásának az általános irányfüggetlenségi tényezője (szigorúan monoton) nő a súlypont földtől mért távolságának csökkenésével, azonban sohasem éri el a szabályos hexaéder gömbre normalizált izoperimetrikus hányadosát.

$$\lim_{h \rightarrow 0} (\Psi_f(h)) = \lim_{h \rightarrow 0} \left(\frac{\frac{1}{\pi^3} (6V_p(h))^{\frac{2}{3}}}{A_p(h)} \right) = \frac{\frac{1}{\pi^3} (6a^3)^{\frac{2}{3}}}{6a^2} = \sqrt[3]{\frac{\pi}{6}} \approx 0.806 \quad (83)$$

$$\Psi_f(h) < \sqrt[3]{\frac{\pi}{6}}, \quad \{h \in \mathbf{R} \mid h > 0\} \quad (84)$$

ahol h a robot súlypontjának földtől mért (pozitív nem nulla) távolsága, Ψ_f kerekek tapadása által meghatározott maximális gyorsulás általános irányfüggetlenségi tényezője, V_p és A_p rendre a kerekek tapadása által meghatározott dinamikai fázistér térfogata illetve határfelületének területe, a pedig egy szabályos hexaéder élének hossza (tetszőleges pozitív, nem nulla, skalár érték).

Kapcsolódó publikációk: [P1, P2, P11-P13, P16-P20]

8.3.1 Háttér magyarázat

A kerekeken mérhető terheléseloszlás változása és annak hatása a súlypont föltől mért távolságának függvénye, ahol a változó terheléseloszlás elhanyagolása egy nulla magasságú súlypontnak felelhető meg. Utóbbi egyszerűsítés egy - a kinematikai fázistérhez hasonló - hexaéder alakú fázisteret eredményez („Fig. 53”/a ábra), amelynek a nulla szöggyorsuláshoz tartozó felülnézeti metszete egy szabályos hatszög. A súlypont helyzetének emelkedésével a hexaéder folytonos, három tengely szerinti szimmetrikus torzulása tapasztalható („Fig. 53”/b ábra).

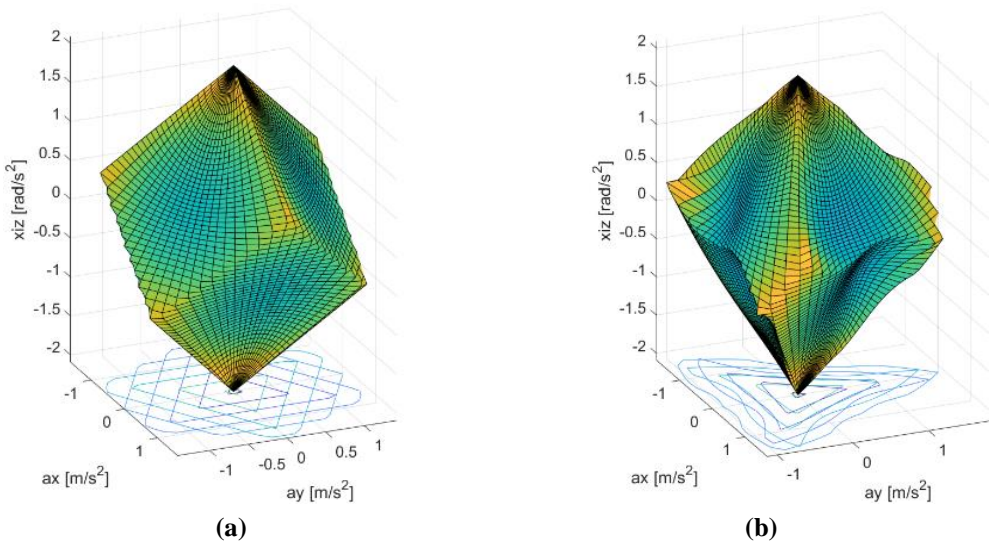


Fig. 53. A súlypont helyzetének hatását elhanyagoló (a), illetve figyelembe vevő (b) kiwi hajtású mobilrobot gyorsulás fázistere

A torzulás és az irányfüggetlenség közötti összefüggést numerikus szimulációval vizsgáltam, melynek során a 2. tézis során ismertetett izoperimetrikus hányadost határoztam meg az eltérő magasságú súlyponthoz tartozó dinamikai fázisterek esetén („Fig. 54” ábra).

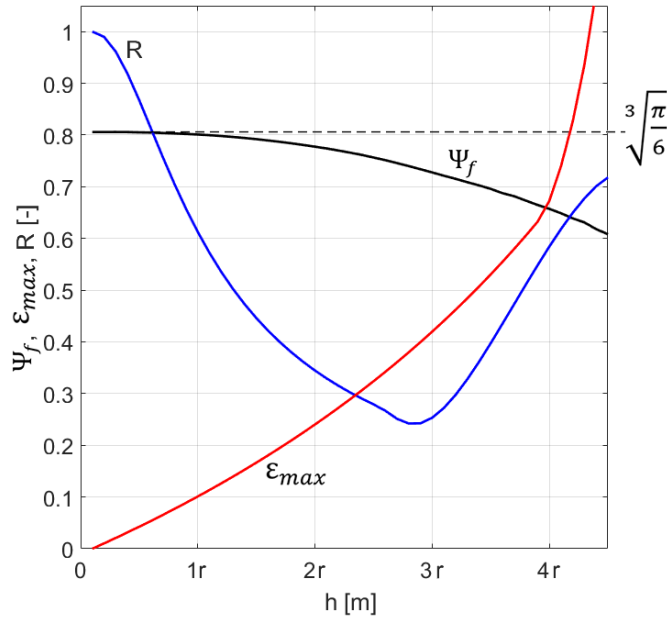


Fig. 54. Általános irányfüggetlenségi tényező (Ψ_f), maximális relatív hiba (ε_{max}) és lineáris korreláció (R) a súlypont helyzetét elhanyagoló modellhez képest a súlypont föltől mért magasságának (h) függvényében. r a robot alapkörének sugara, amely körvonal a kerekek tapadási pontjain halad át.

A szimuláció során továbbá meghatároztam a súlypont helyzetét elhanyagoló, hexaéder formájú fázistérhez viszonyított:

- irányfüggően megcsúszást okozó maximális eltérést: $\epsilon_{\max}(h)$
- és a lineáris korrelációt: $R(h)$.

Ez eredmény igazolja, hogy az irányfüggetlenség a súlypont helyzetének emelkedésével csökken. E mellett az is leolvasható, hogy az irányfüggetlenségi tényező értéke a szabályos hexaéder izoperimetrikus hányadosának értékétől (közelítően: 0,806) aszimptotikusan kezd el távolodni a fázistér folyamatos torzulása révén.

8.3.2 Gyakorlati alkalmazás

A 9. ábra egyben azt is mutatja, hogyha a súlypont a robot alapkörének átmérőjénél ($2r$) magasabban helyezkedik el, akkor az egyszerűsített modell irányfüggő maximális relatív hibája (ϵ_{\max}) meghaladja a $\pm 25\%$ -ot, ami másfélszeres ingadozást jelent egy a súlypont hatását elhanyagoló módszerhez képest, ami a kerekek látszólag rendszertelen és váratlan megcsúszását okozza. Ekkor a robot dinamikai korlátainak meghatározásához célszerű a súlypont helyzetének hatását is modellező eljárás alkalmazása. Ennek révén a robot kerekeinek csúszása úgy kerülhető el, hogy más, kedvezőbb irányokba viszont nem szükséges túlzott mértékben korlátozni a gyorsulást.

A fentiek alapján az általános irányfüggetlenségi tényező helyes megállapítása általánosan is iránymutatást nyújt annak eldöntésére, hogy bármely síkon mozgó mobilrobot irányítása során milyen mértékben egyszerűsíthetjük – vagy akár hanyagolhatjuk el – a robot iránytól függő dinamikai sajátosságait.

A módszer alkalmazhatósága végett a nyílt forráskódú *Robot Operating System* (ROS) keretrendszerbe beépülő, C++ nyelven implementált dinamikai algoritmust dolgoztam ki. Az algoritmus különleges eszközöket nem igénylő mérések révén, egyszerűen paraméterezhető tetszőleges kiwi hajtású robot irányítására.

Szintén e modell alkalmazásával készítettem egy a dinamikai fázisteret ábrázoló, a robottervezést támogató szoftvert, amely nem csak a kerekek csúszását, hanem a meghajtó motorok maximális nyomatékát és a robot esetleges felborulását is peremfeltételként kezeli. Ennek révén a geometria egyedi igényekhez igazodó optimalizálása mellett, a motorok és áttetelek helyes megválasztása is lehetővé válik. A szoftver felhasználói felülete a „Fig. 55” ábrán látható.

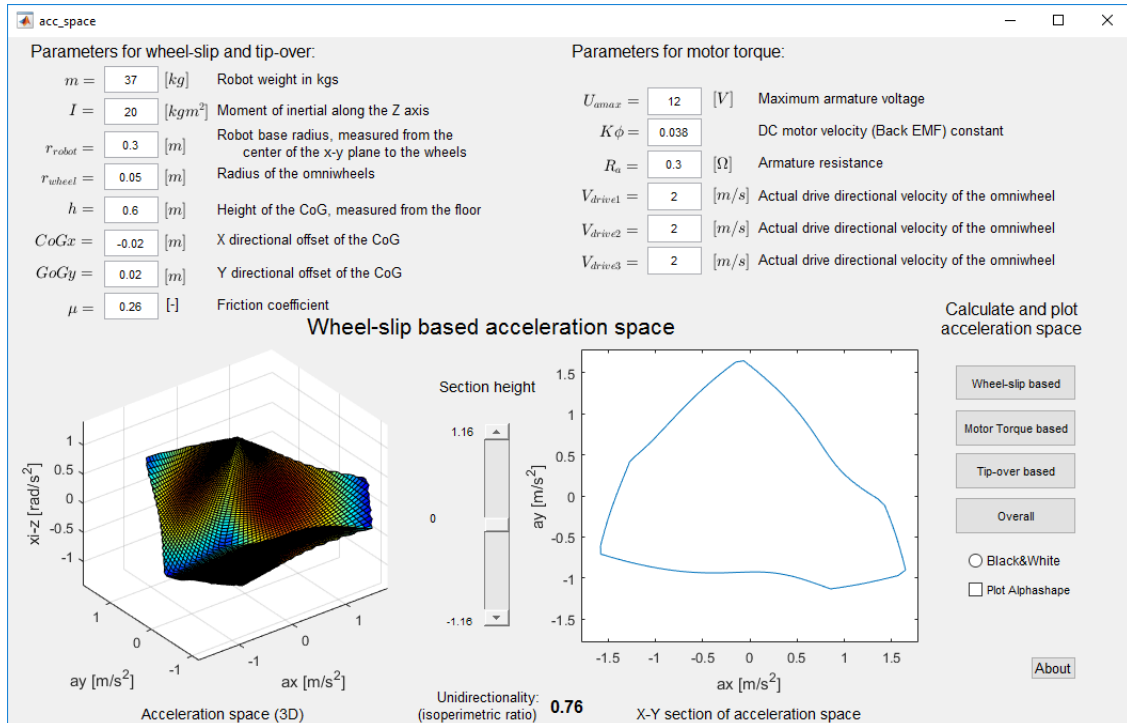


Fig. 55. Kiwi hajtású robot tervezését támogató szoftver

APPENDIX

The Matlab source code with the compiled executable (exe) and the ROS C++ catkin package are available as a supplementary material on www.sciencedirect.com or it can be downloaded directly from the author's website: www.generalmechatronics.com/doc/publ/HolonomicDrive_Elsevier2017.zip

AUTHOR'S PUBLICATIONS

- [P1] G. Szayer, B. Kovács, F. Tajti, P. Korondi, “Feasible utilization of the inherent characteristics of holonomic mobile robots,” *Elsevier Robotics and Autonomous Systems*, 2017, DOI:10.1016/j.robot.2017.04.002., IF: 1.95 (2016)
- [P2] B. Kovács, G. Szayer, F. Tajti, M. Burdelis, P. Korondi, “A Novel Potential Field Method for Path Planning of Mobile Robots by Adapting Animal Motion Attributes,” *Elsevier Robotics and Autonomous Systems*, 2016, DOI: 10.1016/j.robot.2016.04.007., IF: 1.95
- [P3] F. Tajti, B. Kovács, G. Szayer, P. Korondi, “Variable Robot Geometry Optimization Method to Avoid Tip Over Situations During Slow Motion on Unknown Terrains,” *Acad. Appl. Res. Mil. PUBLIC Manag. Sci.* 15 pp. 301-323, 2016.
- [P4] F. Tajti, G. Szayer, B. Kovács, P. Barna, P. Korondi, “Optical flow based odometry for mobile robots supported by multiple sensors and sensor fusion,” *Automatika*. 57 pp. 201–211, 2016, DOI:10.7305/automatika.2016.07.886., IF: 0.38
- [P5] F. Tajti, G. Szayer, B. Kovács, M.A.P. Burdelis, “Mobile Robot Performance Analysis for Indoor Robotics,” *Period. Polytech. Civ. Eng.*, pp. 123–131, 2015., IF: 0.271
- [P6] B. Kovács, G. Szayer, F. Tajti, “Design of a universal robot controller,” *Periodica Polytechnica-Mechanical Engineering* 55:(2) pp. 95-100, 2011.
- [P7] F. Tajti, G. Szayer, B. Kovács, P. Korondi, “Shop-floor controller based on RT-middleware technology,” *Journal Of Mechanics Engineering And Automation* 3:(11) pp. 686-694, 2013, Paper 3-JMEA-E20130808-1.
- [P8] F. Tajti, G. Szayer, B. Kovács, P. Korondi, “Industrial robotics for ERP controlled smart factories,” *Recent Innovations in Mechatronics (RIiM) Vol. 2. (2015). No. 1-2.* pp. 1-9, 2015, DOI:10.17667/riim.2015.1-2/6.source.
- [P9] G. Szayer, B. Kovács, B. Varga, “Universal robot controller,” *Workshop on Cognitive and Eto-Robotics in iSpace CERiS'10. Budapest, Hungary*, 2010.
- [P10] G. Szayer, B. Kovács, B. Varga, P. Korondi, “RT Middleware based robot controller,” *Proceedings of the 7th International Conference on Mechanical Engineering (Gépészeti 2010). Budapest, Hungary*, 2010, Paper 13. ISBN: 978-963-313-007-0
- [P11] G. Szayer, B. Kovács, B. Varga, “Etho-robot,” *Workshop on Cognitive and Eto-Robotics in iSpace CERiS'10. Budapest, Hungary*, 2010.

- [P12] B. Kovács, G. Szayer, F. Tajti, P. Korondi, I. Nagy, “Robot with Dog Type Behavior,” *International Conference on Electrical Drives and Power Electronics*, pp. 347-352, High Tatras, Slovakia, 2011.
- [P13] F. Tajti, G. Szayer, B. Kovács, P. Korondi, “Holonomic based robot for behavioral research,” *Workshop on Cognitive and Eto-Robotics in iSpace 2013, Budapest, Hungary*, 2013.
- [P14] F. Tajti, G. Szayer, B. Kovács, P. Korondi, “Universal RT-middleware robot controller,” *Proceedings of the IECON 2013 - 39th Annual Conference of the IEEE Industrial Electronics Society*. pp. 1-6, Vienna, Austria, 2013, ISBN: 978-1-4799-0223-1
- [P15] F. Tajti, G. Szayer, B. Kovács, B. Dánial, P. Korondi, “CRM TC covering paper - Robotics trends,” *Proceedings of the IECON 2013 - 39th Annual Conference of the IEEE Industrial Electronics Society*, pp. 48-53, Vienna, Austria, 2013, Vienna: IEEE, Paper VF-052493. ISBN: 978-1-4799-0223-1, DOI:10.1109/IECON.2013.6699110.
- [P16] F. Tajti, G. Szayer, B. Kovács, P. Korondi, “Robot base with holonomic drive,” *The 19th World Congress of the International Federation of Automatic Control*, 2014. August, 24-29.
- [P17] B. Kovács, G. Szayer, F. Tajti, V. Devecseri, P. Korondi, “Szociális robotok a 21. században: MOGI Robi a hűséges társ,” *Erdélyi Magyar Műszaki Tudományos Társaság. Kolozsvár, Románia*, pp. 238-241, 2012.04.19.
- [P18] F. Tajti, B. Kovács, G. Szayer, P. Tamás, “Rendvédelmi szerveknél alkalmazható mobil robotok és beágyazott rendszerek,” *Proceedings of ARES’14 Work. Appl. Robot. Enhanc. Secur.*, pp. 85-89, Budapest, Hungary, 2014.06.13-2014.06.14.
- [P29] Kovács B., Tajti F., Szayer G., Tamás P., “Nyílt forráskódú Linux RTAI alapú 3D nyomtató vezérlés,” *Proc. ARES’14 Work. Appl. Robot. Enhanc. Secur.*, pp. 35-38, Budapest, Hungary, 2014.
- [P20] Szayer G., Kovács B., Tajti F., Tamás P., “GPS-GSM alapú útdíj fizetés műszaki nehézségei,” *Proc. ARES’14 Work. Appl. Robot. Enhanc. Secur.*, pp. 48–53, Budapest, Hungary, 2014.

BIBLIOGRAPHY

- [1] G. Lakatos *et al.*, “Emotion attribution to a non-humanoid robot in different social situations,” *PLoS One*, vol. 9, no. 12, 2014.
- [2] A. El-Shenawy, A. Wagner, and E. Badreddin, “Dynamic model of a holonomic mobile robot with actuated caster wheels,” *9th Int. Conf. Control. Autom. Robot. Vision, 2006, ICARCV '06*, 2006.
- [3] J. H. Chung, B. Yi, W. K. Kim, and H. Lee, “The dynamic modeling and analysis for an omnidirectional mobile robot with three caster wheels,” *2003 IEEE Int. Conf. Robot. Autom. (Cat. No.03CH37422)*, vol. 1, pp. 521–527, 2003.
- [4] Y. Mori, E. Nakano, T. Takahashi, and K. Takayama, “A study on the mechanism and control of omni-directional vehicle,” *Proc. IEEE/RSJ Int. Conf. Intell. Robot. Syst. IROS '96*, vol. 1, pp. 52–59, 1996.
- [5] M. Wada and S. Mori, “Holonomic and omnidirectional vehicle with conventional tires,” *Proc. 1996 IEEE Int. Conf. Robot. Autom.*, vol. 4, no. April, pp. 3671–3676, 1996.
- [6] B. Li, H. Du, W. Li, and Y. Zhang, “Side-slip angle estimation based lateral dynamics control for omni-directional vehicles with optimal steering angle and traction/brake torque distribution,” *Mechatronics*, vol. 30, pp. 348–362, 2015.
- [7] K. L. Moore and N. S. Flann, “Hierarchical task decomposition approach to path planning and control for an omni-directional autonomous mobile robot,” *Proc. 1999 IEEE Int. Symp. Intell. Control Intell. Syst. Semiot. (Cat. No.99CH37014)*, pp. 302–307, 1999.
- [8] D. Xu, D. Zhao, J. Yi, and X. Tan, “Trajectory tracking control of omnidirectional wheeled mobile manipulators: robust neural network-based sliding mode approach,” *IEEE Trans. Syst. Man. Cybern. B. Cybern.*, vol. 39, no. 3, pp. 788–99, 2009.
- [9] S. M. Killough and F. G. Pin, “A fully omnidirectional wheeled assembly for robotic vehicles,” *Trans. Am. Nucl. Soc.*, vol. 61, pp. 425–426, 1990.

- [10] F. G. Pin and S. M. Killough, “Design of an Omnidirectional and Holonomic Wheeled Platform Prototype,” *Proc. 1992 IEEE International Conf. Robot. Autom.*, pp. 84–90, 1992.
- [11] F. G. Pin and S. M. Killough, “New family of omnidirectional and holonomic wheeled platforms for mobile robots,” *IEEE Trans. Robot. Autom.*, vol. 10, no. 4, pp. 480–489, 1994.
- [12] M. West and H. Asada, “Design of a holonomic omnidirectional vehicle,” *Proceedings 1992 IEEE International Conference on Robotics and Automation*. pp. 97–103, 1992.
- [13] G. Runge, G. Borchert, and A. Raatz, “Design of a holonomic ball drive for mobile robots,” *MESA 2014 - 10th IEEE/ASME Int. Conf. Mechatron. Embed. Syst. Appl. Conf. Proc.*, 2014.
- [14] J. Myung-Jij, S. Hyun-Sik, K. Heung-Soo, and K. Jong-Hwan, “The Miniature Omni-directional Mobile Robot OmniKity-I (OK-I),” *Proc. Int. Conf. Robot. Autom.*, pp. 2685–2691, 1999.
- [15] O. M. B. Ok-i, M. Jung, H. Kim, S. Kim, and J. Kim, “Omnidirectional mobile base OK-II,” *Proc. 2000 ICRA. Millenn. Conf. IEEE Int. Conf. Robot. Autom. Symp. Proc. (Cat. No.00CH37065)*, vol. 4, no. April, pp. 3449–3454, 2000.
- [16] G. Campion, G. Bastin, and B. D’andrea-Novel, “Structural properties and classification of kinematic and dynamic models of wheeled mobile robots,” *IEEE Trans. Robot. Autom.*, vol. 12, no. 1, pp. 47–62, 1996.
- [17] J. A. Vázquez and M. Velasco-Villa, “Computed-torque control of an omnidirectional mobile robot,” *2007 4th Int. Conf. Electr. Electron. Eng. ICEEE 2007*, no. Iceeee, pp. 274–277, 2007.
- [18] M. Velasco-Villa, Rodríguez-Cortés, Estrada-Sánchez, H. Sira-Ramírez, and J. A. Vázquez, “Dynamic Trajectory-Tracking Control of an Omnidirectional Mobile Robot Based on a Passive Approach,” *Adv. Robot Manip.*, pp. 299–314, 2007.
- [19] K. Kanjanawanishkul and A. Zell, “Path following for an omnidirectional mobile robot based on model predictive control,” *Robot. Autom. 2009. ICRA ’09. IEEE Int. Conf.*, pp. 3341–3346, 2009.

- [20] E. A.-B. and M. V.-V. P. A. Nino-Suarez, “Discrete-time sliding mode path-tracking control for a wheeled mobile robot,” *Proc. 45th IEEE Conf. Decis. Control*, pp. 3052–3057, 2006.
- [21] M. Velasco-Villa, A. Alvarez-Aguirre, and G. Rivera-Zago, “Discrete-time control of an omnidireccional mobile robot subject to transport delay,” *Proc. Am. Control Conf.*, pp. 2171–2176, 2007.
- [22] K. Khanh, P. Hung, and N. Trung, “Trajectory tracking control of omnidirectional mobile robot using sliding mode controller,” *Control. Autom. ...*, no. Iccas, pp. 1170–1175, 2013.
- [23] S. Kao, W. Chiou, and M. Ho, “Integral sliding mode control for trajectory tracking control of an omnidirectional mobile robot,” *Control Conf. (ASCC), 2011 ...*, pp. 765–770, 2011.
- [24] P. Ganguly, T. Kalmár-Nagy, and R. D’Andrea, “Real-time trajectory generation for omnidirectional vehicles,” *Proc. Am. Control Conf.*, no. Cm, pp. 286–291, 2002.
- [25] K. B. Kim and B. K. Kim, “Minimum-time trajectory for three-wheeled omnidirectional mobile robots following a bounded-curvature path with a referenced heading profile,” *IEEE Trans. Robot.*, vol. 27, no. 4, pp. 800–808, 2011.
- [26] T. Kalmár-Nagy, “Real-time trajectory generation for omni-directional vehicles by constrained dynamic inversion,” *Mechatronics*, vol. 35, pp. 44–53, 2016.
- [27] M. Galicki, “Collision-free control of an omni-directional vehicle,” *Rob. Auton. Syst.*, vol. 57, no. 9, pp. 889–900, 2009.
- [28] D. Bruijnen, J. van Helvoort, and R. van de Molengraft, “Realtime motion path generation using subtargets in a rapidly changing environment,” *Rob. Auton. Syst.*, vol. 55, no. 6, pp. 470–479, 2007.
- [29] D. J. Balkcom, P. A. Kavathekar, and M. T. Mason, “Time-optimal Trajectories for an Omni-directional Vehicle,” *Int. J. Rob. Res.*, vol. 25, 2006.

- [30] H.-C. Huang, “SoPC-Based Parallel ACO Algorithm and its Application to Optimal Motion Controller Design for Intelligent Omnidirectional Mobile Robots,” *IEEE Trans. Ind. Informatics*, vol. 9, no. 4, pp. 1828–1835, 2013.
- [31] J. Conradt, F. Galluppi, and T. C. Stewart, “Trainable sensorimotor mapping in a neuromorphic robot,” *Rob. Auton. Syst.*, vol. 71, pp. 60–68, 2015.
- [32] F. Tajti, G. Szayer, B. Kovács, and M. A. P. Burdelis, “Mobile robot performance analysis for indoor robotics,” *Period. Polytech. Civ. Eng.*, vol. 59, no. 2, pp. 123–131, 2015.
- [33] P. F. Muir and C. P. Neuman, “Kinematic modeling for feedback control of an omnidirectional wheeled mobile robot,” *Proc. Int. Conf. Robot. Autom.*, pp. 1772–1778, 1987.
- [34] J. Wu, R. L. Williams, and J. Lew, “Velocity and Acceleration Cones for Kinematic and Dynamic Constraints on Omni-Directional Mobile Robots,” *J. Dyn. Syst. Meas. Control*, vol. 128, no. 4, p. 788, 2006.
- [35] R. Balakrishna and A. Ghosal, “Modeling of Slip For Wheeled Mobile Robots,” *IEEE Trans. Robot. Autom.*, vol. 11, no. 1, pp. 126–132, 1995.
- [36] B. Carter, M. Good, M. Dorohoff, J. Lew, and R. L. W. Ii, “Mechanical Design and Modeling of an Omni-directional RoboCup Player 1 Introduction 2 Design,” *Mech. Eng.*, pp. 1–6, 2000.
- [37] R. L. Williams, B. E. Carter, P. Gallina, and G. Rosati, “Dynamic model with slip for wheeled omnidirectional robots,” *IEEE Trans. Robot. Autom.*, vol. 18, no. 3, pp. 285–293, 2002.
- [38] F. Tajti, G. Szayer, B. Kovács, P. Barna, and P. Korondi, “Optical flow based odometry for mobile robots supported by multiple sensors and sensor fusion,” *Autom. – J. Control. Meas. Electron. Comput. Commun.*, vol. 57, no. 1, pp. 201–211, 2016.
- [39] J. B. Holland, M. J. D. Hayes, and R. G. Langlois, “A slip model for the spherical actuation of the atlas motion platform,” *Trans. Can. Soc. Mech. Eng.*, vol. 29, no. 4, pp. 711–720, 2005.

- [40] T. Kalmár-Nagy, R. D’Andrea, and P. Ganguly, “Near-optimal dynamic trajectory generation and control of an omnidirectional vehicle,” *Rob. Auton. Syst.*, vol. 46, no. 1, pp. 47–64, 2004.
- [41] A. S. Conceição, A. P. Moreira, and P. J. Costa, “Trajectory tracking for Omni-Directional mobile robots based on restrictions of the motor’s velocities,” *IFAC Proc. Vol.*, vol. 8, no. PART 1, pp. 1–5, 2006.
- [42] K. Watanabe, Y. Shiraishi, S. G. Tzafestas, J. Tang, and T. Fukuda, “Feedback control of an omnidirectional autonomous platform for mobile service robots,” *J. Intell. Robot. Syst.*, vol. 22, no. 3–4, pp. 315–330, 1998.
- [43] R. Rojas and A. Förster, “Holonomic control of a robot with an omnidirectional drive,” *KI-Künstliche Intelligenz*, p. 7, 2006.
- [44] V. Damić, M. Čohodar, and A. Omerspahić, “Dynamic Analysis of an Omni-Directional Mobile Robot,” *J. Trends Dev. Mach.*, vol. 17, no. 1, pp. 153–156, 2013.
- [45] J. J. Z. and J. L. Yong Liu, Xiaofei Wu, “Omni-Directional Mobile Robot Controller Design by Trajectory Linearization,” *Proc. Am. Control Conf.*, pp. 3423–3428, 2003.
- [46] Y. Liu, J. J. Zhu, R. L. Williams, and J. Wu, “Omni-directional mobile robot controller based on trajectory linearization,” *Rob. Auton. Syst.*, vol. 56, no. 5, pp. 461–479, 2008.
- [47] C. Leng, Q. Cao, and Y. Huang, “A Motion Planning Method for Omni-directional Mobile Robot Based on the Anisotropic Characteristics,” *Int. J. Adv. Robot. Syst.*, vol. 5, no. 4, pp. 327–340, 2008.
- [48] K. Wakita, J. Huang, P. Di, K. Sekiyama, and T. Fukuda, “Human-walking-intention-based motion control of an omnidirectional-type cane robot,” *IEEE/ASME Trans. Mechatronics*, vol. 18, no. 1, pp. 285–296, 2013.
- [49] L. Raj, V. Devcseri, and R. T. Fekete, “State space model of an omni-directional holonomic mobile robot,” *XV Int. PhD Work.*, no. October, pp. 472–477, 2013.

- [50] E. Hashemi, M. Ghaffari Jadidi, and N. Ghaffari Jadidi, “Model-based PIfuzzy control of four-wheeled omni-directional mobile robots,” *Rob. Auton. Syst.*, vol. 59, no. 11, pp. 930–942, 2011.
- [51] A. Bétourné and G. Campion, “Dynamic modelling and Control Design of a Class of Omnidirectional Mobile Robots,” *Proc. 1996 IEEE Int. Conf. Robot. Autom.*, pp. 2810–2815, 1996.
- [52] A. S. Conceicao, A. P. Moreira, and P. J. Costa, “Practical approach of modeling and parameters estimation for omnidirectional mobile robots,” *Mechatronics, IEEE/ASME Trans.*, vol. 14, no. 3, pp. 377–381, 2009.
- [53] S. Djebiani, A. Benali, and F. Abdessemed, “Modelling and feedback control of an omni-directional mobile manipulator,” *2011 IEEE Int. Conf. Autom. Sci. Eng.*, vol. 22, no. 3, pp. 601–616, 2011.
- [54] G. Mekonnen, S. Kumar, and P. M. Pathak, “Wireless hybrid visual servoing of omnidirectional wheeled mobile robots,” *Rob. Auton. Syst.*, vol. 75, pp. 450–462, 2015.
- [55] C. Ren and S. Ma, “Generalized proportional integral observer based control of an omnidirectional mobile robot,” *Mechatronics*, vol. 26, pp. 36–44, 2015.
- [56] N. Hung, D. Kim, H. Kim, and S. Kim, “Tracking Controller Design of Omnidirectional Mobile Manipulator System,” in *ICROS-SICE International Joint Conference 2009*, 2009, pp. 539–544.
- [57] T. D. Viet, P. T. Doan, N. Hung, H. K. Kim, and S. B. Kim, “Tracking control of a three-wheeled omnidirectional mobile manipulator system with disturbance and friction,” *J. Mech. Sci. Technol.*, vol. 26, no. 7, pp. 2197–2211, 2012.
- [58] J. K. Tar, I. J. Rudas, I. Nagy, K. R. Kozłowski, and J. A. Tenreiro Machado, “Simple adaptive dynamical control of vehicles driven by omnidirectional wheels,” *ICCC 2009 - IEEE 7th Int. Conf. Comput. Cybern.*, pp. 91–95, 2009.
- [59] O. Purwin and R. D’Andrea, “Trajectory generation and control for four wheeled omnidirectional vehicles,” *Rob. Auton. Syst.*, vol. 54, no. 1, pp. 13–22, 2006.

- [60] M. Sherback, O. Purwin, and R. D’Andrea, “Real-Time Motion Planning and Control in the 2005 Cornell RoboCup System,” *Lect. Notes Control Inf. Sci.*, vol. 335, pp. 245–264, 2006.
- [61] H.-C. Huang and C.-C. Tsai, “Adaptive Robust Control of an Omnidirectional Mobile Platform for Autonomous Service Robots in Polar Coordinates,” *J. Intell. Robot. Syst.*, vol. 51, no. 4, pp. 439–460, 2008.
- [62] H.-C. Huang and C.-C. Tsai, “FPGA implementation of an embedded robust adaptive controller for autonomous omnidirectional mobile platform,” *IEEE Trans. Ind. Electron.*, vol. 56, no. 5, pp. 1604–1616, 2009.
- [63] C. C. Tsai, H. C. Huang, and T. Y. Wang, “Simultaneous tracking and stabilization of an omnidirectional mobile robot in polar coordinates,” *J. Chinese Inst. Eng. Trans. Chinese Inst. Eng. A/Chung-kuo K. Ch’eng Hsueh K’an*, vol. 32, no. 4, pp. 569–575, 2009.
- [64] H. C. Huang, C. C. Tsai, and S. C. Lin, “Adaptive polar-space motion control for embedded omnidirectional mobile robots with parameter variations and uncertainties,” *J. Intell. Robot. Syst. Theory Appl.*, vol. 62, no. 1, pp. 81–102, 2011.
- [65] J. K. Tar, J. F. Bitó, I. Gergely, and L. Nádai, “Possible improvement of the operation of vehicles driven by omnidirectional wheels,” *Isc. ’09 - 4th Int. Symp. Comput. Intell. Intell. Informatics, Proc.*, vol. 2, no. October, pp. 63–68, 2009.
- [66] R. D’Andrea, T. Kalmár-Nagy, P. Ganguly, and B. Michael, “The Cornell Robocup Team,” *Springer Pap.*, pp. 1–11, 2000.
- [67] Ashivni Shekhawat, T. Kalmár-Nagy, J. Valasek, and T. János, “Near Optimal Trajectory Generation for Omnidirectional Vehicles by Constrained Dynamic Inversion,” *Guid. Navig. Control Conf. Exhib.*, no. August, 2007.
- [68] R. D. Andrea, “The Cornell RoboCup Robot Soccer Team: 1999 – 2003,” *Handb. Networked Embed. Control Syst.*, pp. 793–804, 2003.
- [69] U. Karras, “Robotino – An Open Learning Mobile Robot System for Robocup,” 2009.

- [70] J. Katona, T. Ujbanyi, G. Sziladi, and A. Kovari, “Speed control of Festo Robotino mobile robot using NeuroSky MindWave EEG headset based brain-computer interface,” *7th IEEE Int. Conf. Cogn. Infocommunications, CogInfoCom 2016 - Proc.*, no. CogInfoCom, pp. 251–256, 2016.
- [71] M. Quigley *et al.*, “ROS: an open-source Robot Operating System,” *Icra*, vol. 3, no. Figure 1, p. 5, 2009.
- [72] J. Blanco, “Development of Scientific Applications with the Mobile Robot Programming Toolkit,” *MRPT Ref. book. Mach. Percept. ...*, pp. 1–100, 2008.
- [73] R. Li, M. A. Oskoei, and H. Hu, “Towards ROS based multi-robot architecture for ambient assisted living,” *Proc. - 2013 IEEE Int. Conf. Syst. Man, Cybern. SMC 2013*, pp. 3458–3463, 2013.
- [74] J. Minguez and L. Montano, “Nearness Diagram (ND) navigation: Collision avoidance in troublesome scenarios,” *IEEE Trans. Robot. Autom.*, vol. 20, no. 1, pp. 45–59, 2004.
- [75] Dipl.-Ing. Theo Jacobs, “Standardisation Efforts on Industrial and Service Robots Standardization,” *Stand. NewsL.*, vol. FP7-ICT-2, no. October 2014, pp. 4–7, 2014.
- [76] T. Lipp and S. Boyd, “Minimum-time speed optimisation over a fixed path,” *Int. J. Control*, vol. 87, no. 6, pp. 1297–1311, 2014.
- [77] G. Szayer, B. Kovács, F. Tajti, and P. Korondi, “Feasible utilization of the inherent characteristics of holonomic mobile robots,” *Rob. Auton. Syst.*, vol. 94, pp. 12–24, 2017.
- [78] S. Géza, K. Bence, T. Ferenc, and T. Péter, “GPS-GSM alapú útdíj fizetés műszaki nehézségei,” in *International Conference on Availability, Reliability and Security*, 2014, pp. 48–53.
- [79] F. Tajti, B. Kovács, G. Szayer, and P. Tamás, “Rendvédelmi szerveknél alkalmazható mobil robotok és beágyazott rendszerek,” in *International Conference on Availability, Reliability and Security*, 2014, pp. 85–89.

- [80] F. Tajti, B. Kovács, G. Szayer, P. Korondi, and S. Zoltán, “Variable Robot Geometry Optimization Method to Avoid Tip Over Situations During Slow Motion on Unknown Terrains,” *Acad. Appl. Res. Mil. Public Manag. Sci.*, vol. 15, no. 3, pp. 301–323, 2016.
- [81] R. S. Montero and E. Bribiesca, “State of the art of compactness and circularity measures,” *Int. Math. Forum*, vol. 4, no. 27, pp. 1305–1335, 2009.
- [82] A. Kaufman, G. King, and M. Komisarchik, “How to Measure Legislative District Compactness If You Only Know it When You See it,” no. 617, 2017.
- [83] J. Ernest C. Reock, “A NOTE : Compactness as a Requirement Measuring of Legislative Apportionment,” *Midwest J. Polit. Sci.*, vol. 5, no. 1, pp. 70–74, 1960.
- [84] D. D. Polsby and R. Popper, “The Third Criterion: Compactness as a Procedural Safeguard Against Partisan Gerrymandering,” *SSRN Electron. J.*, vol. 9, no. 2, 1991.
- [85] Joseph E. Schwartzberg, *Reapportionment, Gerrymanders, and the Notion of Compactness*. 1965.
- [86] H. Wadell, “Volume, Shape, and Roundness of Quartz Particles,” *J. Geol.*, vol. 43, no. 3, pp. 250–280, 1935.
- [87] T. Li, S. Li, J. Zhao, P. Lu, and L. Meng, “Sphericities of non-spherical objects,” *Particuology*, vol. 10, no. 1, pp. 97–104, 2012.
- [88] T. D. Gillespie, “Fundamentals of Vehicle Dynamics,” *Analysis*, vol. 400. p. 519, 1992.
- [89] G. Szayer, B. Kovács, and B. Varga, “Etho-robot,” *Workshop on Cognitive and Eto-Robotics in iSpace CERiS’10*. Budapest, p. 7, 2010.
- [90] B. Kovács, G. Szayer, F. Tajti, P. Korondi, and I. Nagy, “Robot with Dog Type Behavior,” in *17th Int. Conference on Electrical Drives and Power Electronics*, 2011, pp. 347–353.
- [91] B. Kovács, G. Szayer, F. Tajti, V. Devecseri, and P. Korondi, “Szociális robotok a 21. században: MOGI Robi a hűséges társ,” in *Erdélyi Magyar Műszaki Tudományos Társaság*, 2012, vol. 2012.04.19, pp. 238–241.

- [92] G. Szayer, B. Kovács, P. Korondi, and F. Tajti, “Holonomic based robot for behavioral research,” in *Proceedings of CERiS’13 - Workshop on Cognitive and Eto-Robotics in iSpace*. 162 p., 2013, pp. 16–20.
- [93] F. Tajti, G. Szayer, B. Kovacs, B. Daniel, and P. Korondi, “CRM TC covering paper - Robotics trends,” in *IECON Proceedings (Industrial Electronics Conference)*, 2013, pp. 48–53.
- [94] F. Tajti, G. Szayer, B. Kovács, and P. Korondi, “Robot base with holonomic drive,” in *IFAC Proceedings Volumes (IFAC-PapersOnline)*, 2014, vol. 47, no. 3, pp. 5715–5720.
- [95] B. Kovács, G. Szayer, F. Tajti, M. Burdelis, and P. Korondi, “A novel potential field method for path planning of mobile robots by adapting animal motion attributes,” *Rob. Auton. Syst.*, vol. 82, pp. 24–34, 2016.
- [96] G. Szayer, B. Kovács, and B. Varga, “Universal Robot Controller,” *Workshop on Cognitive and Eto-Robotics in iSpace CERiS’10*, vol. Budapest,.. pp. 1–26, 2010.
- [97] G. Szayer, B. Kovács, B. Varga, and P. Korondi, “RT middleware based robot controller,” in *International Conference on Mechanical Engineering (Gépészett 2010)*, 2010, vol. 7, pp. 414–422.
- [98] F. Proctor and J. Michaloski, “Enhanced Machine Controller Architecture Overview,” *NIST Intern. Rep. 5331*, 1993.
- [99] B. Kovács, G. Szayer, and F. Tajti, “Design of a universal robot controller,” *Period. Polytech. Mech. Eng.*, vol. 55, no. 2, pp. 95–100, 2011.
- [100] F. Tajti, G. Szayer, B. Kovacs, and P. Korondi, “Shop-floor controller based on RT-middleware technology,” *J. Mech. Eng. Autom.*, pp. 686–694, 2013.
- [101] F. Tajti, G. Szayer, B. Kovacs, and P. Korondi, “Universal RT-middleware robot controller,” in *IECON Proceedings (Industrial Electronics Conference)*, 2013, pp. 1–6.
- [102] K. Bence, T. Ferenc, S. Géza, and T. Péter, “Nyílt forráskódú Linux RTAI alapú 3D nyomtató vezérlés,” in *International Conference on Availability, Reliability and Security*, 2014, pp. 35–38.

- [103] F. Tajti, G. Szayer, B. Kovács, and P. Korondi, “Industrial robotics for ERP controlled smart factories,” *Recent Innov. Mechatronics*, vol. 2, no. 1, pp. 1–9, 2015.
- [104] K. Watanabe, K. Sato, K. Izumi, and Y. Kunitake, “Analysis and control for an omnidirectional mobile manipulator,” *J. Intell. Robot. Syst.*, pp. 3–20, 2000.
- [105] S. Ahmad, H. Zhang, and G. Liu, “Multiple working mode control of door-opening with a mobile modular and reconfigurable robot,” *IEEE/ASME Trans. Mechatronics*, vol. 18, no. 3, pp. 833–844, 2013.
- [106] C. H. Ko, K. Y. Young, Y. C. Huang, and S. K. Agrawal, “Active and passive control of walk-assist robot for outdoor guidance,” *IEEE/ASME Trans. Mechatronics*, vol. 18, no. 3, pp. 1211–1220, 2013.
- [107] J. Huang, W. Xu, S. Mohammed, and Z. Shu, “Posture estimation and human support using wearable sensors and walking-aid robot,” *Rob. Auton. Syst.*, vol. 73, pp. 24–43, 2015.
- [108] M. Tavakoli, C. Viegas, L. Marques, J. N. Pires, and A. T. De Almeida, “OmniClimbers: Omni-directional magnetic wheeled climbing robots for inspection of ferromagnetic structures,” *Rob. Auton. Syst.*, vol. 61, no. 9, pp. 997–1007, 2013.
- [109] M. Tavakoli and C. Viegas, “Analysis and application of dual-row omnidirectional wheels for climbing robots,” *Mechatronics*, vol. 24, no. 5, pp. 436–448, 2014.